

DEVELOPING HIGH THROUGHPUT ORGANOID-BASED PLATFORMS TO STUDY ENTERIC  
PHYSIOLOGY *IN VITRO*

Ian Andrew Williamson

A dissertation submitted to the faculty of the University of North Carolina at  
Chapel Hill in partial fulfillment of the requirements for the degree of Doctor  
of Philosophy in the Joint Department of Biomedical Engineering in the  
School of Engineering.

Chapel Hill  
2018

Approved by:  
Nancy Allbritton  
Scott Magness  
Shawn Gomez  
Scott Bultman  
Jeff Macdonald  
Ian Carroll

© 2018  
Ian Andrew Williamson  
ALL Rights Reserved

## ABSTRACT

Ian Williamson: Developing High Throughput Organoid-based Platforms to Study Enteric Physiology *In Vitro* (Under the direction of Scott T. Magness)

The human gastrointestinal lumen is a complex environment where microbial residents (microbiota) interact symbiotically and pathogenically with the host intestinal mucosa. Intestinal health is regulated by these interactions as they relate to host genetics and food consumption. Human genetic diversity has long been recognized as a key factor in intestinal health and disease. Recently, appreciation has grown for the importance of microbiota interactions with the host mucosa in maintaining homeostasis and disease. The lack of quantitative *in vitro* models to investigate interactions in the intestinal mucosa is considered a substantial barrier to investigate intestinal physiology. Organoids represent an attractive model system because they are derived from primary tissues and embody key properties of the native mucosa; however, assaying organoids specifically in high throughput is technically challenging. Organoids grow as spherical monolayers imbedded in hydrogel limiting access to the enclosed 'lumen' compartment and complicating longitudinal tracking. Furthermore, the homogeneous composition of the three-dimensional culture environment and the heterogeneity of organoid growth patterns complicates readouts based on organoid growth, size, and morphology. Here, I report on the development and validation of several technologies to address the sampling limitations of organoid systems, facilitating high throughput assays describing mucosa physiology, renewal, and interactions with the microbiota.

## **ACKNOWLEDGMENTS**

The work presented in this dissertation is the result of many collaborative projects made possible by the support of the UNC research community. I would like to thank my mentor Dr. Scott Magness for introducing me to laboratory science and believing in my pursuit of an advanced education in bioengineering. I would like to thank the UNC Center for Center for Gastrointestinal Biology and Disease for providing an interesting and diverse environment, facilitating my growth as a basic science researcher. Drs. Susan Henning and Adam Gracz for their guidance throughout my graduate studies. The technologic innovations making up the majority of this work would not have been possible without the help and guidance of Drs. Nancy Allbritton, Christopher Sims, and Yuli Wang in the UNC Chemistry Department. I would like to thank my fellow researchers in the Magness lab and Allbritton lab: Dr. Kyle Roche, Dr. Bailey Zwarycz, Dr. Asad Ahmad, Dr. Pete Attayek, Dr. Matthew DiSalvo, and Jennifer Speer for their contributions to the work detailed here. Finally, I would like to acknowledge the exceptional undergraduates in the Magness lab, including Xiao Fu Liu, Liam Gaynor, and Malvika Pillai.

I also thank my family and friends who have been a constant source of encouragement during the completion of this dissertation. Their support helped me endure the rigors of graduate school, while maintaining my sunny disposition.

## TABLE OF CONTENTS

ABSTRACT .....	iii
ACKNOWLEDGMENTS .....	iv
TABLE OF CONTENTS .....	v
LIST OF FIGURES .....	xii
Chapter 1: Introduction to Intestinal Physiology .....	1
The Intestinal Lumen is our Primary Interface with the Environment .....	1
Organization and physiology of the intestinal mucosa .....	1
Microbiota colonizing the intestinal lumen affect host physiology .....	5
Enteropathies involve aberrant renewal and/or barrier function dysregulating the intestinal luminal interface. ....	6
Inflammatory bowel diseases and the enteric microbiota .....	8
Colitis associated colorectal cancer. ....	11
Gastrointestinal organoids are a reductionist <i>in vitro</i> platform to model intestinal physiology and enteropathies .....	12
Organoid Structure and physiology. ....	12
Modeling human diseases in organoids. ....	14
Significant technical barriers have limited applications of organoid-based assays ....	16
Culture heterogeneity and complicates organoid sampling in 3D space .....	17

Chapter 2: Engineering Platforms to Expand Organoid Applications .....	19
Introduction.....	19
Reconstructing basal-luminal signaling gradients <i>in vitro</i> and measuring gradient influences on organoid compartmentalization .....	20
Developing self-renewing monolayers of primary colonic epithelial cells .....	21
Developing a high throughput microfabricated IESC culture platform to describe intrinsic and extrinsic regulation of stem cell growth .....	23
Methods/Materials .....	24
Reconstructing basal-luminal signaling gradients <i>in vitro</i> and measuring gradient influences on organoid compartmentalization .....	24
Developing self-renewing monolayers of primary colonic epithelial cells .....	25
Developing a high throughput microfabricated IESC culture platform to describe intrinsic and extrinsic regulation of stem cell growth .....	27
Results.....	34
Reconstructing basal-luminal signaling gradients <i>in vitro</i> and measuring gradient influences on organoid compartmentalization.....	34
Developing self-renewing monolayers of primary colonic epithelial cells .....	35
Developing a high throughput microfabricated IESC culture platform to describe intrinsic and extrinsic regulation of stem cell growth.....	36
Conclusions .....	41
Reconstructing basal-luminal signaling gradients <i>in vitro</i> and measuring gradient influences on organoid compartmentalization .....	41
Developing self-renewing monolayers of primary colonic epithelial cells .....	41
Developing a high throughput microfabricated IESC culture platform to describe intrinsic and extrinsic regulation of stem cell growth.....	42

Chapter 3: A High throughput Organoid Microinjection Platform to Study Gastrointestinal Microbiota and Luminal Physiology .....	44
Synopsis .....	44
Overview.....	44
Background & Aims .....	46
Results.....	49
Development of an organoid injection system.....	49
Validating the organoid injection system .....	52
Automated computer vision facilitates high-throughput organoid identification, injection and quantification of injected cargos .....	54
Growth dynamics of transplanted microbial communities and colonoid barrier integrity can be monitored by computer vision .....	56
The colonoid lumen supports the growth of aerobic and obligately anaerobic human microbiota taxa .....	59
Conclusions .....	63
Methods.....	67
Automated Imaging System .....	67
Microinjection Hardware Custom Fittings.....	67
Optimized Microinjection Needle Processing .....	68
Colonoid culture and expansion.....	68
Plating Colonoids on CRA devices.....	69
Computer Vision Identification of Organoids .....	70

Computer Vision Quantification of Injected Cargos.....	71
Assessing Efficiency of Microinjection Device.....	71
Retrieving Bacteria from the Organoid Lumen .....	72
Bacterial Cultivation .....	72
High Resolution Imaging of Microinjected Colonoids .....	73
Mock Community Response to Media Antimicrobials .....	73
Relating Fluorescent Signal to Microbial Load .....	74
Stool Sample Preparation .....	75
Colonoid Fecal Microbiota Transplantation .....	75
DNA Isolation .....	76
16S rRNA Gene amplicon sequencing.....	76
Sequencing data analysis .....	77
Colonoid Anaerobe Monoculture Assay .....	78
Statistics .....	78
Figures .....	80
Appendix A: In Vitro Polarization of Colonoids to Create an Intestinal Stem Cell Compartment.....	103
Introduction.....	103
Materials and Methods .....	106
Transgenic Mouse Models and Isolation of Colonic Crypts.....	106

Colonoid Culture .....	107
Diffusion-Based Gradient Generation and Characterization .....	108
Culture of Colonic Cells in the Microchannel of the Gradient Device .....	109
Microscopy .....	109
Immunofluorescence and EdU Assays .....	110
Colonoid Segmentation using DsRed or Hoechst 33342 .....	110
Measurement of the Percentage of Colonoids Positive for a Fluorophore .....	111
Measurement of Sox9EGFP Polarization in a Colonoid.....	111
Measurement of EdU Polarization in a Colonoid.....	112
Statistics.....	113
Results and Discussion .....	114
Design and Characterization of Gradient-Microdevice .....	114
Microchannel devices support colonoid development similar to conventional cultures .....	115
Colonoids do not demonstrate overall polarization in the absence of an external gradient.....	117
A Wnt-3a gradient is sufficient to polarize the stem/progenitor cell compartments.....	119
A Wnt-3a/R-spondin1 gradient enhances polarization of the stem/ progenitor cell compartment.....	121
Effect of a Wnt-3a and R-spondin1 Gradient on Growth and Polarization of Colonoids Derived from a Single Stem Cell.....	122
Conclusions .....	124

Appendix B: Self-renewing Monolayer of Primary Colonic or Rectal Epithelial Cells ..	136
Introduction.....	136
Materials and Methods .....	138
Isolation of crypts from mouse colon and human rectal biopsies. ....	138
Preparation of the collagen hydrogel in a 6-well plate.....	139
2D monolayer culture on a collagen hydrogel. ....	140
Characterization of the 2D monolayer.....	141
High-throughput screening of dietary metabolites and natural products. ....	142
Assaying for hit dietary compounds on mouse 3D organoids and human 2D monolayers. ....	142
Image Acquisition.....	143
Image Analysis.....	144
Hit Selection.....	144
Other Statistics/Methods.....	145
Results.....	146
A murine colonic epithelial monolayer proliferates on the surface of a collagen hydrogel .....	146
Equivalency of murine colonic 2D monolayers to 3D organoids.....	149
Lineage tracing confirms the presence of stem cells in the murine 2D monolayer.....	150
Human rectal epithelial cells form proliferative 2D monolayers.....	151

Screening dietary components and food metabolites on murine colonic monolayers reveals specific impacts on cell proliferation and differentiation.....	152
Screening dietary metabolites and natural products on human tumor cell lines and primary human rectal cells.....	156
CONCLUSIONS .....	157

## LIST OF FIGURES

Table 1: Factors limiting the use of organoid technologies.....	80
Figure 1. Modified CRAs are compatible with long-term culture of primary IESCs.....	81
Figure 2. Retrieval of magnetic rafts for downstream gene expression analysis.....	83
Figure 3. Software-assisted post hoc analysis identifies initial well contents of CRA culture. ....	85
Figure 4. Cell-to-cell contact is required for PC-influenced survival of IESCs in vitro. ....	87
Figure 5. Single cells do not form cell–cell contacts in microwells after initial plating. ....	89
Figure 6. Robotically Articulated Colonoid Microinjection Maintains Atmospheric Control Facilitating Long-term Sampling of Large Batches of Colonoids: .....	92
Figure 7. Increasing Microinjection Throughput Using Computer Vision to Quantify Cargo Retention, Organoid Morphology and Injection Success: .....	94
Figure 8. The colonoid lumen forms a discrete compartment compatible with specific microbial growth:.....	97
Figure 9: Monolayer Respiration Makes the Colonoid Lumen a Hypoxic Environment Capable of Supporting the Growth of Anaerobic Enteric Microbes: .....	99
Figure 5. The Colonoid Lumen Is Compatible with Patient Derived Microbial Communities and Non-sporulating Anaerobes:.....	101
Appendix A: Fig 1. Characterization of the gradient-generating microdevice.....	126
Appendix A: Fig 2. Colonoid properties in the absence of a gradient.....	128
Appendix A: Fig 3. Incorporation of EdU into colonoids after a 2 h pulse in the absence of a gradient. ....	129
Appendix A: Fig 4. Colonoid growth in the presence of a Wnt-3a gradient across the microchannel. ....	130

Appendix A: Fig 5. Colonoid growth in the presence of a dual Wnt-3a/R-spondin1 gradient.....	132
Appendix A: Fig 6. Growth of single stem cells in the presence of a Wnt-3a/R-spondin1 gradient.....	134
Appendix B: Figure 1. Proliferative 2D monolayer culture of murine colonic crypts on the surface of collagen hydrogel.....	158
Appendix B: Figure 2. Proliferative capacity, lineage composition, and compartmentalization are highly similar between 2D murine colonic monolayers and 3D organoids. ....	160
Appendix B: Figure 3. Lineage tracing of mouse colonic epithelial cells in the 2D monolayer.....	161
Appendix B: Figure 4. Human rectal epithelial cells can be cultured as a proliferative 2D monolayer.....	162
Appendix B: Figure 5. The impact of dietary compounds and natural products on primary murine colonic monolayers.....	163
Appendix B: Figure 6. Assaying a subset of the dietary compounds and metabolites on murine 3D organoids.....	164
Appendix B: Figure 7. The impact of seven dietary compounds and natural products on human primary rectal and tumor Caco-2 cells.....	165

## LIST OF ABBRIVATIONS

3D	Three-dimensional
BMP	Bone Morphogenetic Protein
CBCs	Crypt-base Columnar Cells
CD	Crohn's Disease
CF	Cystic Fibrosis
CHGA	Chromogranin A
CRC	Colorectal Cancer
CTFR	Cystic Fibrosis Transmembrane Conductance Regulator
DSS	Dextran Sulfate Sodium
ENS	Enteric Nervous System
FACs	Fluorescence Activated Cell Sorting
GF	Germ-free
GI	Gastro Intestinal
IBD	Inflammatory Bowel Disease
IESC	Intestinal Epithelial Stem Cell
Lct	Lactase
LPS	Liposaccharide
MAMPs	Microbe Associated Patterns
MVID	. Microvillus Inclusion Disease
PBS	Phosphate Buffered Saline
PC	Paneth Cell

PEG	Polyethylene Glycol
PRRs	Pattern Recognition Receptors
RFP	Red Fluorescent Protein
SCFAs	Short-chain Fatty Acids
SIS	Sucrase-isomaltase
TA	Transit-amplifying
TLR	Toll-like Receptor
UC	Ulcerative Colitis
Wnt	Wingless-related Integration

## **Chapter 1: Introduction to Intestinal Physiology**

### **The Intestinal Lumen is our Primary Interface with the Environment**

Absorption of ingested nutrients occurs in the intestine where components of digested food are both actively transported and passively diffuse into the body. The intestine is a complex tissue consisting of mucosa, muscularis, and serosa layers with distinct cellular composition and function. The innermost mucosa layer of the intestine is responsible for the bulk of absorptive processes. The intestinal mucosa consists of a supportive lamina propria of fibroblasts, myofibroblasts, capillaries, and lymphocytes underlying a monolayer of columnar epithelium (intestinal epithelium) that directly interfaces with the luminal space. The outer submucosa, muscularis, and serosa layers of the intestine drive the movement of ingested material down the gastrointestinal (GI) tract and regulate the transport of absorbed nutrients to the rest of the body. This dissertation focuses on the mucosa layer and developing *in vitro* approaches to study physiology and renewal of the epithelial surface of the lumen.<sup>1,2</sup>

### **Organization and physiology of the intestinal mucosa**

The small intestinal epithelium is organized into microstructure functional units of regularly dispersed invaginations into the lamina propria termed 'crypts' surrounding villi projections into the lumen. The intestinal epithelium renews rapidly to maintain function with near-total turnover every 5-7 days. The kinetics of intestinal renewal were established by "lineage tracing" models where actively dividing cells were labeled with

titrated thymidine and their migration was observed at various times following administration<sup>1</sup>. These approaches identified a pluripotent intestinal epithelial stem cell population (IESC) in the base of each crypt that divides roughly every 24 hour, producing transit-amplifying progenitors (TA) that populate the crypt neck. TAs differentiate as they migrate up the crypt and eventually reach the villus tip before sloughing off into the luminal space. Similarly, to the small intestine, the colonic epithelium is renewed by actively cycling IESCs residing in crypt invaginations into the lamina propria. The colon lacks villi projections, instead forming a smooth surface that interacts with the luminal contents. Renewal of the colonic epithelium is similarly rapid, with near-total turnover every 7-10 days driven by crypt residing stem cells. The crypts are largely devoid of differentiated cells, which are subdivided into absorptive and secretory lineages based on their function and expression of associated peptides. Absorptive lineages have distinct columnar morphology and express digestive enzymes such as sucrase isomaltase (SIS) and lactase (Lct). The intestinal epithelium is dominated by absorptive cells, but secretory lineages dispersed throughout the tissue serve important homeostatic functions. Goblet and enteroendocrine cells, dispersed throughout the intestinal epithelium, secrete protective and signaling peptides maintaining homeostasis. Goblet cells produce mucins that collect in the lumen to maintain epithelial barrier integrity and are traditionally identified by intracellular *Muc2* peptide expression. Enteroendocrine cells release hormones into the lumen and underlying lamina propria to carry signals to far regions of the intestine or other tissues. Enteroendocrine cells are conventionally identified by their cytosolic hormone peptides like *Chromogranin A* (CHGA). One secretory cell type, the Paneth cell (PC), resides

exclusively in the base of small intestinal crypts where they secrete protective antimicrobials like lysozyme that form a niche for resident stem cells.<sup>1-3</sup>

Components of the mucosa produce secreted and membrane bound ligands forming localized signaling gradients that regulate renewal. The Wingless-related integration site (Wnt), Bone morphogenic protein (BMP), and Notch signaling pathways are the most substantially linked to epithelial proliferation and differentiation. Niche cells near the crypt base secrete Wnt ligands that bind to receptors on crypt-based cells, stabilizing cytoplasmic *β-catenin*. Stabilized *β-catenin* translocates to the cell nucleus, where it activates the *TCF* and *LEF* transcription factors that drive targets generally associated with cellular growth and proliferation. Wnt signaling decreases as cells migrate away from the crypt base reducing access to niche ligands. BMP signaling acts opposite of Wnt signaling, driving differentiation as cells migrate up the crypt villus axis. *Bmp4* and related ligands are strongly expressed in the villus mesenchyme, where it binds to serine/threonine kinase receptors on epithelial cells to activate genes through the *SMAD* transcription factor<sup>4-7</sup>. Notch signaling is mainly restricted to the crypt compartment, where active stem cells and TAs express *Notch1* and *Notch2* receptors. High levels of notch signaling are necessary for terminal absorptive cell formation, while lower levels drive progenitors towards secretory lineages. Redundancies in signaling ligands and receptors rendering individual components of each pathway expendable under homeostatic conditions, making the signal transduction network regulating intestinal renewal highly complex. The intricacies of the molecular functions of each pathway have been described at great length elsewhere.<sup>8-10</sup>

The dynamics of intestinal epithelial renewal have been well understood for decades but direct studies of IESCs were hampered by a lack of specific genetic biomarkers. In 2007, the G-protein coupled receptor *Lgr5* was validated by *in vivo* lineage-tracing as an IESC biomarker expressed in crypt-base columnar cells (CBCs) intercalated between PCs in the crypts of the small intestine<sup>11</sup>. Tracing the progenitors of *Lgr5* cells through genetic lineage tracing showed that progeny formed long-lived clonal units containing all post-mitotic lineages persisting for 60 days or longer. These studies confirmed the self-renewal and multipotency of *Lgr5* CBCs and established the gold standard of *in vivo* lineage tracing used to identify additional CBC IESC biomarkers including *Olfm4*, *Ascl2*, and *Sox9*<sup>12–15</sup>. Following the identification of the CBC IESC population, a second IESC population residing above the PC compartment was described by lineage tracing from *Bmi1* expressing cells<sup>16</sup>. Subsequently, other genes associated with the super-Paneth position were validated as *in vivo* IESC biomarkers, including mTert and Hopx<sup>17</sup>. While all the super-Paneth IESC populations have some stem cell capacity under normal physiological conditions, reports show increased lineage tracing from super-Paneth IESC biomarkers following damage. The field consents that super-Paneth IESCs represent a reserve population, normally quiescent, that activates to initiate repair following damage to CBC IESCs<sup>16–18</sup>. This model has been confirmed by genetically ablating *Lgr5* IESCs in animal models, which were able to compensate by activating super-Paneth IESC populations.

Rapid renewal allows the intestinal epithelium to change composition, by changing the abundance of absorptive and secretory lineages as well as the digestive, transport, or protective peptides they produce. These mechanisms allow the intestinal epithelium

to act as a dynamic, selectively permeable barrier to allow absorption of essential nutrients while sealing the body from harmful toxins and microbial invasion. The intestinal mucosa responds dynamically to nutrient availability in specific and non-specific manners to increase or decrease absorption. Villi projections extend further into the lumen in response to feeding, grossly increasing the absorptive surface area and potential<sup>19</sup>. The apical surface of absorptive epithelial cells is coated with membrane projections called microvilli that are highly concentrated with transport proteins and digestive enzymes. Digestive enzymes on the apical surface break down macromolecules like carbohydrates into monomers for active transport by absorptive enterocytes into the body. Other polar nutrients like ions are also actively transported by proteins on the apical membrane of enterocytes. Lipids are digested into monoglycerides and free fatty acids that passively diffuse into the cytosol. Absorptive enterocytes change their expression of transport proteins and digestive enzymes to increase or decrease specific nutrient uptake in response to nutritional requirements and availability.<sup>20</sup>

### **Microbiota colonizing the intestinal lumen affect host physiology**

Nutrient availability in the intestine is strongly influenced by the thousands of symbiotic microbial species, collectively referred to as the enteric microbiota, that colonize the lumen in stable populations. The microbiota is comprised of bacteria, fungi, protozoa, and archaea that inhabit specific regions of luminal space in complex overlapping communities. Bacteria are the best characterized component of the enteric microbiota with 300-1000 species observed in the microbiota of healthy adults. Microbiota bacteria ferment digested material into bioactive metabolites that are

absorbed by the epithelium, where they act as energy sources, mitogens, and morphogens effectively preserving normal physiology. The classical example of host-microbiota molecular interactions is butyrate, produced by bacterial fermentation of dietary fiber in the colonic lumen. Enterocytes prefer butyrate to glucose as an energy source promoting stem cell driven renewal. Butyrate also acts as a morphogen by inhibiting epigenetic changes in histone methylation. The microbiota also produce neuroactive peptides like serotonin and gaba that grossly effect host digestion and peristalsis.<sup>21-23</sup>

The bacterial component of the enteric microbiota is dominated by gram-positive species of the Firmicutes, Bacteroidetes, Actinobacteria, or Proteobacteria phylum that compete for suitable luminal space. The composition of the microbiota is stabilized by competition for key nutritional and environmental factors. Changes in the luminal environment caused by pathogens, antimicrobial treatment, or dietary changes can lead to the overgrowth of specific members inside or outside of their normal habitat, termed dysbiosis. Dysbiosis is particularly important in modern health care due to an epidemic of *Clostridium difficile* colitis caused by the overgrowth of an anaerobic motile bacteria normally inhabiting the small intestine. *C. difficile* dysbiosis occurs in about 500,000 Americans every year, reoccurring in nearly 25% and causing mortality in about 5% of cases due to severe colon inflammation and diarrhea.

**Enteropathies involve aberrant renewal and/or barrier function dysregulating the intestinal luminal interface.**

Nonpathogenic enteropathies result from dysregulation of the complex balance between intestinal renewal, barrier function, and nutrient absorption. The most well

characterized non-pathogenic enteropathies result from aberrant renewal or differentiation caused by mutations in Wnt, BMP, or Notch signaling components. Mutations causing IESC populations to become hyperproliferative lead to crypt hyperplasia and adenomas, arising in 20-50% of Americans by age 70. Adenomas lead to the formation of polyps, which dramatically increase cancer risk. Nearly 1 million new cases of colorectal cancer (CRC) are diagnosed each year with familial risk associated with about 30% of cases. Some cases are caused by autosomal dominant mutations that drive polyposis or nonpolyposis forms of hereditary colorectal cancer. These two conditions cause 5-10% of CRC and are directly inherited by an affected individual. The other 20% of new cases with concurrent familial risk have recessive or partially functional mutations in key tumor-suppressor and oncogenes. In these cases, cancer is initiated through subsequent mutations in the Wnt or BMP signaling pathways. Accumulation of cell signaling changes, rather than the order of occurrence, initiates tumor formation.<sup>24-27</sup>

Mutations in genes coding for key transporters or structural peptides can also drive enteropathies, causing nutrient malabsorption. Microvillus inclusion disease (MVID) is caused by mutations in *myosin Vb*, which stunts enterocyte differentiation. Without *myosin Vb* enterocytes lack microvilli and distinct apical-basal lateral polarity. MVID is often fatal early in life due to intractable diarrhea and metabolic acidosis. MVID is an autosomal recessive disorder with the defective *myosin Vb* gene inherited from both parents that may not be affected. An autosomal recessive mutation in the ion transporter, cystic fibrosis transmembrane conductance regulator (CTFR), also drives malabsorptive enteropathy. Loss of function prevents the secretion of chloride and

carbonate ions, leading to a syndrome termed cystic fibrosis (CF). CF causes thickening of the mucous secreted into the lumen, causing blockages and preventing ingested material from reaching the apical surface. More than 5,000 specific mutations in *CTFR* are known to cause CF though the effect of *CTFR* dysfunction that leads to the CF phenotype is still under debate.<sup>28–30</sup>

### **Inflammatory bowel diseases and the enteric microbiota**

There is considerably less consensus on the kinetics of enteropathies driven by the dysregulation of host immune responses. In these syndromes, inappropriate responses by enteric immune cells cause prolonged inflammation of the mucosa that can disturb nutrient absorption and barrier function. In Celiac disease, dietary glutens that are absorbed by the mucosa interact with type II major histocompatibility complexes to activate lymphocytes. Prolonged lymphocyte activation leads to lesions of flat villi and hyperplastic crypts to form. Similar lesions occur in cases of inflammatory bowel disease (IBD) where microbial cues activate and prolong inflammation. The specific microbial taxa, epithelial receptors, and cell signaling pathways initiating and prolonging IBD are still under debate despite extensive investigations. Our understanding of the microbiota's role in IBD has been reviewed in detail elsewhere and will be summarized here.<sup>31,32</sup>

Dysbiosis is thought to drive IBD by dysregulating cell signaling patterns and affecting host gene expression. This is directly accomplished through the binding of microbe associated patterns (MAMPs) to pattern recognition receptors (PRRs) on the apical epithelial surface. The involvement of the Toll-like receptor (TLR) family of PRRs in cell signal transduction has been well characterized. Bacteria cell wall components

like peptidoglycan and flagellin are known TLR ligands that increase the expression of nuclear factor-KB regulated targets when bound to TLRs<sup>33,34</sup>. In healthy states the host intestine becomes habituated to commensal microbiota taxa and reduces its inflammatory response. Habituation is accomplished through the expression of redundant inhibitory peptides (reviewed by <sup>28,32,35-38</sup>) regulating paracrine interactions between the intestinal epithelium and regulatory lymphocytes in the lamina propria. Various metabolic byproducts produced by commensal microbiota enhance the expression of anti-inflammatory peptides by the host epithelium. In this way the microbiota can directly modulate host immunity to relieve inflammatory responses and maintain homeostasis.

Short-chain fatty acids (SCFAs) produced by commensal microbiota have been most directly linked to host immune response. These 2-6 carbon bioactive metabolites, produced by dietary fiber fermentation, have been implicated as regulators of T-cell and dendritic lymphocyte activity. Propionate and acetate support the development of Th1, Th17, and IL-10 regulatory T-cell populations, while Butyrate acts as a systemic T-cell inhibitor. SCFAs are metabolized into acetyl-CoA in epithelial cells, which acts as an activator for mTOR-mediated gene expression. Valproate, propionate, and butyrate also inhibit the maturation and trafficking of dendritic cells by reducing epithelial release of proinflammatory ligands. The anti-inflammatory effect of microbiota produced SCFAs is exemplified by propionate and butyrate reducing IL-6 and IL-12 production resulting from liposaccharide (LPS) binding to TLR-4. Commensal microbiota taxa also reduce host immune response by less direct means than the secretion of anti-inflammatory factors. Certain microbiota taxa including *Bifidobacterium* are thought to stimulate

mucous production, increasing mucosa barrier integrity and reducing interactions between luminal contents and the mucosa.<sup>28,32,38–40</sup>

Considerable evidence links dysbiosis to IBD pathogenesis but direct evidence has not been convincingly demonstrated. IBD cases are sub-classified by the tissues that they affect. Ulcerative Colitis (UC) primarily effects the distal colon and rectum, while Crohn's disease (CD) is more systemic with affects observed in the small intestine, colon, mouth, esophagus, and stomach. The microbial load of the intestinal lumen is increased in both forms of IBD, with significantly more anaerobic and aerobic bacteria recovered from IBD patient stool samples compare to controls. IBD symptoms are most severe in the distal colon where the highest load of microbiota is found. Rodents with mucosal defects in PRRs or downstream ligands have chronic intestinal inflammation. These rodent models fail to achieve pathogenesis when raised in germ-free (GF) conditions further implicating the enteric microbiota in IBD. Microbiota composition is considerably altered in both IBD types with increases in *Bacteroidetes*, *Lactobaccillus*, and *Proteobacteria* taxa observed. Outgrowth of *Bacteroidetes* taxa coincides with decreases in *Firmicutes* taxa, significantly increasing the ratio of *Bacteroidetes* compared to *Firmicutes* comprising the microbiota. This ratio has become key in diagnosing IBD and measuring thepoetic relief. More direct evidence links dysbiosis to CD than UC. CD is associated with polymorphisms in PRRs by genome-wide association studies. Also abundant taxa like *Escherichia coli* isolated from CD patients shows enhanced virulence compared to strains from healthy controls.<sup>29,38,41,42</sup>

The strongest evidence for the microbiota's involvement in IBD may be the relief patients experience when receiving microbially-targeted treatments. Early research

found that CD symptoms were relieved when the luminal fecal stream was diverted and reoccurred once fecal flow was restored. Microbial treatments for IBD have expanded since that finding to include antibiotic and probiotic treatments aimed at correcting dysbiosis. IBD patients experience symptom relief when treated with antibiotics, which is lost with long term use. This fits the model of acquired antibiotic resistance observed in many bacterial pathogens. Probiotic treatments delivering live *Bifidobacterium* and *Lactobacillus* microbes can prevent IBD lesion reoccurrence in some patients and rodent models. But the relief is not ubiquitous across patients and symptomatic profiles. Expanding microbiota-targeted IBD treatments has been difficult, in part due to the interpersonal variability in microbiota profile and symptom presentation in IBD patients.<sup>43–48</sup>

### **Colitis associated colorectal cancer.**

Dysbiosis is also strongly linked with CRC initiation and progression. The link was originally described in rodent models employing mucosa irritants like Dextran Sulfate Sodium (DSS) to cause inflammation making the intestine susceptible to carcinogens. Carcinogenesis stimulated by these approaches is limited in GF individuals with reduced tumor size and burden compared to colonized controls. This linked inflammation, known to be regulated by the microbiota in humans, to CRC. Case studies show that more than 20% of IBD patients develop CRC within 30 years of developing colitis with high mortality observed in colitis-associated cancers. Even CRC patients without clinically detected IBD display robust inflammation and increased levels of inflammatory cytokines. The composition of the enteric microbiota is altered in CRC patients compared to healthy controls but changes in individual taxa are inconsistent.

Microbiota composition also varies within individual CRC patients when sampled at tumor sites or healthy regions of mucosa. Despite the high variability in CRC-associated dysbioses, several microbiota species meet the Bradford Hill criteria for epidemiologic causality of CRC. *Enterotoxigenic Bacteroides fragilis*, *Enterococcus faecalis*, *Escherichia coli*, and *Fusobacterium necrophorum* can produce Wnt and pro-inflammatory ligands that can dysregulate intestinal renewal and repair potentially driving carcinogenesis.<sup>23,44,49–53</sup>

### **Gastrointestinal organoids are a reductionist *in vitro* platform to model intestinal physiology and enteropathies**

The lack of techniques to culture primary intestinal tissues has limited the mechanistic description of GI biology during health and disease states. Many of the early studies on molecular regulation of intestinal renewal relied on *in vivo* models that limit the scope of longitudinal IESC studies. Transplanting human fecal microbiota samples into GF animal models have been fruitful in describing human diseases, but GF facilities are rare and GF animal housing is costly, limiting scale and the use of transgenic animals<sup>54–56</sup>. Recently, concerns have been raised around the metabolic profiles of mice raised GF, and their differential expression of epithelial transport proteins confounds interpretations made following colonization<sup>52,55,57</sup>.

#### **Organoid Structure and physiology.**

Controlled testing of the molecular kinetics behind variable phenotypes of the intestinal epithelial represented in human disease states is a daunting task. More robust *in vitro* studies of intestinal physiology have historically been limited to immortalized cancer cell lines. However, these lack lineage identity and normal metabolic processes,

limiting their power as physiologic models<sup>56</sup>. Recent reports utilize advanced, three-dimensional (3D) culture techniques that produce intestinal epithelial organoids from isolated IESCs<sup>58</sup>. Organoids recapitulate the native tissue patterning, renewal, membrane transport, and other physiologic properties. Embedding IESCs in protein hydrogel mimics the extra cellular matrix (ECM) of the lamina propria. Ligand peptides and small molecule inhibitors targeting the Wnt, Bmp and Notch are delivered in the culture media driving niche signaling. All these components are necessary to drive IESC renewal *in vitro* forming complex multicellular monolayers in 3D space. <sup>59</sup>

Organoids self-pattern into hollow structures as they grow, with proliferative IESCs restricted to specific regions. Organoid IESC populations are often concentrated in crypt-like ‘buds’ projecting from the enclosed organoid ‘lumen’ where they produce adjacent progenitors that differentiate as they migrate toward the organoid lumen. In this way, organoids recapitulate normal renewal with cycling stem cells producing all the differentiated lineages of the native epithelium<sup>60</sup>. Importantly, organoid cells maintain native polarity, exhibited through differential expression of transporter proteins on their inner apical and outer basolateral membranes<sup>61</sup>.

Organoids retain tissue and regional identity transferring the full profile of endogenous stem cell populations to laboratory settings. Organoid technology was initially described for murine small intestine IESC culture but has been expanded to culture colon, liver, pancreas, and esophagus of animal models and human samples. The lack of associated tissue layers makes organoids a truly reductionist model of epithelial physiology free of artifactual effects of feedback from other tissues. In attempts to reduce such artifacts, organoid culture techniques have become more

refined. Synthetic Polyethylene glycol (PEG) hydrogels are replacing the animal derived ECM hydrogels employed in early reports. Groups are also expanding the use of small molecules to replace peptide ligands that have variable activity, confounding studies. Small molecule treatment can enrich organoids with specific lineages by changing cell signaling kinetics.<sup>58,62,63</sup>

### **Modeling human diseases in organoids.**

Organoids represent an important bridge between traditional 2D cultures and *in vivo* mouse/human models. Organoids are genetically stable and recapitulate traits of the source tissue more completely than conventional immortalized cell cultures. IESC niche conditions can be more easily manipulated in organoids than animal models. Organoids can be grown from transgenic animals to study the genetic involvement in renewal processes specifically in the epithelium. Genetic manipulation of organoids using viral and CRISPR/Cas9 vectors has also been demonstrated allowing for novel transgenic lines to be produced *in vitro*. The self-renewal capacity of organoids can be used to expand specific, rare mucosa populations that are not easily collected from animal models.<sup>64–68</sup>

Organoids grown from diseased patients or animal models recapitulate disease phenotypes, allowing researchers to study enteropathies in a laboratory setting. Patient derived organoids have been used most extensively when studying genetically driven enteropathies, which are recapitulated *in vitro* due to the genomic stability of organoid IESCs. For this reason, organoids grown from MVID patients have stunted microvilli with reduced digestive enzyme loads. Similarly, organoids with mutations in CFTR have characteristic defects in ion transport. This has been exploited to assess disease

restitution by treating defective organoids with small molecules to drive CTFR activity, which causes healthy organoids to swell in size. Induced swelling of CTFR mutant organs following gene editing demonstrated a gain of CTFR function effectively curing CF.<sup>57,63,66,69,70</sup>

Introducing mutations to oncogene and tumor suppressor alleles causes human and murine organoids to adopt a cancer-like phenotype. Serial mutations to Wnt and BMP signaling components drives organoid IESC proliferation without the normally essential stimulation by niche signaling. The cancer-like phenotype of organoids is assessed by starving established cultures of Wnt and BMP ligands usually delivered in the media. Organoids with mutations in oncogenes driving WNT and BMP signaling survive long-term without normally essential ligands. Cancer-like human and murine organoids form tumors when transplanted into animal models demonstrating the extent that organoids can be used to model disease.<sup>15,27,71,72</sup>

Co-cultures of intestinal organoids and microbes are being pursued to study host-microbiota interactions in health and disease. These studies look to leverage similarities between the lumen of organoids and the native tissue to cultivate microbiota taxa in a physiologic context. Protective mucins and antimicrobial peptides accumulate in the organoid lumen along with exfoliated cells that migrated from the bud tips. Starving organoids of Wnt signaling factors or accelerating differentiation with small molecules increases the rate exfoliated cells accumulate in the organoid lumen. Inhibitors can be used to force organoid secretory cells to release vesicle content into the organoid lumen delivering a variety of antimicrobial and anti-inflammatory peptides.

<sup>32,64,69,73-77</sup>

Organoids also display many PRRs on their enclosed apical surface providing the major molecular components mechanistically involved in host-microbe interactions. Organoids at least express *TLR2*, *TLR3*, *TLR4*, *TLR7*, *TLR8*, and *TLR9* that demonstrate various functions when activated *in vitro*. Activating *TLR3* by peptidoglycans increases the expression of inflammatory cytokines. Certain peptidoglycans also interact with *CD14* causing IESCs to divide more quickly and expand in number, increasing organoid outgrowth. These effects were lost in organoids from mouse models with defects in TLR-mediated signaling pathways. These properties make self-renewing intestinal organoids an attractive, new option for co-culture studies with enteric microbes.<sup>32,64,69,73–77</sup>

### **Significant technical barriers have limited applications of organoid-based assays**

A variety of factors have limited the use of organoid technologies in studying in variety of GI health and disease processes, detailed in Table 1: Factors Limiting the use of organoid technologies

Organoids lack components of other tissue layers that may be necessary to accurately demonstrate disease states. Organoids lack neural cells that form an extensive enteric nervous system (ENS) *in vivo* containing 200-600 million neurons, many of which are synoptically connected to enteroendocrine cells in the mucosa. This allows the ENS to sense luminal signals and conduct bidirectional communication between the central nervous system and the intestine. Nervous system interactions modulate the release of local and systemic hormones affecting intestinal function. Some progress has been made to incorporate neural components into organoid cultures in hopes of studying ENS interactions with the mucosa. This approach confirmed the

presence of synaptic connections between ENS neurons and enteroendocrine cells<sup>77-79</sup>. Less progress has been made incorporating immune cells into organoid culture platforms, limiting their use to study IBD mechanistically. Organoid technology has instead been employed to assess epithelial barrier function and PC dysfunction in IBD contexts using genetic models and inflammatory cytokine treatment.<sup>62,63,79-83</sup>

Organoids also lack mesentery components limiting their use in modeling fibrosis, a process that is also difficult to illicit in rodent models. Mesentery cell types are sufficiently compatible with organoid culture conditions for robust co-culture assays. Incorporating specific myofibroblast populations into organoid cultures allowed researchers to identify specific subpopulations of myofibroblasts driving fibrosis and evaluate the potency of anti-fibrotic drugs.<sup>68,84,85</sup>

Adding non-epithelial cell types and tissue layers to organoid culture platforms is a prolific area of biotechnology innovation that will be integral in expanding the application of organoids to study disease. This dissertation instead focuses on mechanically refining organoid platforms to expand their applications.

### **Culture heterogeneity and complicates organoid sampling in 3D space**

Organoid culture techniques were originally developed for the murine small intestine but have been expanded to culture stem cells from the colon, stomach, and esophagus of human samples and animal models. The expansion and modeling potential of these culture systems makes organoid-based assays attractive for drug screening and regenerative medicine, but applications have been limited due to the technical difficulty associated with sampling organoids grown in 3D. Specific IESCs are impossible to track longitudinally in 3D space preventing researchers from quantifying

changes in specific organoids. Organoid heterogeneity further complicates sampling, with highly variable starting sizes and expansion rates. This heterogeneity limits the use of organoid size or growth as treatment readouts without introducing artifacts into experimental results. Organoids grown from the same source also have variable cellular composition that can affect responses to treatments and challenges. Organoids lacking mature secretory cells have a limited response to microbial challenges, while increased goblet cell content protects organoids from pharmaceutically driven inflammation. Organoid IESC content also affects response to treatments or challenges effecting renewal. CBC and super-Paneth IESC populations are known to interconvert and can interact through *Wif1* and *FoxA1* cell signaling. Super-Paneth IESCs are thought to induce tumorigenesis *in vivo* and may be necessary to accurately recreate cancer initiation. The remainder of this dissertation will focus on my attempts to address these limitations through automation, microfabrication, and biomaterial innovation.<sup>11,18,63,86-88</sup>

## Chapter 2: Engineering Platforms to Expand Organoid Applications

### Introduction

Organoid cultures require defined growth conditions that mimic the IESC niche, making organoid growth a physiological readout for the activity of niche factors delivered *in vitro*. Organoid formation and self-renewal has been used as a measure of Wnt activity and its effect on IESC activity. Mice genetically lacking the PC produced niche factor *Wnt3* form normal crypts but fail to grow organoids in standard conditions. Adding exogenous Wnt driving ligands to the culture media rescues organoid formation allowing researchers to assess the effects of redundant signaling sources on IESC renewal. Inhibiting notch signaling *in vitro* phenocopies the manipulation *in vivo*, resulting in massive goblet cell production. Deletion of *Lrig1*, an inhibitor of BMP signaling, increases IESC numbers *in vivo* and *in vitro*. These results show that organoids accurately recapitulate Wnt, BMP, and Notch's influence on IESC driven renewal and the effects of perturbation on epithelial physiology. Closing the gap between organoid culture technologies and high throughput conventional monolayer culture technologies will better leverage organoids to mechanistically describe intestinal renewal and disease.<sup>5,88–91</sup>

Parts of this chapter previously appeared as an article in the journals NCB, Plos1, and CMGH the original citations are as follows:

Gracz, A. D. et al. A high-throughput platform for stem cell niche co-cultures and downstream gene expression analysis. *Nat. Cell Biol.* 17, 340–349 (2015).

Attayek, P. J. et al. Automated microwell platform to identify and collect non-adherent cells successfully gene-edited with CRISPR-Cas9. *Biosens. Bioelectron.* 91, 175–182 (2017).

Wang, Yuli, DiSalvo, Matthew, Gunasekara, Dulani B., Dutton, Johanna, Proctor, Angela, Lebnar, Michael S., Williamson, Ian A., Speer, Jennifer, Howard, Riley L., Smiddy, Nicole M., Bultman, Scott J., Sims, Christopher E., Magness, Scott T. & Allbritton, Nancy L. Self-renewing Monolayer of Primary Colonic or Rectal Epithelial Cells. *CMGH* 4, 165–182.e7 (2017).

Williamson, Ian A., Arnold, Jason W., Samsa, Leigh Ann, Gaynor, Liam, DiSalvo, Matthew, Cocchiaro, Jordan L., Carroll, Ian, Azcarate-Peril, M. Andrea, Rawls, John F., Allbritton, Nancy L. & Magness, Scott T. A High-Throughput Organoid Microinjection Platform to Study Gastrointestinal Microbiota and Luminal Physiology. *Cell. Mol. Gastroenterol. Hepatol.* 1–38 (2018). doi:10.1016/j.jcmgh.2018.05.004

## Reconstructing basal-luminal signaling gradients *in vitro* and measuring gradient influences on organoid compartmentalization

In standard platforms, organoids are exposed to systemically high concentrations of signaling ligands more closely resembling the crypt environment than the more differentiated epithelial compartments. Culture media ligand levels can be manipulated to effect extrinsic signaling but cannot recapitulate the opposing Wnt-BMP signaling gradients that normally regulate epithelial renewal. A tight correlation between Wnt activity and IESC proliferation is observed *in vivo*, with the highest levels of both observed at the basal-lateral pole, but it has been difficult to specifically describe Wnts role in regulating epithelial patterning. Transgenic animal models inactivating or stimulating Wnt signaling have noteworthy phenotypes. Loss of signaling arrests IESC proliferation and constitutive activation causes hyperproliferation and crypt hyperplasia. Loss of Wnt target genes like *EphB2* and *EphB3* causes defects in PC migration with lysozyme expressing cells observed throughout the mucosa. <sup>87,92-96</sup>

Testing the impact of factor gradients in epithelial patterning *in vivo* is technically challenging, relying on indirect readouts like gene expression. We developed a gradient-forming device to recreate a physiologically relevant microenvironment for testing the kinetics of Wnt's regulation of crypt compartmentalization. Recently the Allbritton lab described a microfluidic device specifically developed for optimizing growth factor concentrations for efficient culture of colon organoids (colonoids). Colonoids at each end of the produced Wnt gradient displayed distinctly different morphologies. Patterns associated with differentiation were observed at the low end of the gradient and patterns associated with high IESC content were observed at the high end of the

gradient. The absence of IESC segregation within a single colonoid was likely due to the shallow gradient imposed across each colonoid, effectively placing the entire colonoid within the same chemical environment. The microfluidic device to increase the slope of the produced Wnt gradient and test if chemical gradients of signaling factors can pattern individual colonoids under controlled conditions (Appendix A: Fig1).<sup>87,92-96</sup>

Initial attempts employing a gradient of only *Wnt3a* were mildly successful. Colonoids grown under a steep linear gradient of *Wnt3a* demonstrated observable by *Sox9*<sup>EGFP</sup> polarity but failed to significantly affect the pattern of proliferation (Appendix A: Fig4). I included the Wnt co-factor *R-spondin1*, normally systemically delivered in culture, to the linear gradient in hopes of exaggerating the polarity observed under *Wnt3a* gradients. Furthermore, IESCs were being cultured in the microchannel device from whole crypt units containing PCs and other niche components. I hypothesized that the native niche components being used in the microchannel cultures might be masking the effects of the ligand gradients. I sought to remove these artifacts by sorting individual IESCs from dissociated crypts by fluorescence activated cell sorting (FACS).

### **Developing self-renewing monolayers of primary colonic epithelial cells**

Conventional immortalized intestinal cell lines have been used in high throughput screenings aimed at describing intestinal renewal. Cancer cell lines grow as confluent monolayers and can be efficiently passaged making them compatible with conventional high throughput cell-based assays. Though immortalized cell lines are widely applied in GI research, they possess many non-physiologic characteristics including somatic mutations, chromosomal instabilities, altered metabolism, aberrant proliferative and limited differentiation. The non-physiologic properties of immortalized cell lines call into

question their predictive ability in assays designed to understand normal epithelial physiology. Although organoid culture technology has had a major positive impact on the in vitro study of primary gut epithelium, the 3D geometry of organoids prevents access to the apical aspect of the epithelium, making lumenally relevant studies challenging. The spheroidal architecture of the organoids prevents access of exogenously delivered compounds to the luminal surface, limiting studies focused on apical transporters, receptors, and metabolic enzymes.

Furthermore, hydrogel embedded organoids exist in multiple planes, making imaging by conventional microscopy exceptionally challenging and low throughput. Unfolding the spherical organoid into a two-dimensional (2D) monolayer addresses these major challenges and could further transform in vitro study of the gut epithelium. Primary intestinal epithelial tissue is difficult to culture long-term as a monolayer because tissues cultured in these systems rapidly lose stem and proliferative cells through apoptosis. The Allbritton lab previously demonstrated that primary tissues can form short-lived, non-proliferative monolayers on polydimethylsiloxane (PDMS) and other artificial surfaces in the absence of a hydrogel. They sought to identify parameters that would support self-sustaining monolayers and identified a rat tail *collagen I* hydrogel that showed promise but needed to be validated for self-renewal and multipotency. I sought to employ genetic lineage tracing, used to validate the 3D organoid culture platform, and immunohistochemical biomarker staining to confirm the presence of true IESCs (Appendix B: Fig. 1).<sup>57,60,103–105,62,64,97–102</sup>

## **Developing a high throughput microfabricated IESC culture platform to describe intrinsic and extrinsic regulation of stem cell growth**

Due to the difficulties concerning sampling in 3D space, conventional organoid-growth based assays preclude statistically meaningful studies of clonal IESCs or IESC–niche cell co-cultures, limiting genetic analysis of single IESCs and their organoid progeny. Platforms facilitating clonal stem cell studies have driven our understanding of renewal in the hematopoietic system and mammary glands. The lack of similar tools in the IESC field has hindered our understanding of key niche interactions like IESC-PC signaling. PCs have been shown to increase IESC organoid formation *in vitro* but studies relied on the co-culture of hundreds of IESCs with hundreds of PCs. These interactions may not reflect physiologically normal signaling, where much smaller numbers of IESCs (~15) and PCs (~8) interact in the crypt base.<sup>7,106–110</sup>

Understanding how IESCs self-renew and differentiate is essential for determining the mechanisms underlying a broad range of issues related to human health and disease. Although *in vivo* lineage tracing and genetic manipulation remain important techniques for the analysis of IESC behavior, developments in primary IESC culture have expanded the toolkit available to study mucosal physiology to include powerful, complementary *in vitro* assays. Array-based technologies are emerging as a powerful method to study the functional characteristics of single and/or small numbers of stem cells in the hematopoietic system and holds similar promise for epithelial tissues such as the intestine. We developed a platform to study large numbers of single IESCs simultaneously, either at the clonal level or in the presence of niche cells, using microfabricated arrays (Fig. 1).<sup>7,106–110</sup>

Microfabricated culture arrays were modified for long-term 3D culture to capture and functionally assay clonal IESCs and IESC–niche cell co-cultures, effectively providing a platform for high throughput niche reconstruction using primary IESCs and niche cells. Rafts fabricated into the array wells allows for efficient retrieval of single IESCs and developed organoids for direct integration into conventional high throughput biochemical assays (Fig. 2).<sup>7,106–110</sup>

## **Methods/Materials**

### **Reconstructing basal-luminal signaling gradients *in vitro* and measuring gradient influences on organoid compartmentalization**

#### **The Sox9<sup>EGFP</sup>: Cag<sup>DsRED</sup> mouse model**

The Cag<sup>DsRED</sup> mouse line ubiquitously expresses the red fluorescent protein DsRed driven by the chicken beta-actin promoter. The Sox9<sup>EGFP</sup> mouse line possesses the Sox9 promoter controlling EGFP (enhanced green fluorescent protein) expression integrated using a modified bacterial artificial chromosome. Crossing these two transgenic lines provides an epithelium source where DsRED expression marks all cell types and low expression levels of EGFP marks CBC IESCs (Fig. 1D).<sup>92</sup>

#### **Isolation of Crypts from Mouse Colon**

Epithelial cells were dissociated from whole murine colons using previously described techniques with some modifications. Colons were resected, opened longitudinally and rinsed in PBS. Colons were cut into 10 mm segments and transferred to 3 mM EDTA (Sigma), 10 μM Y-27632 (Selleck) and incubated for 45 min at 4°C with gentle agitation. Fragments were transferred into fresh PBS with 10 μM Y-27632 and shaken by hand for 2 min to release the epithelial layer from the submucosa.<sup>92</sup>

## Isolation of Single Colonic Stem Cells

Epithelial cells were dissociated from whole murine colons using previously described techniques with some modifications<sup>111</sup>. Colons were resected, opened longitudinally and rinsed in PBS. Colons were cut into 1 mm segments and transferred to 3 mM EDTA (Sigma), 10  $\mu$ M Y-27632 (Selleck) and incubated for 45 min at 4°C with gentle agitation. Fragments were transferred into fresh PBS with 10  $\mu$ M Y-27632 and shaken by hand for 2 min to release the epithelial layer from the submucosa. Epithelium was separated from the remnant mucosa, washed twice in phosphate buffered saline (PBS) and dissociated to single cells in 0.3 U/mL dispase (Life Technologies), 10  $\mu$ M Y-27632 in Hank's Buffered Saline Solution (HBSS, Life Technologies) incubated at 37 °C for 10-14 min while shaking every 2 min. Cell solutions were passed sequentially through 100  $\mu$ m, 70  $\mu$ m, and 40  $\mu$ m pore-size nylon filters before being transferred to intestinal stem cell (IESC) culture media (Advanced DMEM/F12 (Life Technologies), N2 (1x, Life Technologies), B27 (1x, Life Technologies), Glutamax (1x, Life Technologies), penicillin (100 unit/mL, Life Technologies), and streptomycin (100  $\mu$ g/mL, Life Technologies), 10 mM HEPES (Life Technologies), 10  $\mu$ M Y27632 (Selleck Chemicals) and 500 mM N -acetyl- cysteine (Sigma)).

## **Developing self-renewing monolayers of primary colonic epithelial cells**

### *Lgr5*<sup>EGFP</sup>*CreERT2**xR26*<sup>confetti</sup> mouse

*Lgr5*<sup>EGFP-IRES-creERT2</sup> mice were generated by targeted insertion of the EGFP-IRES-creERT2 cassette into the ATG of the *Lgr5* allele. This generated mice where EGFP expression mosaically marked *Lgr5*<sup>+</sup> cells in multiple tissues. This transgene was

crossed onto the Rosa26<sup>Confetti</sup> transgenic line where a strong CAGG promoter was integrated into the *Rosa26* allele followed by a LoxP-flanked NeoR-cassette blocking transcription. This was upstream of the Brainbow-2.1 cassette<sup>112</sup>. Cre-mediated recombination removes the transcriptional roadblock allowing expression of one of the four fluorescent marker proteins, stochastically driven by the CAGG promoter, allowing discrimination between the clonal progeny of neighboring IESCs within the same crypt.

#### Monolayer culture of colonic crypts

The crypts were placed on top of the collagen hydrogel at a density of 1000 crypts/cm<sup>2</sup> (unless otherwise stated) and cultured in 4 mL medium per well in the 6-well plate. The medium was changed every 48 hours, and Y-27632 was added for the initial 48 hours of culture. When the cell coverage was greater than 80% (typically after 3–4 days for mouse cells, 5–7 days for human cells), the monolayers were sub-cultured by a gentle 2-step dissociation method. The first step was to lift the monolayer from the collagen hydrogel by scraping the collagen (with cells) from the well and transferring the hydrogel to a 15-mL conical tube containing 1 mL culture medium with 500 U/mL collagenase (type IV; Worthington Biochemical, USA). The gel was broken into small pieces by pipetting using a 5-mL serologic pipette, followed by a 1-mL pipet tip. The tube was then incubated at 37°C for 10 minutes to completely digest the collagen gel. The monolayers were rinsed with PBS buffer and pelleted by centrifugation at 600g for 1 min. The second step further breaks apart the monolayer pieces into smaller fragments by incubating the pellet in 150 mL of 0.5 mM EDTA and Y-27632 (10 µM) in PBS at 37C for 2 minutes (mouse cells) or 5 minutes (human cells). The monolayers were broken into small fragments by pipetting up and down 30 times by using a 200-mL

pipet tip. The cell fragments were resuspended in medium and subcultured on a new collagen hydrogel at a passage ratio of 1:3. To convert 3D organoids to a 2D monolayer, the organoids were extracted from Matrigel by detaching the Matrigel patty, breaking it into coarse pieces, and then pipetting the suspension by using a 200- $\mu$ L pipet tip. The cells were then cultured on a collagen gel at a density of 10 organoids/cm<sup>2</sup>.

### Genetic lineage tracing from IESCs in 2D culture

Lineage tracing was induced in adult *Lgr5*<sup>EGFP-IRES-creERT2</sup> mice by interparitaneal injection of 2mg of 4-hydroxy tamoxifen 24 hours prior to sacrifice and resection.

### **Developing a high throughput microfabricated IESC culture platform to describe intrinsic and extrinsic regulation of stem cell growth**

#### Clonal stem cell culture

Isolated IESCs were plated in CRAs (Cell Microsystems, USA) at ratios of ~1.5 cells per microwell. Sorted cells were added to array reservoirs in culture media and cells were seeded into microwells by centrifugation at 51g for 5 min at 4°C. Following centrifugation, medium was gently aspirated and arrays were overlaid with 600  $\mu$ l (2 reservoir array) or 200  $\mu$ l (4 reservoir array) of Matrigel and growth factors. Arrays were centrifuged a second time at 51g for 5 min at 4°C, to recapture any cells displaced by the addition of Matrigel. Matrigel was allowed to polymerize for 30min at 37°C before being overlaid with 1ml (2 reservoir array) or 600 $\mu$ l (4 reservoir array) of culture media. Matrigel for validation experiments contained previously described growth factors, with some modification, at the time of plating: 15  $\mu$ M Jagged-1 peptide (AnaSpec, USA), 750 ng/ml EGF (R&D, USA), 100 ng/ml Noggin (Peprotech, USA) and 500 nM LY2157299

(Selleck Chemicals, USA). Initial media in validation experiments contained 2.5  $\mu$ M CHIR99021 (Selleck Chemicals, USA) and 2.5  $\mu$ M Thiazovivin (Selleck Chemicals, USA). Growth factors were added at two-day intervals: 1  $\mu$ M Jagged-1 peptide, 50 ng/mL EGF, 100 ng/mL Noggin and 1  $\mu$ g/ml RSPO1 (R&D, USA). Medium was changed every four days, and no CHIR99021 or Thiazovivin was used past initial plating.<sup>57,113</sup>

### Stem cell niche co-culture

Isolated IESCs and PCs were plated in CRAs (Cell Microsystems, USA) at ratios of  $\sim$ 1.5 cells per microwell for IESCs and  $\sim$ 1 cell per 2 microwells for PCs. Sorted cells were added to array reservoirs in culture media and cells were seeded into microwells by centrifugation at 51g for 5 min at 4°C (Fig. 1E). Following centrifugation, medium was gently aspirated and arrays were overlaid with 600  $\mu$ l (2 reservoir array) or 200  $\mu$ l (4 reservoir array) Matrigel and growth factors. Arrays were centrifuged a second time at 51g for 5 min at 4°C, to recapture any cells displaced by the addition of Matrigel. Matrigel was allowed to polymerize for 30 min at 37°C before being overlaid with 1 ml (2 reservoir array) or 600  $\mu$ l (4 reservoir array) IESC Sort/Culture Media. In IESC/PC co-culture experiments, growth factors, minus Jagged-1 peptide and Y27632, were supplemented every two days, and medium was changed every four days, as previously described.<sup>57,113</sup>

### CRA image acquisition

Microwell arrays were tile-scanned in bright-field, GFP and DsRed wavelengths using an automated stage and the Scan Slide function in the Metamorph Imaging Suite (Molecular Devices) immediately after plating and overlaying media. Arrays were housed in a physiological chamber mounted on a fluorescent microscope during

imaging, to prevent cell death due to the imaging procedure. Scanned images were stitched into a single composite image using the open source image analysis suite FIJI and then segmented into address-associated individual well images using an algorithm, 'Segmenter.m' , designed in MATLAB (MathWorks, USA). The 'Segmenter.m' is available for download at <http://www.magnesslab.org/#!vstc1=page-1/vstc0=software-downloads>.

### CellProfiler 2.0 analysis.

Computational analysis of initial microwell contents was carried out in CellProfiler 2.0 (Broad Institute) in two steps: segmented microwell images were loaded in sequence into CellProfiler to determine the contents of each microwell of the array; (2) raw data generated by CellProfiler was converted into easily interpretable graphs and tables showing the desired location, survivability or growth of IESCs within the array culture. Our analysis pipeline ('SCPipeline.cp') was assembled using modules in the open source image analysis software package CellProfiler 2.0 (available for free download at <http://cellprofiler.org>). Autofluorescence and reflections off microwell walls distort the processed microwell images and can reduce the accuracy of stem cell identification. Raw images loaded into CellProfiler undergo thresholding using the 'MoG Global' method, which separates objects from background on the basis of an estimate of the amount of the image occupied by objects. The image occupation of a single cell was estimated from 10 microwell images and the threshold correlation factor was increased to prevent background identification. A Laplacian of Gaussian algorithm, which is best used for objects with increasing pixel intensity towards their center (such as DsRed+ cells), was used to distinguish between single and clumped objects. To establish

parameters for cell identification and debris discrimination, we randomly selected 500 individual microwell images containing single IESCs and 500 individual microwell images containing debris or fluorescent noise from a two-chamber microwell array containing Sox9<sup>EGFP</sup>: Cag<sup>DsRed</sup> IESCs (Fig. 3C). All analysis was conducted on the DsRed wavelength, because the CAG promoter produced a significantly stronger fluorescent signal than the Sox9<sup>EGFP</sup> BAC transgene. These images were subjected to general size/shape analysis in the CellProfiler 2.0 module 'MeasureObjectSizeShape', which compiled data on the objects' shape and location characteristics. We focused on three specific parameters to develop an analytical pipeline in CellProfiler to identify IESCs: compactness, form factor and eccentricity. After applying standard image thresholding, CellProfiler identified objects in each microwell in our panel of 1,000 images, and we found that IESCs had a distribution of values that was distinct from debris/noise for each of our parameters of interest (Fig. 3D-F). Thresholds were set using these distribution curves to identify IESCs within total identified objects using the 'FilterObjects' CellProfiler module (Fig. 3G). The complete pipeline was named 'SCPipeline.cp'. A similar approach was used to establish filtering parameters for PC identification. Data on identified objects and filtered cells contained in each microwell image were exported using the 'ExportToSpreadsheet' CellProfiler module and processed using Microsoft Excel for Mac 2011 (Microsoft, USA). The object delineated data exported by CellProfiler are converted to well-delineated data using 'WellContents.xls', which shows the initial contents of each microwell, the distribution of IESC and PC containing wells in the array, and the addresses of microwells containing cells with no debris or fluorescent noise. Comparison of pre- and post-filtering microwell contents in 'WellContents.xls'

allowed us to identify the microwell images containing only intact stem cells and no debris (Fig. 3G). To validate our IESC identification pipeline using unbiased microwell images, we manually scored the contents of 2,254 randomly selected microwells. This panel of images was then subjected to analysis using our newly developed pipeline, which was able to identify initial microwell contents with a high degree of accuracy, especially for microwells containing a single IESC (99.87% accurate; Fig. 3H). Owing to stringency settings, this accuracy was reduced for wells containing multiple cells. Source files for 'Segmenter.m' , CellProfiler 2.0 pipeline 'SCPipeline.cp' and 'WellContents.xls' are available here as Supplementary Software and for download at <http://www.magnesslab.org/#!vstc1=page-1/vstc0=software-downloads>.

#### Data analysis of CellProfiler results

After the well contents are determined by automated analysis, "cell per microwell" data is extracted from the .csv file generated in "SCPipeline.cp" using the "WellContents.xls" file (available at magnesslab.org). Data from the "SCPipeline.cp" generated .csv file (this file has a name generated by the user, see "CellProfiler image analysis", step 3) is copied into the WellContents.xls file. Per-microwell contents of the CRA are automatically extracted through formatting expressions built into the WellContents.xls file and displayed on the sheet titled "WellDelineated". The microwell addresses are displayed in the sheet titled "target wells", and grouped by microwell content (intact cells only; microwells with debris are excluded) as follows: column A= 1 cell; column B= 2 cell; column C= 3 cell; column D= 4 cell. Data summary graphics, showing the distribution of cells within the CRA are displayed in the sheet titled "Distribution". Source files for 'Segmenter.m' , CellProfiler 2.0 pipeline 'SCPipeline.cp'

and 'WellContents.xls' are available here as Supplementary Software and for download at <http://www.magnesslab.org/#!/vstc1=page-1/vstc0=software-downloads>.

#### Manual analysis of initial micraft contents.

For experiments examining organoid survival relative to initial cell-to-cell contact, tile-scanned images of CRAs in EGFP and DsRed wavelengths were overlaid and manually scored by micraft address. DsRed<sup>+</sup> cells (isolated as Sox9<sup>EGFP</sup>neg :CAG<sup>DsRed</sup>+ :CD24<sup>High</sup>:SSC<sup>High</sup>) were considered 'PCs' and EGFP<sup>+</sup> cells (isolated as Lgr5<sup>EGFP</sup>high or Sox9<sup>EGFP</sup>low ) were considered 'IESCs'. Two or more cells were scored as 'in contact' only if their fluorescent signatures were contiguous in the overlaid images. For manual quantification of well contents and organoid survival, all investigators were blinded to prior well contents and survival outcomes.

#### Statistical analysis of organoid formation.

For cell number experiments, conditional logistic regression was performed with the number of organoids alive at t = 120 hr as the response and the number of IESCs and PCs present in initial well contents as predictors. This was done separately for each experiment as well as separately for each replicate within separate experiments. When analysis was conducted across both replicates in a single experiment, a term indicating individual wells was included in the model to account for well-to-well variability. To examine whether IESC survival was related to cell contact or cell type (IESC or PC), we performed a logistic regression with organoid survival at t = 120 hr as the response and each combination of cell contact and cell type (IESC, no contact; IESC-PC, no contact; IESC-IESC contact; IESC-PC contact) as the predictor. An overall test was performed to examine whether there was any difference in survival amongst the four groups. If

overall significance was found then pairwise tests were also performed. Wells were considered independent and therefore it was not necessary to model the correlation between them. No statistical method was used to predetermine sample size and experiments were non-randomized. All analyses were performed using SAS Version 9.3 (SAS Institute). P values less than 0.05 were considered statistically significant.

Quantification of cell movement in micrafts. For cell movement experiments, pairs of PCs, IESCs, and IESC–PC pairs were identified in micraft images at  $t = 0$  hr. Distance between each cell in a pair was measured at  $t = 0$  and  $t = 24$  hr. Relative change in distance ( $d^\Delta$ ) was calculated by subtracting distance at  $t = 24$  hr ( $d^{24}$ ) from distance at  $t = 0$  hr ( $d^0$ ) and normalizing to  $d^0$  (Fig. 4). Pairs of cells were included in the experiment only if they were alive at  $t = 24$  hr, based on the presence of EGFP or DsRed fluorescence. Distances were measured from the center of each cell to account for changes in cell size. Statistics were analyzed in Prism 6 (GraphPad) by one-way ANOVA with Tukey's multiple comparisons test. To control for measurement error, primary intestinal epithelial cells were isolated and fixed in 4% PFA for 30 min at room temperature, rinsed three times in PBS, and plated in CRA. Distance between fixed cell pairs ( $n = 50$ ) was calculated as per live cells, above. Results from the fixed cell experiment were compared with each group of live cell pairs by unpaired Student's t-test to determine statistically significant movement.

## **Results**

### **Reconstructing basal-luminal signaling gradients *in vitro* and measuring gradient influences on organoid compartmentalization**

#### **A *Wnt3a/R-Spondin1* gradient enhances polarization of the stem/progenitor cell compartment**

The highest levels of Wnt activity are thought to exist in the crypt base with the Wnt concentration tapering off in a gradient toward the luminal surface. *R-Spondin1* (*Rspo1*) is co-expressed with Wnts in the stem cell zone and functions to potentiate Wnt activity through its receptor LGR5, which is G-protein coupled receptor expressed almost exclusively in colonic stem cells<sup>114</sup>. To determine whether a dual gradient of Wnt-signaling along the microchannel might promote enhanced polarization of proliferative and differentiated cellular compartments, *R-Spondin1* and *Wnt3a* were placed at high concentration in the source reservoir (75 ng/mL *Wnt3a*, 110 ng/mL *R-Spondin1*) to generate an environment with a steep factor gradient. To assess whether a *Wnt3a/R-Spondin1* gradient enhanced polarization of the stem/progenitor and differentiated compartments, Sox9<sup>EGFP</sup> and EdU location was measured in each colonoid under the dual factor gradient. Nearly all the 24 colonoids assessed displayed IESC patterning with a Sox9<sup>EGFP</sup> vector that orientated toward the source reservoir containing *Wnt3a/R-Spondin1*. Polarization was not related to its location in the microchannel. Nearly all of the colonoids assessed also showed proliferative polarity with an EdU vector oriented towards the *Wnt3a/ R-Spondin1* source. (Appendix A: Fig. 5)

## Effect of a *Wnt3a/R-Spondin1* Gradient on Growth and Polarization of Colonoids Derived from a Single Stem Cell

The experiments above utilized multicellular colonoid fragments or whole crypts as the source material for development of colonoids. While the fragments were small (~30  $\mu\text{m}$  diameter with ~25 cells), the fragments did contain many cell types (differentiated, stem, and TA cells), and thus may have had pre-established cellular interactions that might impact spatial lineage allocation of a colonoid developing under an externally imposed growth-factor gradient. All evidence to- date indicates that the cells within these colonoids are representative of those *in vivo* and maintain a normal karyotype, it is conceivable that the cultured colonoids differ in an as yet unknown manner from their *in vivo* counterparts<sup>64,90,115</sup>. For this reason, single stem cells were isolated from freshly obtained Sox9<sup>EGFP</sup>-CAG<sup>DsRed</sup> mouse crypts by fluorescence-activated cell sorting of the stem cells (Sox9<sup>EGFP</sup>Hi:CAG<sup>DsRED</sup>)<sup>120</sup>. The stem cells suspended in Matrigel were loaded into a microchannel and cultured for 5 days in the presence of a *Wnt3a/R-Spondin1* gradient. The Sox9<sup>EGFP</sup> polarization was significantly exaggerated in the single-cell-derived colonoids with expression vectors of 20 of the 23 colonoids assessed pointing towards the gradient source. (Appendix A: Fig. 6)

### **Developing self-renewing monolayers of primary colonic epithelial cells**

#### Lineage Tracing confirms the presence of stem cells

To determine whether self-renewing colonic stem cells persisted in the 2D monolayers, we performed genetic lineage tracing by using the Lgr5<sup>EGFPCreERT2</sup>xR26<sup>Confetti</sup> transgenic mouse. Colonic crypts were isolated from a tamoxifen-treated Lgr5<sup>EGFPCreERT2</sup>xR26<sup>Confetti</sup> mouse and plated on the surface of

collagen hydrogel at a low density of 30 crypts/cm<sup>2</sup> (to track the growth of individual crypts). At 24 hours after plating, tracing events (4 out of 3000 crypts) expressed *red fluorescent protein* (RFP), which marked them as derived from Lgr5 stem cells (Appendix B. Fig. 4). The *RFP+* regions expanded into large red fluorescent patches inter-mixed with the progeny of non-fluorescent stem cells. *RFP+* cells were isolated from 2D patches and subcultured to determine whether the *RFP+* patches contained cells with colonic stem cell properties. The *RFP+* cells continued to expand into patches composed only of *RFP+* cells (Appendix B. Fig. 4). The *RFP+* cell monolayers possessed proliferative (EdU+) cells and all the differentiated cell types: goblet cells (*Muc2+*), enteroendocrine cells (*ChgA+*), and absorptive colonocytes (*ALP+*) (Appendix B. Fig. 4). These data demonstrate that the 2D monolayers possessed *Lgr5+* IESCs that expanded as a proliferative monolayer and produced differentiated descendants in vitro. (Appendix B: Fig. 5)

## **Developing a high throughput microfabricated IESC culture platform to describe intrinsic and extrinsic regulation of stem cell growth**

### CRAs are adaptable to intestinal stem cell culture and imaging

Previously described polydimethylsiloxane (PDMS)/polystyrene CRAs could be used to isolate and culture single IESCs in 3D embedded in ECM hydrogel. As IESCs require several days to develop into organoids, CRAs had to be amenable to media changes<sup>13,57</sup>. To meet these requirements, polycarbonate cassettes, with dividers to create multiple media reservoirs, were bonded to CRAs (Fig. 1A,B). Cassettes were fabricated with two or four culture chambers (~2,500 or 5,000 microwells per culture chamber, respectively). Physical well addresses, stamped into PDMS at 5-microwell

intervals, were included in the array design to allow for tracking. Conventional IESC cultures are capable of supporting organoid growth for many weeks. IESCs were maintained up to 8 weeks in CRAs, with retention of organoids in their original micrafts (Fig. 1L). At 8 weeks, organoids had grown into large structures containing many crypts (Fig. 1L,M). These observations demonstrate feasibility for long-term CRA-based culture of primary IESCs.

Tile-scanning microscopy produced high-resolution images of whole CRAs for downstream analysis.

Tile-scanning of the CRA in the DsRed wavelength immediately after plating and at 48 hr revealed that isolated IESCs had begun to produce primitive organoids, indicative of biocompatibility (Fig. 1F,I). Large, high-resolution mosaic images of the entire array surface could be segmented into indexed individual micraft images using the segmentor.m script, referencing the micraft location on the array surface in the micraft image file name.

Post hoc image analysis can quantify micraft contents and identify micrafts containing specific numbers of cells

To rapidly assess the cellular contents in each of the micrafts, we developed a computational pipeline with the following analytical goals: to identify micrafts containing IESCs; exclude empty micrafts; exclude micrafts containing debris or imaging artefacts; and quantify the number of IESCs per micraft. To achieve this, we developed an image analysis computational pipeline (Fig. 3A) that was able to accurately identify micrafts containing targeted initial cellular contents. Computational analysis could accurately quantify the cellular contents of each micraft especially for

single IESCs (99.87%; n=2,258 visually validated; Fig. 3H). Owing to stringency settings adapted specifically for clonal analysis, the percentage of identified microrrafts was reduced for wells containing multiple cells, but the incidence of falsely identified microrrafts remained 0% for all cell numbers examined (Fig. 3H,I).

#### Cell-cell contact is required for increased organoid formation in vitro

As previous studies have speculated that PC-secreted Wnts are responsible for enhancing IESC growth in vitro, IESC–PC co-culture experiments were carried out in the absence of exogenous Wnt, to avoid ‘masking’ the potential impact of PCs on organoid formation<sup>57,113,116</sup>. The GSK3 $\beta$  inhibitor CHIR99021, a Wnt agonist, was also excluded from co-culture experiments. To address the possibility that a PC in one microrraft might affect the growth of an IESC in an adjacent, but separate microrraft, we modelled diffusion dynamics of cell-secreted molecules in CRAs. Diffusion between microrrafts was deemed negligible under models relying on liberal rates of diffusion and decay<sup>115</sup>. We reasoned that increased numbers of PCs would result in increased secretion of *Wnts* and IESC growth, and examined microrrafts with initial contents consisting of any combination of 1–5 IESCs and 0–2 PCs. IESCs were isolated from Sox9<sup>EGFP</sup> or Lgr5<sup>EGFP</sup> mice and PCs from Sox9<sup>EGFP</sup>:CAG<sup>DsRed</sup> mice (Fig. 4A). DsRed fluorescence was used as a readout of IESC contamination in PC populations. Replicate experiments were conducted for each IESC biomarker to increase sample size per IESC–PC combination, and data were analyzed from four total CRA experiments, consisting of 4,830 data points, each corresponding to an individual microrraft containing any combination of IESCs and PCs (Fig. 4B,C). Surprisingly, examination of survival percentages across all combinations of IESCs and PCs

revealed no statistically significant trends, regardless of whether IESCs were isolated using Sox9<sup>EGFP</sup> or Lgr5<sup>EGFP</sup> (Fig. 4B,C). To investigate the overall effect of PCs on organoid survival, we next analyzed the percentage of organoids formed in micrafts containing any number of IESCs or any number of IESCs with any number of PCs (Fig. 4D). These analyses also failed to produce statistically significant differences between IESC-alone and IESC-PC micrafts, suggesting that PC presence alone is insufficient to increase organoid formation in vitro at physiologically relevant numbers. Previous studies have suggested that cell-to-cell contact between IESCs and PCs may influence organoid formation, but this has not been formally tested by comparison between touching and non- touching IESCs and PCs<sup>113</sup>. Using the same data generated in our IESC-PC co-culture experiments, we reanalyzed initial CRA contents to classify micrafts by cell-to-cell contacts at t = 0 hrs and correlated this status with organoid formation outcome (Fig. 4F). This comparison yielded results with overall statistical significance (conditional logistic regression, P = 0.0282), indicating that IESCs in direct contact with PCs are more likely to form organoids than IESCs alone, or IESC-PC wells that are not in direct contact. Interestingly, IESC-IESC contact events were also more likely to form organoids than non-touching IESCs, suggesting that cell-to-cell contact between two or more IESCs may also positively influence organoid formation. As expected, PC-PC contact did not result in the formation of organoids, consistent with the post-mitotic status of PCs in vivo and the high level of purity observed in PC populations (Fig. 4G).

### Single cells do not form de novo contacts after plating

The contact-dependent effects on organoid formation prompted us to examine whether *de novo* cell–cell contacts occurred after initial classification as ‘non-touching’ at  $t = 0$  hrs. To assay this, we measured the distance between IESC–IESC, IESC–PC and PC–PC pairs in microwell images acquired at  $t = 0$  hrs and calculated positive or negative changes in cell–cell distance at  $t = 24$  hrs (Fig. 5A). Microwells in which both cells were alive at 24 hrs were included for analysis, resulting in  $n=905$  pairs (521 IESC–IESC; 345 IESC–PC; 39 PC–PC; Fig. 5B). To control for background movement due to known changes in extracellular matrix integrity that occur over time, measurements were taken on pairs of fixed intestinal epithelial cells for comparison ( $n=50$ ). Analysis of change in distance in alive pairs demonstrated that: cell movement was statistically significant compared with measurements taken on pairs of fixed cells; and no observed cells formed *de novo* contacts after initial plating of CRAs. Interestingly, non-touching pairs of cells with an initial cell–cell distance  $\leq 25 \mu\text{m}$  seem to grow further apart within the first 24 hr of culture (Fig. 5C). Together, these data demonstrate that single cells migrate within Matrigel cultures and that cell–cell signaling may repel single cells from one another over short distances *in vitro*. Previous studies demonstrate significant organoid movement and merging *in vitro*<sup>124</sup>. To further examine cell movement in the CRA platform, we performed time-lapse imaging of microwells. Single cells demonstrated appreciable movement as they developed into organoids over the first 24 hrs of culture. Larger clumps of cells merged into single organoids, suggesting that the movement and merging of IESCs *in vitro* may be influenced by cell number or heterogeneity within populations.

## **Conclusions**

### **Reconstructing basal-luminal signaling gradients *in vitro* and measuring gradient influences on organoid compartmentalization**

Microfabricated platforms can produce steep linear gradients of morphogenic factors across individual colonoids or single stem cells recapitulating the crypt axis. A simple linear gradient of *Wnt3a*/*Rspondin1* was sufficient to induce polarization of the proliferative and differentiated cellular architecture in colonoid tissue constructs derived from both single colonic stem cells and small multicellular colonoids composed of heterogeneous cell types. Combining a *R-Spondin1* (110 pg/mL/ $\mu\text{m}$ ) gradient with a *Wnt3a* (75 pg/mL/ $\mu\text{m}$ ) gradient acted synergistically to produce enhanced polarization of the colonoid body. Maintenance of colonoids derived from single stem cells under the combined gradient condition produced the most highly polarized colonoid structure suggesting that the multicellular fragments possessed some internal patterning which limited the ability of derived colonoids to maximally respond to morphogenic gradients. (Appendix A: In Vitro Polarization of Colonoids to Create an Intestinal Stem Cell Compartment)

### **Developing self-renewing monolayers of primary colonic epithelial cells**

The Allbritton lab developed a self-renewing, 2D monolayer derived from primary intestinal tissue and possessing all cell lineages found within the colon. Remarkably, the monolayers self-pattern to create peripheral stem/proliferative and central differentiated cell zones. The interior of the monolayer yields a large surface area occupied predominantly by differentiated cells, a feature mimicking that of the intestinal surface area *in vivo*. Genetic lineage tracing from the *Lgr5*<sup>EGFP<sup>CreERT2</sup></sup> allele is the gold standard

in the GI field to validate the presence of potent IESC populations<sup>11</sup>. Confirming that *Lgr5*<sup>+</sup> IESCs are present in the monolayer culture systems validates their use as an alternative to embedded organoid cultures in a platform to study the apical mucosa surface more readily manipulated by addition of compounds to the media. This structure enables facile assay of drugs, toxins, and metabolites using conventional cell-based assay systems, not possible in the embedded organoid systems.(Appendix B: Appendix B: Self-renewing Monolayer of Primary Colonic or Rectal Epithelial Cells) <sup>38</sup>

### **Developing a high throughput microfabricated IESC culture platform to describe intrinsic and extrinsic regulation of stem cell growth**

CRA has broad applicability to assaying stem cell–niche interactions and organoid development and serve as a high throughput culture platform to interrogate gene expression at initial stages of stem cell fate choices. Stem cell niches provide critical extrinsic signals that govern stem cell self-renewal and differentiation, but their anatomical locations and complexity often present significant challenges to the study of stem cell renewal *in vivo*. PCs express soluble and insoluble IESC niche signaling components, including Wnt and Notch ligands<sup>113,116</sup>. We examined the impact of PC presence and contact with IESCs on organoid formation. Interestingly, we find that PC presence alone is not predictive of organoid formation. Rather, direct cell-cell contact between IESCs and PCs is required for enhanced IESC growth, suggesting that insoluble or very short-range soluble signals support IESCs *in vitro*. These results support *in vivo* findings that stemness is most strongly correlated in cells that exist in intimate contact with PCs, and provide insight into the functional role of PCs in maintaining stemness<sup>117</sup>. Importantly, the CRA platform was critical in testing dose and

contact dependency of PCs in a microscale format. in maintaining stemness. Importantly, the CRA platform was critical in testing dose and contact dependency of PCs in a microscale format.

Array-based stem cell culture platforms are growing in use and present an efficient and cost-effective alternative to conventional cell culture<sup>126,127</sup>. However, most platforms are not amenable to long-term cultures, such as required for the development of IESC-derived organoids and other self-assembled, stem-cell-derived organoids. CRAs facilitate the culture of thousands of primary stem cells over many days and weeks as well as high throughput reconstitution of the stem cell niche at physiologically relevant cell numbers. The power of the CRA platform is further highlighted by the ability to retrospectively 'mine' existing high throughput CRA data sets to test new hypotheses, such as niche cell dose dependency, cell-cell contact and cellular movement within micrafts.<sup>106,107,114</sup>

CRAs provide robust methodology for screening candidate mitogens and morphogens for their effect on organoid formation and development, and the study of other IESC niche cells, such as pericryptal myofibroblasts, endothelial cells and neurons. Furthermore, CRAs have broad potential for in vitro reconstruction of stem cell niches across a range of cell and tissue types, especially those that require three-dimensional extracellular matrices. The ability to easily retrieve a high replicate number of organoids early in their development allows investigators to associate functional observations with dynamic changes at the genetic and transcriptomic level, facilitating next-generation forward genetic screens in primary stem cells.<sup>106,107,114</sup>

## Chapter 3: A High throughput Organoid Microinjection Platform to Study Gastrointestinal Microbiota and Luminal Physiology

### Synopsis

A high-throughput organoid microinjection platform was developed to study gastrointestinal physiology and the microbiome. Monitoring and quantification of injected microbes and other cargos was achieved by automated imaging. Human fecal microbiota including highly oxygen-sensitive anaerobic taxa were transplanted into the organoid lumen and maintained over time in stable monocultures or microbial communities.

### Overview

**Aims:** The human gut microbiota is becoming increasingly recognized as a key factor in homeostasis and disease. The lack of physiologically relevant *in vitro* models to investigate host-microbe interactions is considered a substantial bottleneck for microbiota research. Organoids represent an attractive model system because they are derived from primary tissues and embody key properties of the native gut lumen; however, access to the organoid lumen for experimental perturbation is challenging. Here, we report development and validation of a high-throughput organoid

Parts of this chapter previously appeared as an article in the journals NCB, Plos1, and CMGH the original citations are as follows:

Gracz, A. D. et al. A high-throughput platform for stem cell niche co-cultures and downstream gene expression analysis. *Nat. Cell Biol.* 17, 340–349 (2015).

Attayek, P. J. et al. Automated microraft platform to identify and collect non-adherent cells successfully gene-edited with CRISPR-Cas9. *Biosens. Bioelectron.* 91, 175–182 (2017).

Wang, Yuli, DiSalvo, Matthew, Gunasekara, Dulan B., Dutton, Johanna, Proctor, Angela, Lebhar, Michael S., Williamson, Ian A., Speer, Jennifer, Howard, Riley L., Smiddy, Nicole M., Bultman, Scott J., Sims, Christopher E., Magness, Scott T. & Allbritton, Nancy L. Self-renewing Monolayer of Primary Colonic or Rectal Epithelial Cells. *CMGH* 4, 165–182.e7 (2017).

Williamson, Ian A., Arnold, Jason W., Samsa, Leigh Ann, Gaynor, Liam, DiSalvo, Matthew, Cocchiaro, Jordan L., Carroll, Ian, Azcarate-Peril, M. Andrea, Rawls, John F., Allbritton, Nancy L. & Magness, Scott T. A High-Throughput Organoid Microinjection Platform to Study Gastrointestinal Microbiota and Luminal Physiology. *Cell. Mol. Gastroenterol. Hepatol.* 1–38 (2018). doi:10.1016/j.jcmgh.2018.05.004

microinjection system for cargo delivery to the organoid lumen and high-content sampling. **Methods:** A microinjection platform was engineered using off-the-shelf and 3D-printed components. Microinjection needles were modified for vertical trajectories and reproducible injection volumes. Computer vision (CVis) and microfabricated CellRaft™ Arrays (CRAs) were used to increase throughput and enable high-content sampling of mock bacterial communities. COMSOL modeling predicted a hypoxic luminal environment that was functionally validated by transplantation of fecal-derived microbial communities and monocultures of a non-sporulating anaerobe. **Results:** CVis identified and logged locations of organoids suitable for injection. Reproducible loads of 0.2 nl could be microinjected into the organoid lumen at ~90 organoids/hour. CVis analyzed and confirmed retention of injected cargos in ~500 organoids over 18 hrs and revealed the requirement to normalize for organoid growth for accurate assessment of barrier function. CVis analyzed growth dynamics of a mock community of GFP- or DsRed-expressing bacteria, which grew within the organoid lumen even in the presence of antibiotics to control media contamination. Complex microbiota communities from fecal samples survived and grew in the colonoid lumen without appreciable changes in complexity. **Conclusions:** High-throughput microinjection into organoids represents a next-generation *in vitro* approach to investigate gastrointestinal luminal physiology and the GI microbiota. **Keywords:** Organoid, microinjection, high-throughput, fecal microbiota, anaerobic, barrier function, high-content sampling

## **Background & Aims**

The human gastrointestinal tract contains a remarkably dense and diverse microbial community<sup>38,118</sup>. The interactions between gut microbiota and host are becoming increasingly recognized as key factors in homeostasis and disease<sup>43</sup>. Many studies indicate that community imbalances, known as dysbioses, are associated with onset and progression of diseases including diabetes<sup>119</sup>, obesity<sup>120–122</sup>, colorectal cancer<sup>27,50,51</sup>, and inflammatory bowel disease (IBD)<sup>44</sup>. Despite tight statistical associations between dysbiosis and disease, the ability to formally test cause-and-effect relationships is severely limited by lack of *in vitro* experimental models that enable controlled interrogation of host-microbe interactions.

Sequencing of the 16S rRNA gene is routinely used to characterize microbial communities and is a powerful tool to identify bacteria that may contribute to disease<sup>32</sup>. While 16S rRNA gene sequencing provides a ‘signature’ of microbial composition within a community, alone it is insufficient to define specific microbial mechanisms that impact host biology. Germ-free (gnotobiotic) animal models are commonly used to investigate host-microbe interactions in a physiologically relevant system, but germ-free animal models are often impractical for researchers to employ because of the scarcity of gnotobiotic facilities and high cost of gnotobiotic experimentation<sup>13</sup>. Additionally, the inherent low throughput nature of germ-free rodent studies limits the ability to decipher the individual role that each microbial species plays in health and disease.

A recent assessment of microbiota research in the United States identified the development of high throughput tools as a key, common unmet need for this field<sup>14</sup>. With the recognition of this problem, concerted efforts are now being made to build a

'translational microbiome toolbox' to create innovative and high-throughput approaches to test detailed mechanisms of host-microbe interactions<sup>123</sup>. For instance, engineering *Bacteriodes thetaiotaomicron*, *B. fragilis*, *B. vulgatus*, *B. ovatus*, *B. eggerthii*, and *B. uniformis* with 6 different fluorescent proteins enabled delineation of species within the gut of mice, and revealed that the priority of gut colonization determines colonic crypt microbial occupancy<sup>124</sup>. Similarly, engineering inducible promoters in *Bacteroides* has enabled study of host-microbe interactions through measurement of commensal sialidase activity and liberation of mucosal sialic acid, a nutrient for pathogens<sup>125</sup>. Further, new methods have been developed that permit genetic manipulation and analysis of "genetically intractable" bacteria from the intestine<sup>126</sup>. As these sorts of tools are being increasingly developed to test mechanistic questions, and studies are expanded to interrogate the thousands of different microbes that inhabit the gut, high-throughput *in vitro* models will be essential for these next-generation microbiome studies.

Transplanting the complex microbial communities found in the gut lumen to a physiologically relevant system *in vitro* is particularly challenging since most microbes comprising the human GI microbiota are highly sensitive to oxygen exhibited limited viability or proliferative capacity in the presence of oxygen<sup>127</sup>. A recent study suggests that 50%-60% of the oxygen-sensitive bacterial genera in the GI microbiota can produce resilient spores and can be detected on specialized agar plates incubated in an anaerobic environment<sup>127</sup>, however, non-sporulating anaerobes remain difficult or impossible to cultivate *in vitro*, and require an environment sufficiently hypoxic for survival and growth<sup>127</sup>. Minibioreactors without a host cellular component have been

built to cultivate fecal samples in a hypoxic environment<sup>128</sup>. This system increased throughput by allowing up to 48 communities to be cultivated per anaerobic chamber. While this system proved sufficient to stably culture complex communities, only 15%-25% of the initial fecal OTUs were observed suggesting that other system components are required to cultivate the full complexity of fecal microbiota.

Designing culture environments that possess a host cellular component in combination with physiologically relevant luminal environment may enable more complex communities to be cultivated while facilitating the study of host-microbial interactions. Culturing techniques have been developed that permit growth of primary intestinal epithelium on 2D surfaces<sup>129-131</sup>, however, generating a steep oxygen gradient over a single cell layer in monolayer cultures remains an engineering challenge due to the requirement of a constantly intact monolayer, which is difficult to achieve in 2D cultures. Gut organoids, also known as enteroids or colonoids<sup>132</sup>, represent an alternative *in vitro* system to culture fecal derived microbiota by the virtue of their morphologic, cellular and physiologic properties that are unavailable in 2D culture systems.

Organoids are microscale spherical structures comprised of an epithelial monolayer that surrounds a hollow lumen containing mucous and cellular debris, and serves as a natural physical barrier to the ambient atmosphere<sup>57</sup>. Organoids form in culture from isolated crypts or single intestinal stem cells<sup>13,57,64,115,133</sup>, retain long-term self-renewal properties due to stable intestinal stem cells compartments (e.g. crypt buds) interspersed between zones of differentiated cells, and possess cell lineage ratios, polarization, and cell migration patterns that mimic those found *in vivo*<sup>64</sup>.

*Clostridium difficile*, a sporulating pathogenic anaerobe, has been microinjected and monocultured for 12 hours in the organoid lumen suggesting that the organoid luminal environment can support oxygen-sensitive sporulating taxa<sup>74,134</sup>. While organoids are a potentially suitable environment to model physiology of the gut lumen, microinjection currently represents the most direct method for delivering defined cargo to the lumen<sup>135</sup>.

In this study, we developed a high-throughput organoid-specific platform to study luminal physiology and the gut microbiome. We leveraged advances in organoid culture, microfabricated culture devices<sup>106,107,114</sup>, computer vision (CVis)<sup>114</sup>, and semi-automated microinjection technologies to enable high-content sampling of a number of microinjected cargos, including materials to study epithelial barrier integrity and fecal isolates from human donors. The platform can be extended to organoids derived from other tissues like the lung and stomach, and injectable cargos can be tailored to study a broad range of topics related to gut epithelial biology including microbe-microbe and host-microbe interactions, nutrient transport, and barrier function.

## **Results**

### **Development of an organoid injection system**

The apical side of the gut epithelium is exposed to a complex mixture of luminal contents including nutrients, microbiota, metabolites, and indigestible material. While there is merit to using the organoid lumen to model gut physiology, the apical surface of the organoid epithelium is inaccessible because the organoid epithelial monolayer creates a barrier to the luminal space (Fig. 6A). Material can be introduced into the organoid lumen by incubating fragments of dissociated organoid with compounds that are then passively enveloped into the organoid as the lumen re-forms<sup>135</sup>. Though this

technique can be effective, it lacks precision in that there is no control over the quantity of material that can be delivered to the organoid. Moreover, this strategy cannot be used to introduce materials into the lumen of mature organoids. Microinjection is an alternative approach that offers the ability to accurately, reproducibly, and precisely place a wide variety of cargos into the organoid lumen. However, microinjection is technically challenging and requires a high-level of expertise that limits its broad use by investigators.

Using common hardware with some simple modifications, we developed a semi-automated, high-throughput organoid microinjection system that can be easily reproduced in many laboratories. To develop this system, conventional remote-controlled microinjection hardware, and a fluorescent microscope fitted with an automated stage and imaging system were combined in a single platform (Fig. 6B). The system is contained within a physiologic chamber to maintain appropriate temperature and CO<sub>2</sub> levels to support long-term organoid viability for time intensive experiments (Fig. 6B). Three 3D-printed custom fittings were engineered to enable precise needle articulation over organoids cultured in conventional tissue culture plates or CRAs for high-throughput applications (Fig. 6B; CAD files available in Supplemental Materials)<sup>106,136</sup>.

Needle approach for pronuclear or zebrafish embryo microinjection typically occurs at a ~45° angle. These angles are incompatible with the use of multi-well plates because the walls of the wells prohibit needle articulation. Additionally, diagonal needle approaches result in an unacceptable level of needle breakage when moving the needle through the hydrogel that surrounds organoid. To circumvent these issues,

microinjection needles were fashioned from glass capillaries, then heated and bent to a 90° angle, allowing for a vertical needle approach to organoid targets (Fig. 6C). Positioning of the needle over the target organoid did not obstruct the microscope visual field due to the inverted orientation of the objective lens and optical clarity of the needle.

Accurate and reproducible microinjection requires high quality glass microneedles. We found that needle construction techniques for conventional zebrafish embryo microinjection produced needles that were not suitable for organoid microinjection and required substantial optimization<sup>137</sup>. Specifically, needle taper and tip length were increased to promote smooth entry and exit from the organoid and rapid re-sealing. Needle bore diameter was optimized to 1 µm to reduce the size of epithelial puncture and enable reproducible nanoliter injections (Fig. 6D). Preliminary attempts to inject organoids revealed that microforged needles were highly susceptible to retention of cellular material resulting in high incidence of clogging, and impaired insertion and removal of needles in subsequent injection attempts. At the microscopic level, the borosilicate needles are littered with microscopic defects<sup>137</sup>, which we surmised caused retention of cellular material on the needles after injection. Wet etching using HF was adapted to remove these defects and produce a smooth external needle tip<sup>137</sup>. A high internal pressure was maintained in the needle body during wet etching to reduce buildup of acid or salt residues that might cause clogging or contaminate cargos. These microneedle design features proved essential for efficient and reproducible high-throughput microinjection into organoids.

## Validating the organoid injection system

Precise and reproducible microinjection volumes are critical for quantitative studies. The minimal microinjection volume was determined for the organoid-optimized needle design by injecting single droplets of aqueous FITC conjugated dextran into oil (Fig. 6E). The accuracy of five different microinjection needles was tested by imaging injection droplets, measuring the cross-sectional area of single injection droplets using CVis, and calculating the spherical volumes of each droplet (Fig. 6E). Optimized microinjection needles were capable of reproducibly delivering  $0.2 \text{ nl} \pm 1.4\%$  of cargo. Each  $0.2 \text{ nl}$  droplet is approximately half the theoretical lumen volume of a  $100 \mu\text{m}$  wide organoid. Injection duration is a property of pneumatic injection systems that changes injection volumes. Though injection duration necessary to produce a  $0.2 \text{ nl}$  droplet varied from  $24 \text{ ms}$  to  $51 \text{ ms}$  between five different needles, there was little variability in droplet volume ( $<1\%$ ). This indicates that variation in needle tip geometry requires fine-tuning of injection durations to produce extremely small volumes. In contrast, longer injection durations of  $200 \text{ ms}$  produced consistent  $2.0 \text{ nl}$  droplets from five different needles with minimal variation ( $\pm 2.1\%$ ) (Fig. 6F). These data demonstrate that highly consistent volume droplets can be generated between  $0.2 \text{ nl}$  and  $2.0 \text{ nl}$  when modulating the injection duration.

When diagonal needle approaches are used for microinjection the needle tip can be observed in the focal plane of the target. When using a vertical needle approach the needle is not visible in the focal plane of the organoid until the puncture. The  $90^\circ$  articulation of the microinjection needle required a modified workflow to efficiently microinject organoids (Fig. 6G). Visual cues caused by light refraction off of the needle

tip enables alignment above the organoid (Fig. 6G.1); the needle tip is then advanced until it touches the top surface of the organoid (Fig. 6G.2). As the needle contacts the organoid exterior, deflection and bending of the epithelial monolayer are visualized as creasing and stretching of the organoid perimeter (Fig. 6G.3). Once punctured, the organoid retracts to its original diameter and cargo is delivered by pneumatic pulse (Fig. 6G.4). After needle retraction, creases in the organoid monolayer are no longer observed (Fig. 6G.5). If cargo is fluorescent, imaging can then be performed (Fig. 6G.6) (Supplemental Video 1).

Based on the diameter of the needle tip (1  $\mu\text{m}$ ), we estimate that a  $\sim 5\text{-}10\ \mu\text{m}$  hole (about 1 cell thickness) is generated as a result of the puncture through the epithelium. To evaluate whether cargo remained in the organoid lumen after needle withdrawal, luminal retention of an inert 70kDA fluorescein-dextran impermeable to the membranes and intercellular junctions was assessed<sup>138</sup>. Immediately after injection, the fluorescent dextran quickly diffused and equilibrated throughout the luminal space (Fig. 7A). Over time, signal intensity decreased as the organoid grew and expanded (Fig. 7B; Supplemental Video 2). While the decrease in fluorescent cargo might be due to leakage, it was hypothesized that reduction in fluorescent signal was due to increased luminal volume, effectively diluting the fluorescent cargo with organoid growth. To test this, CVis measured the mean intensity and area of the fluorescent signal every 30 minutes for 18 hours (Fig. 7C). While the mean intensity decreased to approximately half of the original intensity during the 18-hour time course, the signal area doubled (Fig. 7D,E). When the signal intensity was integrated over the observed area, the normalized signal was demonstrated to remain constant over the 18-hours (Fig. 7F). These data

indicate that the injected cargo was effectively retained in the organoids and suggests there is unappreciable leakage from the needle puncture.

### **Automated computer vision facilitates high-throughput organoid identification, injection and quantification of injected cargos**

Major limitations to efficient and high-throughput microinjection are manual identification of organoids suitable for injection, and the manual tracking and quantification of cargos post-injection. To address these problems a CVis program was developed to automatically identify suitable organoids cultured on a Cell Raft Array (CRA). CRAs are commercially available microculture well arrays that enable efficient imaging, identification, and position recall of thousands of organoids in a small footprint (Fig. 7G)<sup>106</sup>. There are ~15,000 microwells in a 2.0cm<sup>2</sup> area of the microfabricated device. Passaged organoids were randomly seeded using a Poisson distribution such that there was approximately 1 organoid per 200µm<sup>2</sup> microwell (Fig. 7G). Organoids were cultured for 3 days to achieve a population of organoids that were of a practical size for injection. The CRA was imaged in brightfield and fluorescence channels using MATLAB scripts, which serially collected indexed images of individual rafts. Images of each raft were then processed through OrganoidMorph, a custom computational image analysis pipeline developed in the open-source platform CellProfiler with a simple user interface<sup>135,139</sup>. Total organoid area and luminal area was measured using CVis, and monolayer width was determined by subtracting the overlapping area (Fig. 7H; Supplemental Video 3). Organoid area and monolayer width metrics for each organoid was associated with a specific address on the CRA to enable automated recall for microinjection. To validate OrganoidMorph identification, CVis-identified organoids were

compared to manually-identified organoids (Fig. 7I). Automated organoid identification in ~15,000 CRA wells took about 2 hours and was >95% accurate. Lumen segmentation was 96.8% accurate based on comparison to manual measurements (Fig. 7H,I). These data demonstrate that a CVis pipeline can be used to accurately and efficiently identify the location of hundreds of organoids, and quantify their morphology to identify sub-sets of organoids suitable for injection.

Anecdotally, microinjection efficiency is highly variable between organoids of different sizes, shapes, luminal volumes, and monolayer widths. Average monolayer widths and cross-sectional areas from ~1,800 organoids from CAG:DsRed mice were automatically determined by OrganoidMorph CVis analysis and the data was binned according to width and area (Fig. 7J, K). To test whether distinct morphologies were more suitable for microinjection, ~500 organoids with different monolayer widths and cross-sectional areas were targeted for microinjection with 0.4 nl of membrane impermeable 70kDA Fluorescein-Dextran (Fig. 7L). Microinjection was scored as 'successful' if FITC signal was entirely contained within DsRed-positive cell boundaries immediately after injection, or 'unsuccessful' if FITC signal was detectable outside of organoid boundaries (Fig. 7L). Organoid cross-sectional area, which is a proxy for luminal volume, was positively correlated with successful microinjection and injection efficiency (microinjection time vs area) (Fig. 7M). The smallest organoid successfully injected measured 10,000  $\mu\text{m}^2$ . In general organoids with cross-sectional areas of <10,000  $\mu\text{m}^2$  were not suitable for microinjection. Approximately, 50% of organoids with cross-sectional areas between 10,000  $\mu\text{m}^2$  and ~18,000  $\mu\text{m}^2$  were successfully injected; 100% of organoids with >18,000  $\mu\text{m}^2$  cross-sectional areas were successfully injected.

In contrast, there was no significant correlation between microinjection success and monolayer width (Fig. 7N). However, there was a positive correlation between injection speed and monolayer width for organoids with monolayers wider than  $\sim 15 \mu\text{m}$ . When organoid monolayers were  $>15 \mu\text{m}$ , each injection took an average of  $39.1 \pm 12.5$  seconds, while monolayers  $<15 \mu\text{m}^2$  took an average of  $82.2 \pm 14.4$  seconds to inject (Fig. 7O). These data provide important organoid morphology metrics and guidelines to increase efficiency and success of organoid microinjection.

### **Growth dynamics of transplanted microbial communities and colonoid barrier integrity can be monitored by computer vision**

A number of studies have piloted monoculture of bacteria in the lumen of organoids<sup>138,140–144</sup>. We sought to explore whether our high-throughput microinjection system could be used to culture microbial communities in the lumen of colonoids, which are organoids derived from colonic epithelium, and whether CVIs could be used to monitor growth dynamics of fluorescently labeled bacteria within a community. An inoculum of  $\sim 1,500$  non-pathogenic *E. coli* NC101 constitutively expressing GFP was injected into five individual colonoids to assess whether the fluorescent signature could be detected by microscopy. Confocal microscopy demonstrated that the GFP expressing *E. coli* NC101 could be easily detected (Fig. 8A). Orthogonal views of image projections invariably demonstrated a large *E. coli* NC101-GFP signal in close proximity to the colonoid monolayer (Fig. 8A; Video: S4). A mock community of two different traceable bacterial species, *E. coli* expressing DsRed, and *Y. pseudotuberculosis* expressing GFP, was injected into colonoids, detected by fluorescence microscopy, and monitored over time to determine whether growth dynamics of each species could be

quantified by CVis. Comparable to *E. coli* NC101-*GFP* alone, *E. coli* K12-*DsRed* and *Y. pseudotuberculosis-GFP* could be readily imaged together in the same organoid by epifluorescence microscopy at 2, 12 and 24 hours post-injection (Fig. 8C). There were no appreciable changes observed in epithelial thickness, budding, or growth rate after organoid lumen colonization.

Contamination of culture media due to off-target injection, needle leakage, or minor leakage out of the colonoid lumen would compromise colonoid cultures and complicate analysis of injected microbial communities. To address this issue, two different antibiotics, tetracycline and chloramphenicol, were added to the colonoid media to inhibit growth of free bacteria outside of the organoid lumen. *E. coli* K12-DsRED was resistant to tetracycline and *Y. pseudotuberculosis-GFP* was resistant to chloramphenicol. To test the efficacy and specificity of antibiotics added to the media, an inoculum of ~1,500 of each fluorescent strain was injected into 10 colonoids per antibiotic condition, 5  $\mu$ l of media was collected over time, cultured for 24 hours, then cultures were qualitatively assessed for bacterial growth and fluorescent signature. While there was no apparent bacterial contamination observed visually in the colonoid culture media at any time point, small amounts of active tetracycline-resistant and chloramphenicol-resistant microbes could be cultured from all conditions 2 hours after the injections (Fig. 8D). Neither strain could be cultured from media collected at 24 hour or 48-hour time points when both tetracycline and chloramphenicol were employed, indicating the antibiotics were effectively controlling contaminating bacteria outside of the colonoid lumen.

To determine if the growth of the mock community could be quantitatively monitored over time, 40 colonoids were injected with ~1500 *E. coli* K12-DsRED and ~1500 *Y. pseudotuberculosis*-GFP bacteria, and fluorescence signal was quantified by time-lapse CVis every 30 minutes (Fig. 8B). The integrated DsRED and GFP intensity within the colonoid lumen steadily increased over the 24-hour time course (Fig. 8E), suggesting both strains of bacteria in the community were growing. Although colonoids were exposed to antibiotics in the media, the data demonstrate only a modest decrease in fluorescence. A powerful feature of the CRA platform is that the contents of each raft can be individually retrieved for downstream analyses<sup>106</sup>. To determine whether bacteria were active and growing within the colonoid lumen, each colonoid injected with the mock community was retrieved from the CRA, and the number of live bacteria was quantified by colony formation assays (Fig. 8F). No significant difference was observed in the number of bacteria cultured from the luminal contents of colonoids retrieved 2 hours following injection, suggesting that the majority of the microbial load was retained in the colonoid lumen (data not shown). Twenty-four hours post-injection of the mock community, significantly more bacterium were retrieved from all colonoids indicating growth within the colonoid lumen (Fig. 8F). These findings demonstrate that growth dynamics of different bacterial species within a community can be monitored in the colonoid lumen by fluorescent signature and colony forming assays.

We next wanted to determine whether the signal level of fluorescent proteins expressed by bacteria could be directly correlated to the microbial load. Forty-eight colonoids were transplanted with 24ms, 48ms, 72ms, or 96ms injections consisting of ~800, ~1350, ~1700, or ~2000 K12-DsRED bacteria, ~200, ~300, ~500, or ~700

NC101-EGFP bacteria, and 70kDa dextran as an internal reference to monitor barrier function. Forty-five of the 48 attempted injections were successful (93.75%). Signal from both *E. coli* strains as well as the inert dextran could be observed immediately following microinjection and throughout the 24-hour incubation time. There was no apparent loss of barrier function as determined by a consistent signal from fluorescent dextran (Fig. 8G). The transplanted bacteria demonstrated increased growth as measured by CFU over the 24-hour period, and the fluorescent signal from each strain also showed a steady increase in the integrated DsRED and GFP intensity regardless of starting load (Fig 3H). As predicted from the visual observations, the integrated signal produced by the inert dextran remained steady during the 24-hour time course indicating that epithelial barrier function was preserved (Fig. 8I). The ratio of CFU to intensity demonstrated a non-linear relationship indicating that integrated fluorescence signals cannot be used to directly measure luminal microbial loads, but can serve as a proxy for growth (Fig 3. J,K).

### **The colonoid lumen supports the growth of aerobic and obligately anaerobic human microbiota taxa**

Investigating interactions of native microbial communities with the host epithelium in culture is technically challenging and many times impossible because native enteric microbial communities are dominated by obligate anaerobic species, which are difficult or impossible to cultivate *in vitro*<sup>127</sup>. Because of the relatively small colonoid lumen volume, which is surrounded by oxygen metabolizing epithelium, it was hypothesized that the colonoid lumen might be sufficiently hypoxic to cultivate the complex anaerobic microbial communities found in the human gut. Direct measurement of luminal oxygen

in very large human organoids derived from induced pluripotent stem cells has been performed using an oxygen microprobe<sup>145</sup>, however, these microprobe tips are far too large to directly measure oxygen in most organoids derived from primary tissues. Therefore, a computational model was developed to estimate the oxygen concentration using dimensions of a representative colonoid (Fig. 9A). Monolayer thickness and luminal volume was modeled based on this colonoid, and empirically-determined oxygen diffusion and oxygen consumption rates were applied to the model<sup>146</sup> (Fig. 9A). COMSOL Multiphysics modeling suggested that the lumen of colonoids has an estimated 10% of atmospheric O<sub>2</sub> (~180 nM) reaching the apical surface of the organoid due to respiration by the enclosing epithelial monolayer (Fig. 9A,B). The model is remarkably consistent with oxygen levels measured in hiPS-derived organoids where luminal oxygen was measured at ~8% and media levels at 18%<sup>145</sup>.

While complex communities of human GI microbes can be easily acquired by stool sampling from donors, unprocessed stool samples contain large particles that can clog microinjection needles. We developed and validated a method for processing stool samples such that they could be loaded into microinjection needles without clogging the small needle aperture or causing appreciable loss of community diversity (Fig. 9C). While centrifugation of stool diluted in saline is a conventional method to prepare fecal samples for transplantation into gnotobiotic animal models, it was not sufficient to remove enough of the large material that causes needle clogging. Two different commercially available filters were used to filter stool samples diluted in PBS, and the flow-through was compared to untreated samples and centrifuged samples by 16S amplicon sequencing. The results demonstrate little difference in observed species

between untreated, centrifuged, and filter #1, while there was an appreciable decrease in observable species when filter #2 was used. Similar trends were seen by principal component analysis (PCA) of the Operational Taxonomic Units (OTUs) where filter #1 samples closely clustered with OTUs in untreated samples (Fig. 9D). No needle clogging was observed when using stool flow-through from filter #1, which was used to process all stool samples prior to microinjection.

To determine whether aerobic and anaerobic communities could be transferred and cultivated within the colonoid lumen, a simple workflow was developed that enabled anaerobically collected stool samples to be efficiently injected into colonoids similar to the high throughput applications described above. Essentially, stool samples are filtered and loaded into the microinjection needles in an anaerobic chamber, followed by microinjection of a 0.2nl inoculum into the lumen of colonoids (Fig. 9E). This workflow was used to evaluate the compatibility of the colonoid lumen with fecal derived microbial communities (Fig. 10).

Fecal transplants were performed by injecting ~0.2 nl of the filtered stool sample into 30 murine colonoids. At each specified time point, 5 of the colonoids were collected and mechanically disrupted under anaerobic conditions to release bacteria into a solution, which was applied to broth plates for CFU assays (Fig. 10A). There was no apparent effect of colonization on colonoid viability throughout the timecourse. After fecal transplantation, increasing numbers of colonies were observed over time on plates incubated in both aerobic and anaerobic conditions (Fig. 10B). Few or no colonies were recovered from off-target injections, indicating that growth was specific to the lumen environment (Fig. 10C). To assess whether the colonoid lumen could support stable

fecal communities over time, the remaining 5 colonoids from each time point were subjected to 16S amplicon sequencing to monitor taxonomic changes (Fig. 10D). While the Firmicutes represented the most abundant phylum in the stool samples and colonoids at each timepoint, there was a notable expansion of the relative abundance in Actinobacteria and Proteobacteria phyla in the colonoids. Compared to stool, microbial communities injected into colonoids and cultured over time demonstrated no significant difference in the number of observed species or Shannon index, which is a quantitative metric to describe the numbers and dominance of a species within a community (Fig. 10E,F). Together these data demonstrate that complex bacterial communities isolated from donor fecal samples can be efficiently microinjected into the colonoid lumen and cultivated over a 4-day period with little change in the relative composition of the communities.

Obligate anaerobes can be subclassified as 'sporulating anaerobes', which exhibit some oxygen tolerance, or 'non-sporulating anaerobes', which are highly intolerant to oxygen<sup>146</sup>. The diarrheal pathogen *Clostridium difficile*, produces highly resistant spores that can be transmitted through an oxygen rich environment to colonize a new host<sup>127</sup>. *C. difficile* has been injected into organoids derived from hiPSc to study the impact of *C. difficile* toxins on host epithelium<sup>134,147</sup>. We wanted to test whether non-sporulating and highly oxygen-intolerant species could survive and grow inside the colonoid lumen. Bifidobacterium is a Gram-positive genus often associated with anaerobic bacteria and was represented in the healthy fecal microbiota sample. When the fecal microbial community was microinjected into colonoids this genus increased in relative abundance suggesting it is growing in the colonoid lumen (Fig. 10G).

While 16S rRNA gene amplicon sequencing indicates the presence and relative abundance of bacterial taxa, it does not assess their viability. To validate whether non-sporulating obligately anaerobe species of the *Bifidobacterium* genera could survive and grow within the colonoid lumen, a monoculture of *Bifidobacterium adolescentis*, a highly oxygen-intolerant species that is an early colonizer of the infant gut<sup>62</sup>, was microinjected into colonoids (Fig. 10H). Survival and growth of *B. adolescentis* in the colonoid lumen was evaluated at 6, 12, 24, 48, or 60 hours following microinjection. Since *B. adolescentis* was not capable of growing on plates<sup>63</sup> activity was evaluated by culture capacity in anaerobic broth and growth was evaluated by copy-number qPCR for the *B. adolescentis* 16S rRNA gene, which can be used as a proxy for microbial load. While control injections exposed to oxygen were unable to grow in culture at the earliest time point tested (6 hours), *B. adolescentis* could be cultured in broth through 3 days of cultivation in the colonoid lumen (Fig. 10I). There was an ~4.5-fold increase in the relative abundance of *B. adolescentis* within the colonoid lumen between injection (t = 0) and 6 hours of cultivation (Fig. 10I). While *B. adolescentis* could survive through 3 days post-injection, there was a significant loss of 16S rRNA gene abundance at 2 days post-injection, suggesting factors required for growth had diminished. Together, these results indicate that the colonoid lumen is sufficiently hypoxic to support survival and growth of non-sporulating anaerobes found within the larger community of fecal microbiota.

## **Conclusions**

In response to the call for high-throughput platforms and physiologically relevant *in vitro* culture models to study 'unculturable' taxa<sup>148,149</sup> and their effect of GI physiology,

we developed and validated a semi-automated high-throughput microinjection device that enables highly efficient and reproducible injection of cargos into the lumen of gut organoids. The microinjection device was married to CVis algorithms and microculture arrays (CRAs) for high-content sampling of inert and biological cargos injected into the organoid lumen. The microinjection platform was used to monitor and quantify the growth dynamics of mock microbial communities harboring fluorescent reporter genes. With the knowledge that the organoid lumen was sufficiently hypoxic to support cultivation of more oxygen-tolerant sporulating anaerobes such as *C. difficile*<sup>138,140</sup>, we predicted that complex microbial communities containing highly oxygen-sensitive non-sporulating anaerobes might be able to be cultivated in the colonoid lumen. Indeed, computational models suggested a 10-fold decrease in oxygen concentration at the apical membrane of the organoid due to the oxygen-consumption rate of colon epithelial cells and known oxygen diffusion properties. New methods to prepare human fecal samples for microinjection were developed and validated to functionally test whether complex microbial communities would survive and persist in the colonoid lumen. Microinjection of fecal samples into the colonoid lumen demonstrated efficient fecal microbial transplantation based on similar relative abundance of taxa compared to the transplanted fecal sample. Additionally, the microbial communities persisted over a 4-day period with relatively little change in relative composition. As a benchmark for 'functional anoxia' of the colonoid lumen we mono-transplanted *B. adolescentis*, a highly oxygen-sensitive anaerobe, into the colonoid lumen and demonstrated growth and survival over a 4-day period. Together these findings strongly support the concept that

the environment of organoid lumen can serve as a suitable model to investigate many aspects of human fecal microbial communities.

Aside from the utility of this platform for study of the microbiome, our findings indicate that robust retention of cargos injected into the organoid lumen that will be useful for screening compounds and toxins that impair epithelial barrier function. Our high-content CVis applications demonstrate the ability to monitor retention of membrane impermeable compounds in hundreds or thousands of organoids using time-lapse imaging. A pioneering study using hiPSC-derived organoids to study barrier function demonstrated that *C. difficile* toxins disrupted the epithelial barrier resulting in a loss of fluorescent membrane impermeable probe<sup>134</sup>. While these studies and our findings indicate that retention of membrane impermeable probes are useful for measuring epithelial membrane integrity, our results indicate that the fluorescent signal should be normalized to the organoid growth volume to account for loss of signal that could be misinterpreted as a leaky epithelial barrier.

Organoids are not all created equal. Studies at the single organoid level demonstrate large variations in cell lineage composition, gene expression, and function of transporters<sup>107,150</sup>. In a previous study we isolated 96 organoids at different stages of ontogeny and demonstrated that while there was a stereotypical pattern of lineage gene expression at early organoid development, mature organoids exhibited highly variable gene expression consistent with heterogeneous ratios of cell lineages within the organoid<sup>114</sup>. Functional heterogeneity in organoids has also been shown in high-throughput analysis of single organoids using a swelling assay, which is commonly used to assess function of the Cystic Fibrosis Transmembrane Conductance Receptor<sup>150,151</sup>.

Interestingly, at the single organoid level, two categories of organoids were observed; responders to forskolin-induced swelling, and non-responders. And even within each of these populations substantial variation in swelling dynamics was documented. These findings highlight the importance of designing organoid experiments with sufficient biological and technical replicates to provide adequate statistical power. Our microinjection and CVis platform currently enables microinjection of ~90 organoids per hour with subsequent automated time-lapse monitoring of injected cargos. Since the organoids are injected in a physiologic chamber, data can be collected continuously over several days, or the CRAs can be returned to the conventional incubator and data can be sampled by returning the CRA to the automated stage for data sampling at specified time points. While this throughput is likely adequate for most experiments, the data indicate that optimum throughput can be achieved by culturing organoids to a point that the cross-sectional area is  $>18,000\mu\text{m}$ . Further optimization of automated needle positioning in the center of the organoid, and z-plane articulation during the puncture sequence are predicted to substantially increase microinjection throughput.

The ability to efficiently and reproducibly introduce a variety of cargos into the organoid lumen is a significant methodological advance that will be useful to investigate a broad range of topics related to luminal-epithelial physiology, such as barrier function, nutrient absorption, drug transport and metabolism, and the impact of dietary compounds or pharmaceuticals on stem cell maintenance and differentiation. While this study focused on analysis of bacterial communities, our system could be easily adapted to studies focused on the fungi, parasites, and viruses that impact human GI health.

## **Methods**

### **Automated Imaging System**

Microinjection hardware was fitted within a Precision Plastics (USA) enclosure mounted on an Olympus IX81 (Japan) inverted microscope outfitted with a ProScan (Prior, UK) automated stage and controller. Images were acquired by an ORCA-03G (Hamamatsu, Japan) high-speed camera at parameters controlled through a HF204 or HF202 (Prior, UK) automated shutters and a HF108IX3 (Prior, UK) filter wheel. The system was controlled using custom image acquisition software (MathWorks, USA) and MicroManager (Vale Lab, UCSF)<sup>152</sup>.

### **Microinjection Hardware Custom Fittings**

Custom adaptors were 3D-printed to house a commercially available MM-89 (Narashigi, Japan) motor-drive manipulator within the confines of a microscope mounted atmospheric regulating chamber. The physiologic chamber was necessary to preserve biological function of organoids during injection, high throughput, and time-lapse imaging. A spacer was 3D-printed to increase the clearance between the rear wall of the chamber and the NO-PIX-3 (Narashigi, Japan) manipulator mounting bar. Pilot studies showed that pneumatically-driven microinjectors were best suited to remotely deliver nanoliter cargo loads within the chamber constraints. The Pico-spritzer III (Parker-Hannifan, USA) was suitable for use within the IX81 chamber with a low rate of valve malfunction occurrences, which can lead to pressure buildup and needle rupturing. A custom control arm was 3D-printed to orient the injection needle holder perpendicular to the MM-89 shaft collar and parallel to the stage, facilitating vertical needle articulation. A stage insert with a compression fitting was 3D-printed to hold

CellRaft™ Array (CRA) devices tightly and reduce stage position error when devices are moved in and out of the microinjection platform<sup>152</sup>. All CAD files for 3D-printed fittings are available in the online supplementary materials.

### **Optimized Microinjection Needle Processing**

To generate microinjection needles tailored to organoid microinjection, 1 mm filament capillaries (World Precision Instruments, USA) were pulled to fine point using a P-2000 (Sutter, USA) laser-based micropipette puller at parameters modified from the standard “bee-stinger” needle production protocol to reduce the diameter of the needle point<sup>137</sup>. A 90° bend was formed in the needle body ~1.5 cm from the needle tip by heating the needle body with an open flame while horizontally suspended, allowing the bend to form by gravity. The needle pulling process produced microscopic defects that impaired efficient organoid microinjection. To remove the defects, the needle aperture was polished through 6 minutes of wet-etching in 5% hydrogen fluoride (HF). The needle tip was subsequently submerged in sodium bicarbonate to neutralize HF coating the needle tip. To prevent HF and sodium bicarbonate from traveling up the internal filament into the needle body and contaminating cargos, compressed air was fed into the needle body as the tip was submerged in all solutions.

### **Colonoid culture and expansion**

Crypts were isolated from the colon of adult (10-16 week old) Wild type (WT) or CAG:DsRED (constitutively DsRED expressing) male mice reared on Bed-o'-cobs (Anderson's Lab Bedding, USA) and fed a soy free, grain based diet (Envigo, USA) as described<sup>38</sup>. In brief, the whole colon was resected, flushed with cold PBS, opened longitudinally, and then treated with 'isolation buffer'<sup>130</sup>. After 90-minutes, whole crypts

were released from the tissue by gentle shaking then collected by centrifugation at 1000 x g. Crypts were embedded in laminin rich Cultrex hydrogel (Corning, USA) at ~4 crypts/ $\mu$ L. Colonoids were expanded in 50% L-WNR media and 50% 'LCM' media produced according established protocols with the minor modification of removing antibiotics during the conditioning phase to prevent carryover into organoid cultures<sup>153</sup>. In these studies, we utilized media shown to produce colonoids containing all of the native differentiated lineages<sup>153</sup>. For passaging, colonoids were dissociated into small cell aggregates by digesting in TrypLE (Gibco, USA) supplemented with 10  $\mu$ M Y-27632 (Selleck, USA) for 4-6 minutes. Cold serum (10% v/v) was added to the dissociated cells to quench enzymatic activity. For injection experiments, large aggregates were excluded prior to culture by passing dissociated colonoids through a 40 $\mu$ m filter. Organoids were grown for 72hr before injections were performed and sampled by 168hrs to prevent overgrowth that could compromise luminal integrity. Aggregate concentration was visually quantified (fragments/volume) by microscopy. All protocols for animal use were reviewed and approved by the University of North Carolina Institutional Animal Care and Use Committee.

### **Plating Colonoids on CRA devices**

Colonoid fragments were added to CRA reservoirs at 1.5 fragments per raft in L-WNR culture media and centrifuged at 51 x g for 5 min at 4°C to deposit fragments on the rafts. Following centrifugation, the culture media was gently aspirated so not to disrupt fragments, and 150 $\mu$ L of Cultrex (Trevigen, USA) was added per cm<sup>2</sup> of array surface. A second centrifugation for 5 min at 51 x g was used to ensure hydrogel embedded fragments were deposited at the bottom of the raft. The hydrogel was

allowed to polymerize at 37°C for 30 min before 200 µl of L-WNR culture media supplemented with 10 µM Y-27632 was added per cm<sup>2</sup> of array surface. Media was exchanged every 72-hours<sup>154</sup>. Y-27632 was only included in the media at initial plating. Colonoids were grown until they occupied ~80% of each raft (typically 72-hours after plating) prior to injection assays.

### **Computer Vision Identification of Organoids**

Organoids were cultured on CRAs (Cell Microsystems, USA), which are microculture devices that contain ~15,000 wells in a 2.0 cm<sup>2</sup> footprint<sup>114,155</sup>. Organoids were passaged and dissociated to small fragments, which were plated on CRAs such that there was a density of ~1 organoid/well. When organoids had grown to a point they exhibited a defined luminal space (~3 days), the entire CRA was tile-imaged using a MATLAB automated imaging script, which operated the MMCore API component of the open-source MicroManager (Vale Lab, UCSF) automated microscope controller<sup>152</sup>. Autofocus was used to correct for variations in the flatness of the CRAs. To determine whether an organoid suitable for injection was contained on a raft, individual images of each raft were evaluated by a novel CVis algorithm, OrganoidMorph (see supplemental files). The OrganoidMorph image analysis pipeline was developed in the open-source computational image analysis platform CellProfiler<sup>139</sup>. OrganoidMorph identifies the contents in each raft using a Gaussian mixture model that identifies positive from negative pixels<sup>156</sup>. This creates a binary image mask of the fluorescent signal. The size and shape of the mask is then filtered using threshold cut-offs that are consistent with organoid morphology (schematized in Fig. 7H). The location of organoids that passed the OrganoidMorph filtering algorithm was automatically logged so that it could be easily

returned to for microinjection. The luminal compartment was identified by inverting the signal within the colonoid area and segmenting by Otsu thresholding (Supplemental Software: OrganoidMorph.cpproj).

### **Computer Vision Quantification of Injected Cargos**

To identify the fluorescent cargos that were microinjected into the organoid lumen, images were analyzed by CVis (Supplemental Software: OrganoidCargo.cpproj). Specifically, the fluorescent signal area of each image was identified by Otsu thresholding, which is a computational method that decides positive and negative pixels<sup>157</sup>. Masks were generated from the positive fluorescent signal and the area and mean pixel intensity within the mask was measured. These values (intensity x area) were normalized to  $t = \text{initial values}$  for each organoid, and integrated (mean intensity x area) to account for volumetric changes.

### **Assessing Efficiency of Microinjection Device**

Efficiency of the platform was assessed by targeting dsRED colonoids of various size and morphology for microinjection with 0.4nL  $\pm 0.8\%$  of 70kDA fluorescein conjugated dextran (Thermofisher, USA). Colonoids were grown for 72-hours on a CRA device and identified using the OrganoidMorph pipeline. 500 identified colonoids were randomly targeted and microinjection was attempted with the duration of each attempt recorded. microinjection success was assessed by fluorescent microscopy and recorded immediately following each attempt. Microinjection success and duration was related to colonoid size and monolayer width post-hoc based on the CRA address of colonoids targeted for microinjection.

## Retrieving Bacteria from the Organoid Lumen

Live microbes were retrieved from the colonoid lumen by passing intact organoids through a 30-gauge needle (BD biosciences, USA), disrupting the surrounding monolayer. Whole colonoids were retrieved from culture platforms by pipetting and suspended in sterile DPBS (Gibco, USA) before loading into a standard syringe (BD biosciences, USA). Organoids transplanted with anaerobic species were suspended in anoxic DPBS intact and transferred into an anaerobic chamber (COY, USA) prior to passage through a 30-gauge needle.

## Bacterial Cultivation

Aerobic bacteria strains Aerobic bacteria strains (*Escherichia coli* NC101 and *Yersinia pseudotuberculosis* YPIII) were cultivated in Luria broth shaken at 240 rpm or on broth agar plates. *E. coli* NC101 transformed with pEGFP was grown at 37°C in medium containing 10mg/ml carbenicillin. *E. coli* NC101 transformed with pRZT3 was grown at 37°C in medium containing 10mg/ml tetracycline. *Y. pseudotuberculosis* YPIII containing the PfrdA::gfp vector was grown at 30°C on media supplemented with 20% tryptone and 10mg/mL chloramphenicol. *Bifidobacterium adolescentis* was isolated from the stool of a healthy patient (NCBI: BioProject ID PRJNA291486). The strain was maintained in anaerobic conditions until the time of injection<sup>46</sup>. *B. adolescentis* was grown from frozen glycerol stocks (-80°C) in oxygen depleted MRS broth supplemented with 0.2% cysteine overnight in an anaerobic chamber (5% CO<sub>2</sub>, 10% H<sub>2</sub>, 85% N<sub>2</sub>) at 37°C without agitation. Fecal microbiota communities were processed or retrieved from the organoid lumen in an anaerobic chamber, plated on MRS medium and incubated in

the anaerobic chamber (5% CO<sub>2</sub>, 10% H<sub>2</sub>, 85% N<sub>2</sub>) at 37°C, or were cultured aerobically at 37°C.

### **High Resolution Imaging of Microinjected Colonoids**

GFP expressing *E. coli* NC101 was grown to stationary phase (overnight) before ~1,500 CFUs were injected into 5 CAG:DsRED colonoids grown on 50mm tissue culture dishes. Colonoids were fixed 2 hours following injections with 4.0% paraformaldehyde before injected *E. coli* was observed within the colonoid lumen using an Olympus FV1000MPE upright confocal microscope. A 20X/1.00W immersion objective was used to collect 1024x1024 pixel Z-stacks at 2.0 μm intervals through each organoid with sequential detection of *E. coli* (GFP), colonoid epithelium (DsRED) and non-specific debris (DAPI) with Kalman averaging of 2-4X line scans. Detector and laser setting were adjusted to account for signal attenuation due to variable colonoid size and imaging depth. ImageJ was used to adjust brightness and contrast for optimal visualization<sup>158</sup>.

### **Mock Community Response to Media Antimicrobials**

WT colonoids were grown for 72 hours on a CRA device separated into 4 discrete media chambers. Chambers were treated with either chloramphenicol, tetracycline, both antibiotics, or no antibiotics. Broth monocultures of *E. coli* K12 expressing DsRED and *Y. pseudotuberculosis* expressing EGFP were grown to stationary phase (overnight for *E.coli*, 48 hours for *Y. pseudotuberculosis*). Equal volumes of stationary phase cultures were mixed, diluted in LB to 20%, and washed repeatedly in LB by centrifugation at 18,000 x g for 15 minutes to remove residual antibiotics. 20 μl of the mixed sample were loaded into injection needles and transferred

to the injection apparatus. Injection droplets were collected in sterile media and plated on selective LB agar plates to measure microbial cargo load before targeting colonoids greater than 100µm in diameter for microinjection. Following injections additional injection droplets were collected in sterile media and plated on LB agar plates to ensure similar microbial cargo loads were delivered during the injection process. 2-hours following injection, successfully injected organoids were retrieved from each condition and luminal contents were cultured to assess transplant efficiency. The remaining colonoids were fluorescently imaged at 30-minute intervals for 24 hours before retrieval and luminal contents were cultured to assess microbial growth. As controls for antibiotic activity, 10 µL samples of the organoid culture media from each condition collected 2 hours, 24 hours, and 48 hours following injections were collected and used to seed conventional broth cultures treated with tetracycline or chloramphenicol.

### **Relating Fluorescent Signal to Microbial Load**

Colonoids were injected with increasing loads of fluorescent inert and microbial cargos and imaged before sampling the luminal contents. WT colonoids were grown in the presence of tetracycline for 72 hours in conventional culture devices allowing larger colonoids to be cultivated. *E. coli* K12 expressing DsRED and *E. coli* NC101 expressing EGFP were grown to stationary phase (overnight) in LB containing tetracycline. Equal volumes of stationary phase cultures were mixed, diluted in LB to 20%, and washed repeatedly in LB by centrifugation at 18,000g for 15 minutes to remove residual antibiotics. The washed microbial sample was diluted to 50% in 70kDA Alexa Fluor 647 conjugated dextran (Thermofisher, USA). 20 µl of the mixed sample were loaded into injection needles and transferred to the injection apparatus before 12 organoids were

targeted for microinjection at 4 different durations (24ms, 48ms, 72ms, 96ms). All injected organoids were imaged before 6 organoids from each microinjection duration were collected and luminal contents were cultured to assess the delivered microbial load. The remaining colonoids were fluorescently imaged at 30-minute intervals for 24 hours before retrieval and luminal contents were cultured to assess microbial growth.

### **Stool Sample Preparation**

A stool sample (100  $\mu$ l) from a healthy human host (UNC IRB:15-2133) was homogenized in sterile, anoxic PBS (1.0 ml) inside the confines of an anaerobic chamber. The homogenized stool sample was then subject to differential centrifugation (5 minutes at 1000 x g), filtration through 5.0  $\mu$ m syringe filters (Millipore, filter #1), (GE, filter #2), or left unprocessed. Samples (100  $\mu$ l) were stored at -80°C until subjected to DNA isolation and 16S rRNA gene amplicon sequencing (see below).

### **Colonoid Fecal Microbiota Transplantation**

A homogenized healthy donor stool sample was processed using a 5.0  $\mu$ m Millipore syringe filter and loaded into injection needles in anaerobic conditions. Needles were immediately transferred to the injection apparatus and tested to verify reproducible cargo delivery prior to targeting a single colonoid in individual wells of a 96-well plate for injection. Colonoid injections that were off-target or showed observable leakage were used as controls, and wells with a single successful injection were sampled to assess microbial colonization by 16S rRNA gene amplicon sequencing and culturing. Colonoid injections were completed within an hour of removing needles from the anaerobic chamber. Retrieved fecal microbial communities were split by volume and cultured

anaerobically and aerobically on MRS broth agar plates to determine colonoid microbial load.

### **DNA Isolation**

DNA from stool samples was isolated using a DNeasy kit (Qiagen, USA) as directed. DNA from microbe-associated colonoids was subject to the Qiagen DNeasy kit protocol with an additional 5-minute bead-beating step at room temperature to facilitate separation of bacteria from colonoids and improve cell lysis. Isolated DNA was subject to spectrophotometric quantification via NanoDrop™ (Thermo Fisher), assessing both quantity (ABS260nm) and purity (260/280nm ratio).

### **16S rRNA Gene amplicon sequencing**

Total DNA (12.5 ng per sample) was amplified using primers consisting of the locus-specific sequences targeting the V3-V4 region of the bacterial 16S rRNA gene<sup>48</sup>. Primer sequences contained overhang adapters appended to the 5' end of each primer for compatibility with Illumina sequencing platform. Complete primer sequences:

(F) 5'-

TCGTCGGCAG:CGTCAGATGTGTATAAGAGACAGGTGCCAGCMGCCGCGGTAA-3'

(R) 5'-

GTCTCGTGGGCTCGGAGATGTGTATAAGAGACAGGGACTACHVGGGTWTCTAAT-3'.

PCR reaction mixes contained 12.5 ng of total DNA, 0.2 µM of each primer and 2x KAPA HiFi HotStart ReadyMix (KAPA Biosystems, USA). The thermal profile for the amplification of each sample had an initial denaturing step at 95°C for 3 minutes, followed by 28 cycles of denaturing of 95°C for 30 seconds, annealing at 62°C for 30

seconds and a 30 second extension at 72°C. Post cycling, a 5 minutes extension at 72°C was performed, and a final hold at 4°C. Each 16S rRNA gene amplicon was purified using the AMPure XP reagent (Beckman Coulter, USA). Illumina dual-index barcodes (index 1(i7) and index 2(i5)) (Illumina, USA) were added to each amplicon target using a limited cycle PCR program. The thermal profile for the amplification of each sample had an initial denaturing step at 95°C for 3 minutes, followed by a denaturing cycle of 95°C for 30 seconds, annealing at 55°C for 30 seconds and a 30 second extension at 72°C (8 cycles), a 5 minutes extension at 72°C and a final hold at 4°C. The final libraries were again purified using the AMPure XP reagent (Beckman Coulter), quantified via Quant-IT™ PicoGreen® dsDNA Assay Kit (Thermo Fisher) and normalized prior to pooling. The DNA library pool was then denatured with NaOH, diluted with hybridization buffer and heat denatured before loading on the MiSeq reagent cartridge (Illumina) and on the MiSeq instrument (Illumina). Automated cluster generation and paired-end sequencing with dual reads were performed according to the manufacturer's instructions.

### **Sequencing data analysis**

Multiplexed paired-end fastq files were produced from the sequencing results of the Illumina MiSeq using the Illumina software configureBclToFastq. The paired-end fastqs were joined into a single multiplexed, single-end fastq using the software tool fastq-join. Demultiplexing and quality filtering was performed on the joined results. Quality analysis reports were produced using the FastQC software. Bioinformatics analysis of bacterial 16S amplicon sequencing data was conducted using the Quantitative Insights Into Microbial Ecology (QIIME) software<sup>159</sup>. OTU picking was

performed on the quality-filtered results using `pick_de_novo_otus.py`. Chimeric sequences were detected and removed using ChimeraSlayer. Alpha diversity and beta diversity analysis were performed on the data set using the QIIME routines: `alpha_rarefaction.py` and `beta_diversity_through_plots.py`<sup>160,161</sup>. Summary reports of taxonomic assignment by sample and all categories were produced using QIIME `summarize_taxa_through_plots.py` and `summarize_otu_by_cat.py`.

### **Colonoid Anaerobe Monoculture Assay**

*B. adolescentis* cultured until the cells reached late-log growth (OD<sub>600 nm</sub> = ~0.6) before loading injection needles with 20 µl of culture inside an anaerobic chamber. Loaded needles were immediately transferred to the microinjection apparatus and tested to verify reproducible cargo delivery prior to targeting a single colonoid in individual wells of a 96-well plate for injection. Colonoid injections that were off target or showed observable leakage were used as controls while wells with a single successful injection were sampled over 60-hours and subjected to qPCR targeting the *B. adolescentis* 16S rRNA gene and cultured in MRS broth access *B. adolescentis* growth and validate activity organoids.

### **Statistics**

Normalcy of colonoid morphology was assessed by D'Agostino-Pearson and Shapiro-Wilk normality tests. Monolayer width and cross-sectional area of 1827 colonoids grown on 3 CRA devices and quantified by OrganoidMorph did not demonstrate a normal distribution by either test at an alpha level of 0.05. Colony counts from agar plates were compared by the Tukey-Kramer method with an alpha level of 0.05. Droplet volumes were compared between needles by Tukey-Kramer method at an

alpha level of 0.05. No statistical method was used to predetermine sample size and experiments were non-randomized. All analyses were performed using GraphPad Prism 7 ( GraphPad Software, USA).

## Figures

Limitation of Organoid Technology	Possible Solution(s)
Lack of cell types/ tissue layers normally interacting with the of stem cell niche.	Incorporate other cell types with organoid cultures for co-culture systems
Absence of microbial populations limit modelling of host-microbe interactions	Complement with organotypic culture systems with microbiota culture and characterization technologies.
Lack of <i>in vivo</i> growth factor/ signaling gradients in three-dimensional culture	Generate ligand concentration gradients using microfluidic technologies
Lack of biomechanical cues present in the intestinal environment	Vary physical attributes culture hydrogel such as composition, porosity and stiffness
Organoids are highly heterogeneous in viability, size, shape, and cellular composition impeding phenotype screens	Organoids can be tracked individually using microfabricated devices facilitating high throughput imaging
Organoids develop as enclosed spheres limiting access to the enclosed apical lumen	1) Spherical organoid monolayers can be opened into more planer monolayers exposing the apical membrane, enabling direct manipulations 2) Material can be specifically delivered to the enclosed organoid lumen using microinjection technologies

**Table 1: Factors limiting the use of organoid technologies.**

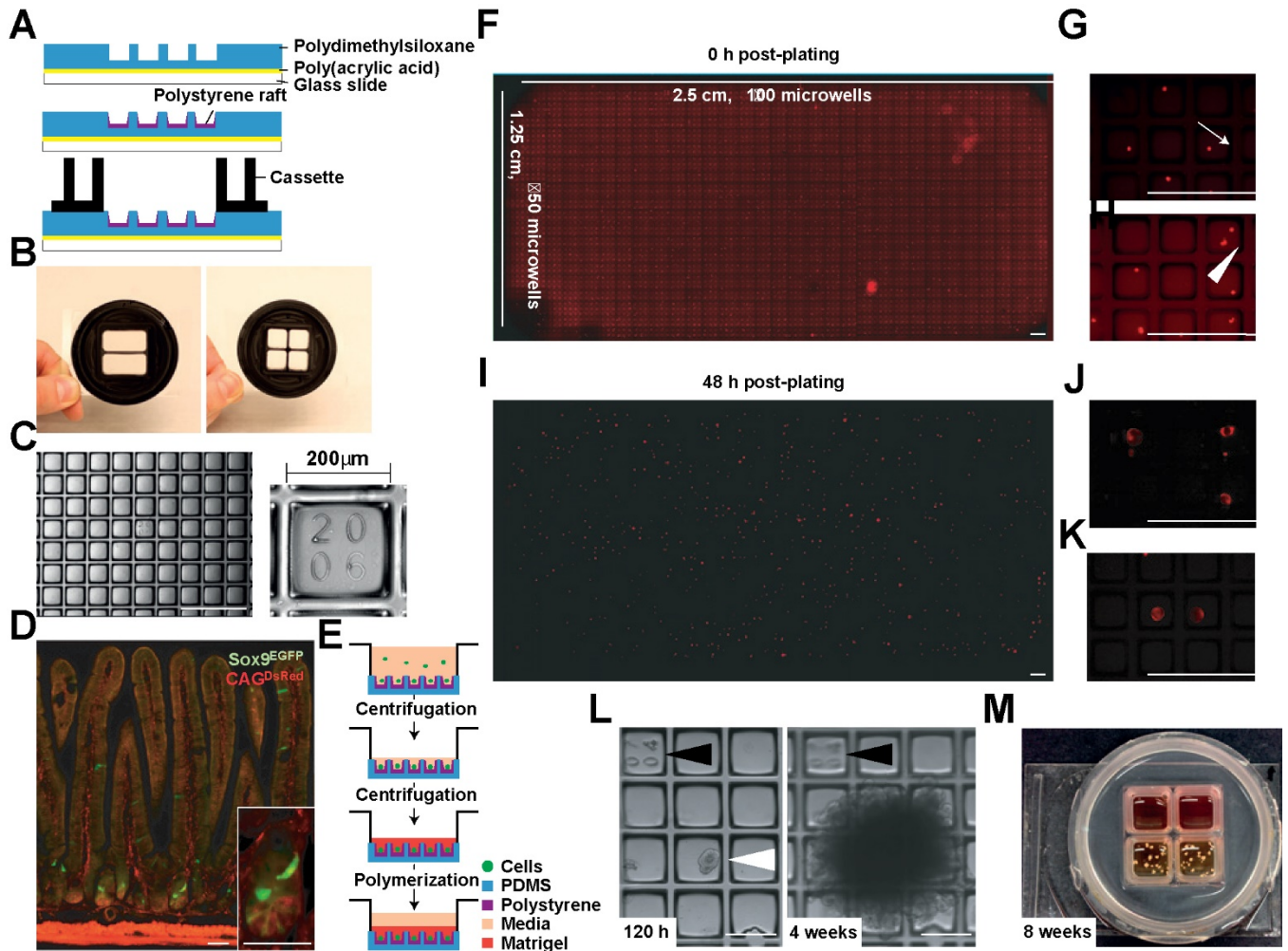


**Figure 1. Modified CRAs are compatible with long-term culture of primary IESCs.**

(A) CRAs consist of polystyrene ‘raft’-lined PDMS microwells mounted to a glass slide with a thin layer of PAA, and attached to a cassette containing media chambers. (B) Cassettes can be scaled to divide a single CRA into 2 or 4 separate media reservoirs. (C) Microwells are 200  $\mu\text{m}^2$ , arranged in a grid, with the physical addresses stamped into the PDMS at 5-well intervals. Scale bar represents 600  $\mu\text{m}$ . (D) IESCs are isolated from Sox9EGFP :CAGDsRed transgenic mice, which express DsRed throughout the intestinal epithelium. Scale bars represent 50  $\mu\text{m}$ . (E) Isolated cells are seeded into microwells through centrifugation in media, and then overlaid with Matrigel. (F-H) IESCs

are randomly distributed across arrays immediately after plating (F), with some microwells containing single IESCs (g, arrow), and others containing multiple IESCs (H, arrowhead). (I-K) Imaging of the same array at 48 hr reveals widespread organoid formation (i), with typical cystic growth of early structures (J,K). Scale bars for f–k represent 600  $\mu\text{m}$ . (l,m) Long-term culture experiments demonstrate that developed IESCs grow out from their original microwells over the course of 4 weeks (l; black arrowhead indicates well address corresponding with CRA position; white arrowhead indicates organoid at 120 hrs), and can be sustained in the array format for 8 weeks or longer (m; upper two wells are empty in this image). Scale bars represent 200  $\mu\text{m}$ .

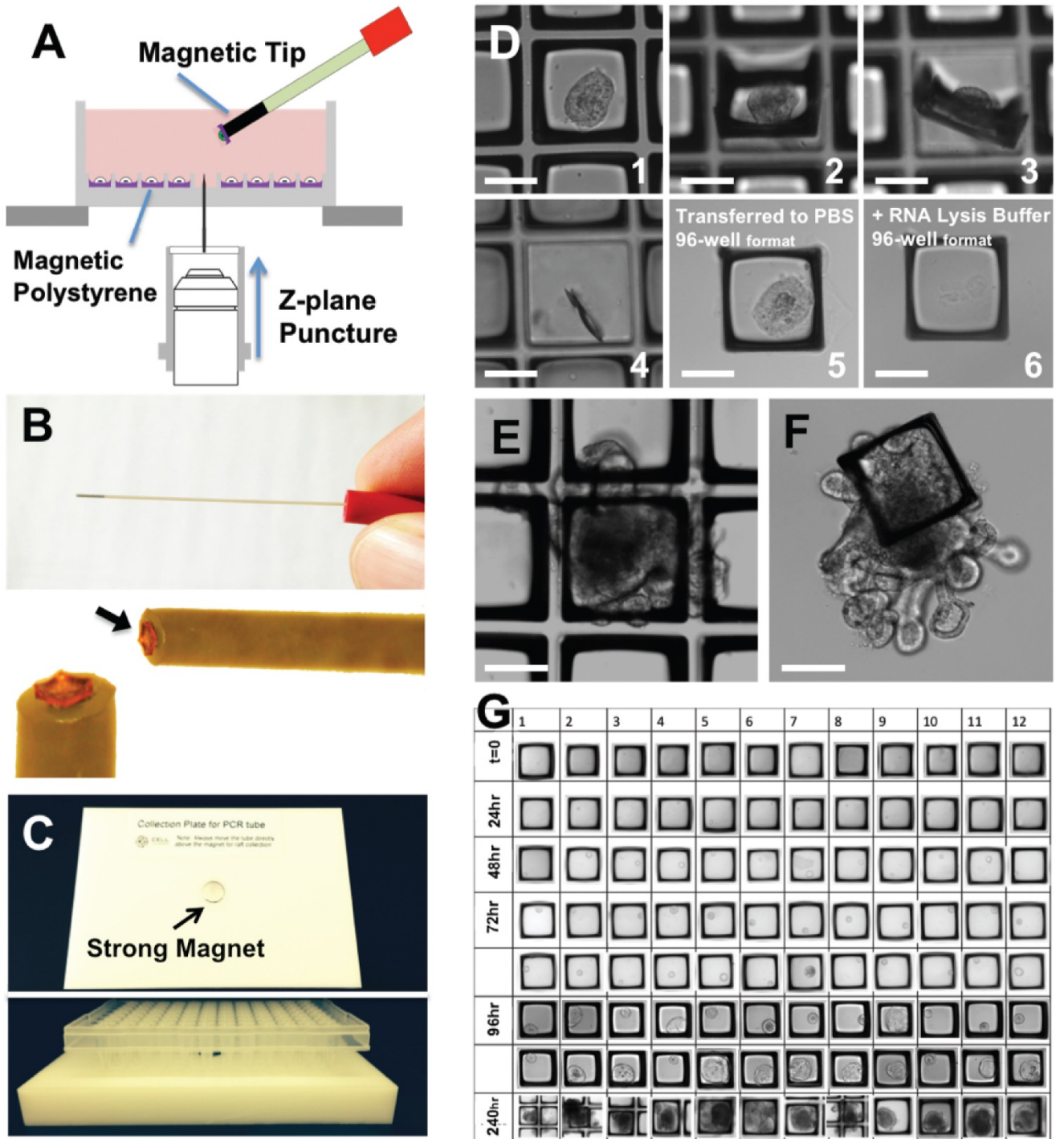


**Figure 2. Retrieval of magnetic rafts for downstream gene expression analysis.**

(A) Raft retrieval. A device containing a fine needle positioned in the center of a clear plexiglass window was fitted onto a 10X objective lens. Z-plane focus was used to puncture the bottom of the PDMS liberating the raft. A magnetic wand was used to

collect the magnetic raft. (B) The magnetic wand facilitates efficient retrieval of magnetic rafts (note red magnetic raft on tip of wand). (C) The raft is liberated from the magnetic wand when placed in a 96-well format dish that is positioned over a stronger magnet place on ice. (D) Time lapse image of raft retrieval (frame 1-4). The raft with organoid depicted in frame 1 was captured by magnetic wand and placed in PBS (frame 5). Enteroid was efficiently lysed in RNA lysis buffer prior to cDNA syndissertation (frame 6). (E) A large well-developed organoid was identified in the CRA and retrieved using the magnetic wand. (F) Matrigel anchors the large organoid to the magnetic raft for efficient capture. (G) Rafts and associated images can be ordered in a conventional 96-well format for indexing and retrospective analysis. Scale bars represent 100 $\mu$ m

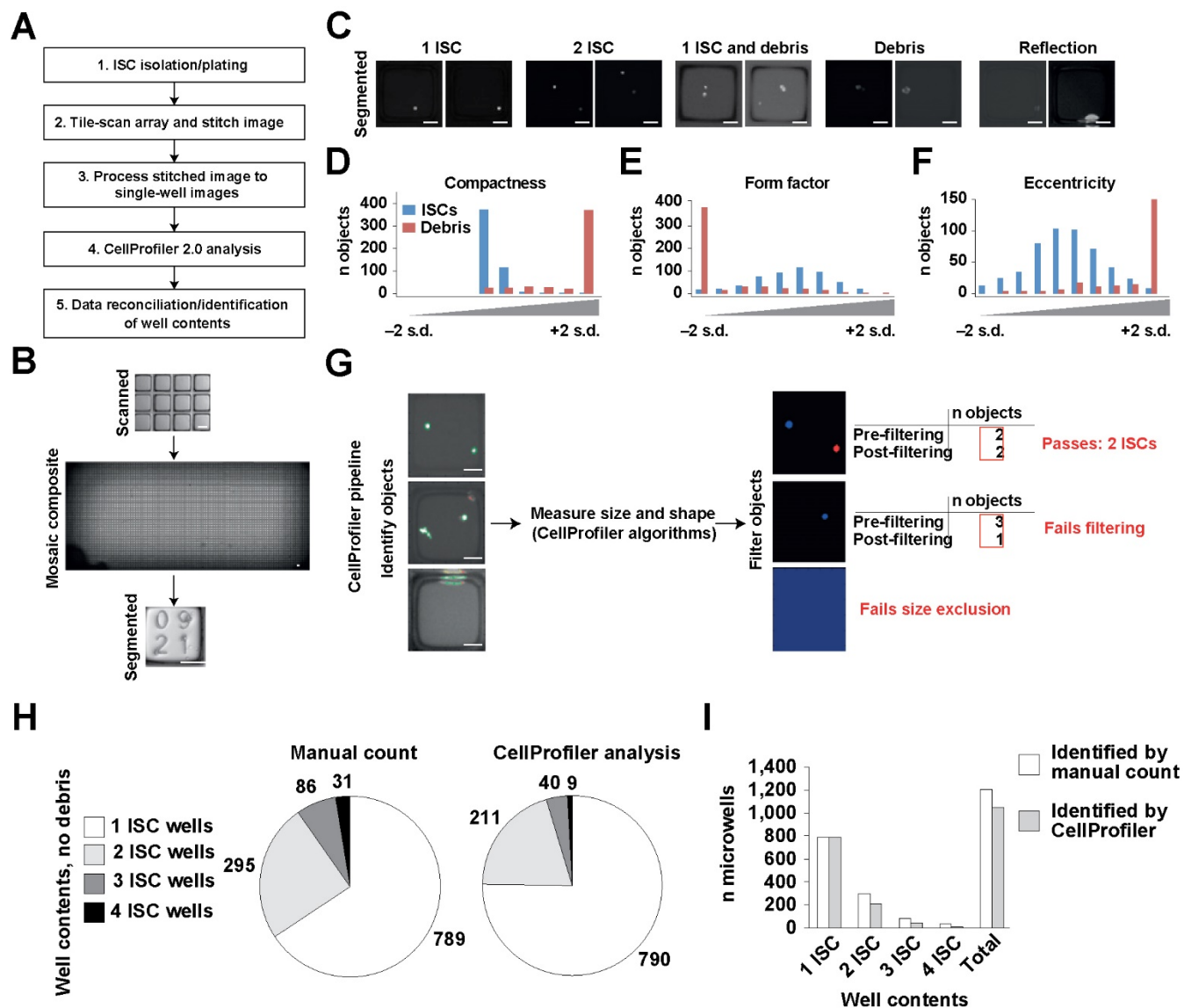


**Figure 3. Software-assisted post hoc analysis identifies initial well contents of CRA culture.**

(A) A defined workflow facilitates post hoc image analysis to identify well contents in CRA cultures. (B) Tile-scanned images are stitched together to form a single composite image, which is then segmented into individual microwell images, each with a unique address corresponding to its physical position in the array. Scale bars represent 100  $\mu\text{m}$ . (C) Visual examination of individual microwells reveals the presence of debris and fluorescent glare as well as IESCs. Scale bars represent 50  $\mu\text{m}$ . (D-F) To distinguish

between true IESCs and debris/noise, visually scored wells were analysed by CellProfiler to determine the distribution profiles of target events (IESC, blue) and debris (red) for the variables compactness, form factor and eccentricity. (G) A new CellProfiler pipeline that identifies objects and applies filters based on the size and shape profiles of known IESCs is used to analyze segmented microwell images. If the number of objects initially identified by CellProfiler is equal to those that pass filtering parameters, the microwell passes inclusion criteria (G, top microwell), otherwise it is excluded as debris containing or empty (G, middle and bottom microwells). Scale bars represent 50  $\mu\text{m}$ . (H,I) Application of the optimized pipeline to randomly selected microwell images reveals an overall accuracy of 99.87%, 71.53%, 46.51% and 29.03% for wells containing 1, 2, 3 and 4 IESCs, respectively (n= 2,254 randomly selected microwells).

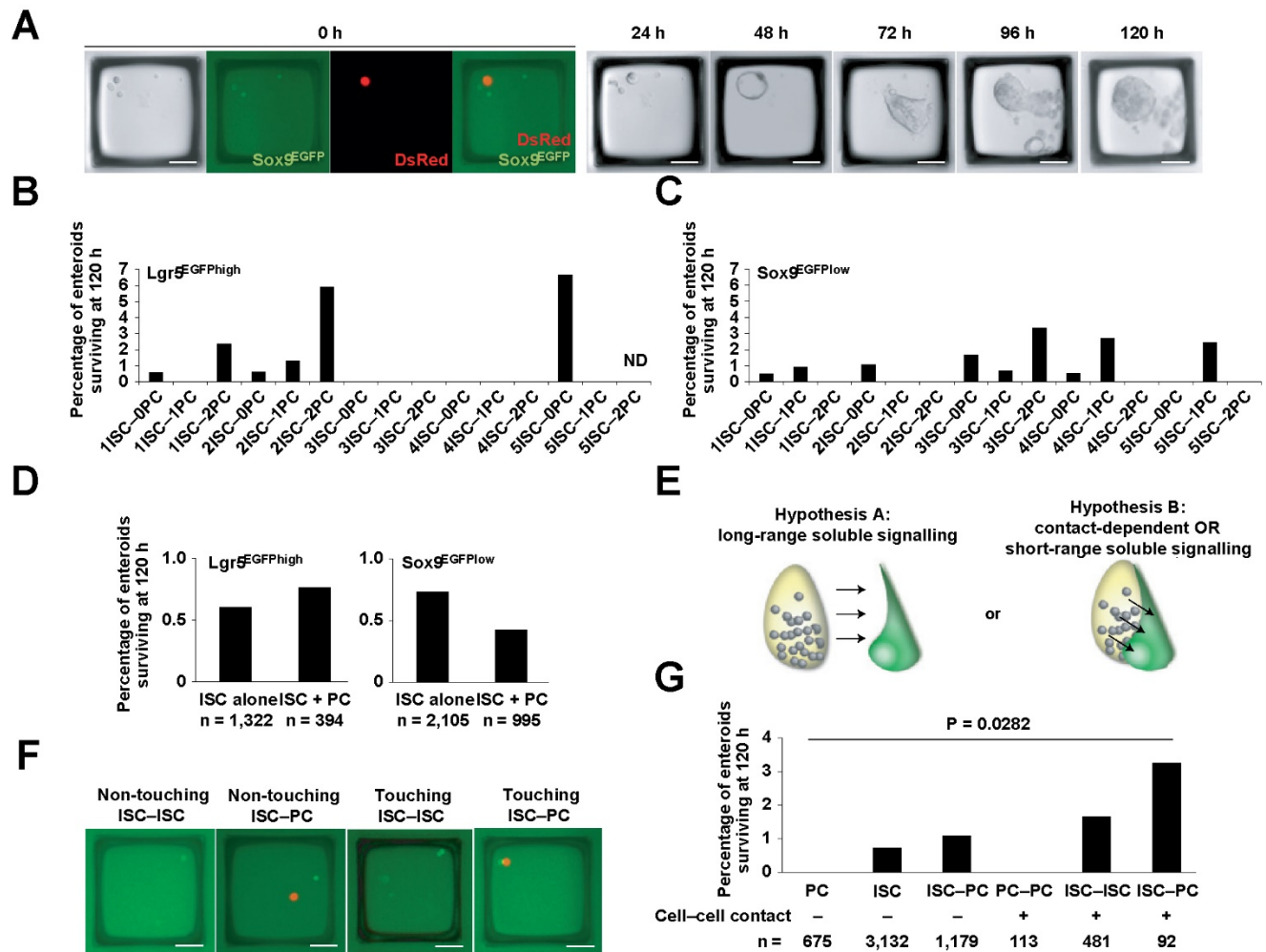


**Figure 4. Cell-to-cell contact is required for PC-influenced survival of IESCs in vitro.**

(A) PCs are isolated from Sox9<sup>EGFP</sup>:CAG<sup>DsRed</sup> mice and co-cultured with IESCs from Sox9<sup>EGFP</sup> or Lgr5<sup>EGFP</sup> mice lacking the constitutive DsRed transgene, allowing for independent tracking of IESC and PC growth in CRAs. (B,C) Quantification of organoid formation across 15 combinations of IESCs and PCs in experiments using IESCs isolated on the basis of Sox9 and Lgr5 biomarker expression demonstrates no significant increase in organoid formation at 120 hr associated with any one condition. Furthermore, we were unable to identify any clear trends between PC number and

organoid development by IESCs (conditional logistic regression, n= 816 microwells). (D) Analysis of overall organoid formation by IESCs alone and IESC–PC co-cultures, regardless of cell number per microwell, also fails to produce a significant effect associated with PC presence (conditional logistic regression, n= 816 microwells). (E) As all data were analysed post hoc from existing images, we were able to test the alternative hypothesis that cell–cell contact is required for PCs to have a niche effect *in vitro*. (F,G) Interestingly, when we grouped initial well contents by whether or not IESCs were in contact with other IESCs or PCs at t=0 hrs, we found that IESC–PCs in direct contact were more likely to form organoids than IESCs alone (conditional logistic regression, P=0.0282, n=5,672 microwells). Single PCs and PC–PC doublets did not form organoids and were excluded from statistical analysis. Data are derived from experiments conducted in replicate for each IESC biomarker. Cell-to-cell contact data are pooled from 8 independent CRAs from 4 Sox9<sup>EGFP</sup> and Lgr5<sup>EGFP</sup> animals. All scale bars represent 50  $\mu$ m.

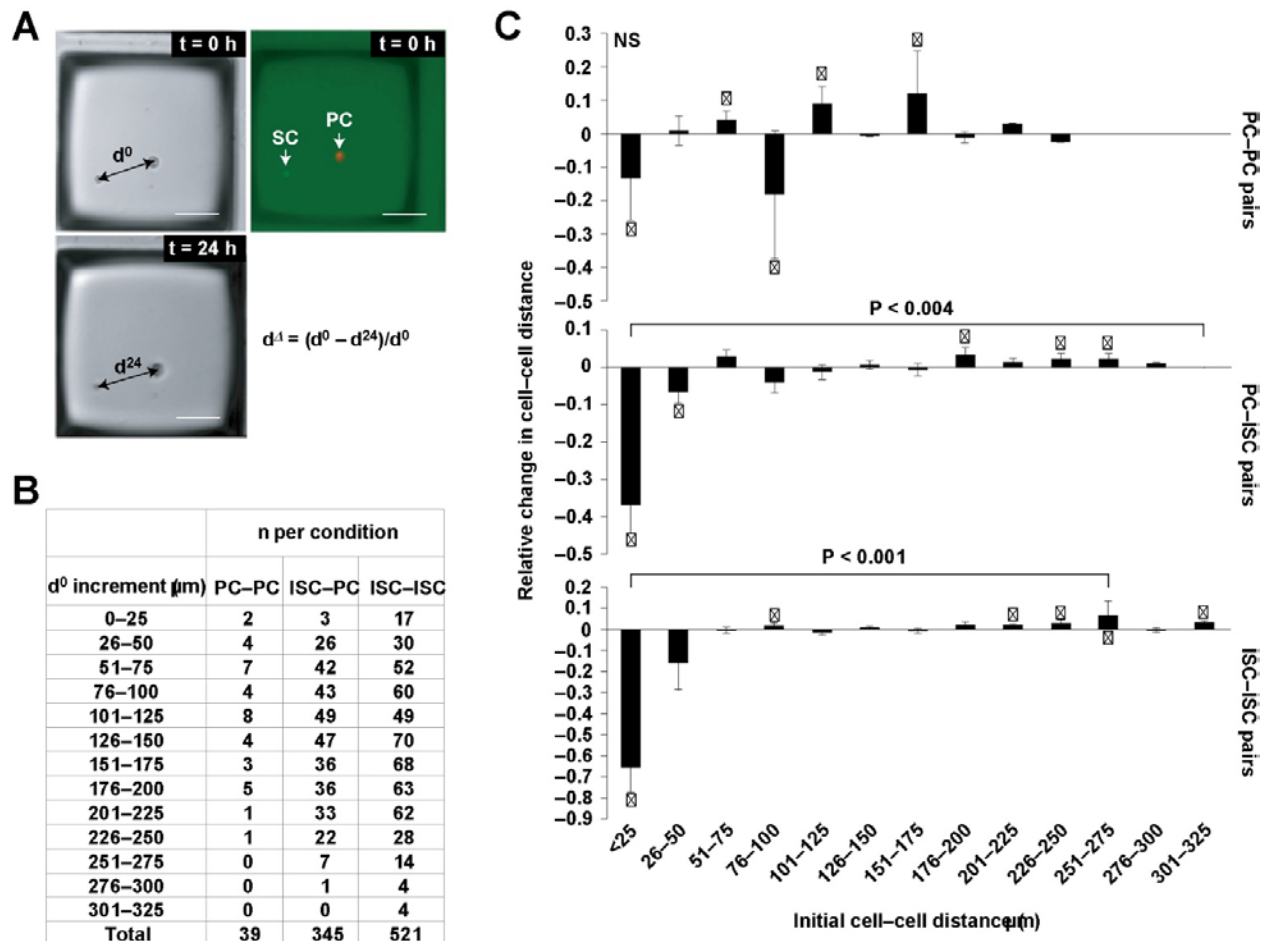


**Figure 5. Single cells do not form cell-cell contacts in microwells after initial plating.**

(A) Initial ( $d^0$ ) and 24 hr ( $d^{24}$ ) distances were measured from the centers of non-touching cells to determine positive or negative changes in distance, normalized to the initial distance ( $d^1$ ). To examine the possibility that cell-cell signaling might be affecting relative cell movement, pairs were grouped and compared in 25  $\mu\text{m}$   $d^0$  increments. SC: stem cell; PC: Paneth cell. Scale bars represent 50  $\mu\text{m}$ . (B) Number of non-touching pairs examined per distance. (C) Non-touching pairs of cells with a  $d^0$  value 25  $\mu\text{m}$  demonstrate statistically significant movement away from one another, relative to  $d^1$  associated with pairs having a  $d^0$  value  $>25$   $\mu\text{m}$ .  $d^1$  was calculated for pairs of fixed

cells (n=50) and compared with live cell movement to control for nonspecific changes in distance. Asterisks represent statistically significant movement, relative to fixed cells; error bars represent standard deviation. (unpaired t-test,  $P < 0.05$ ).

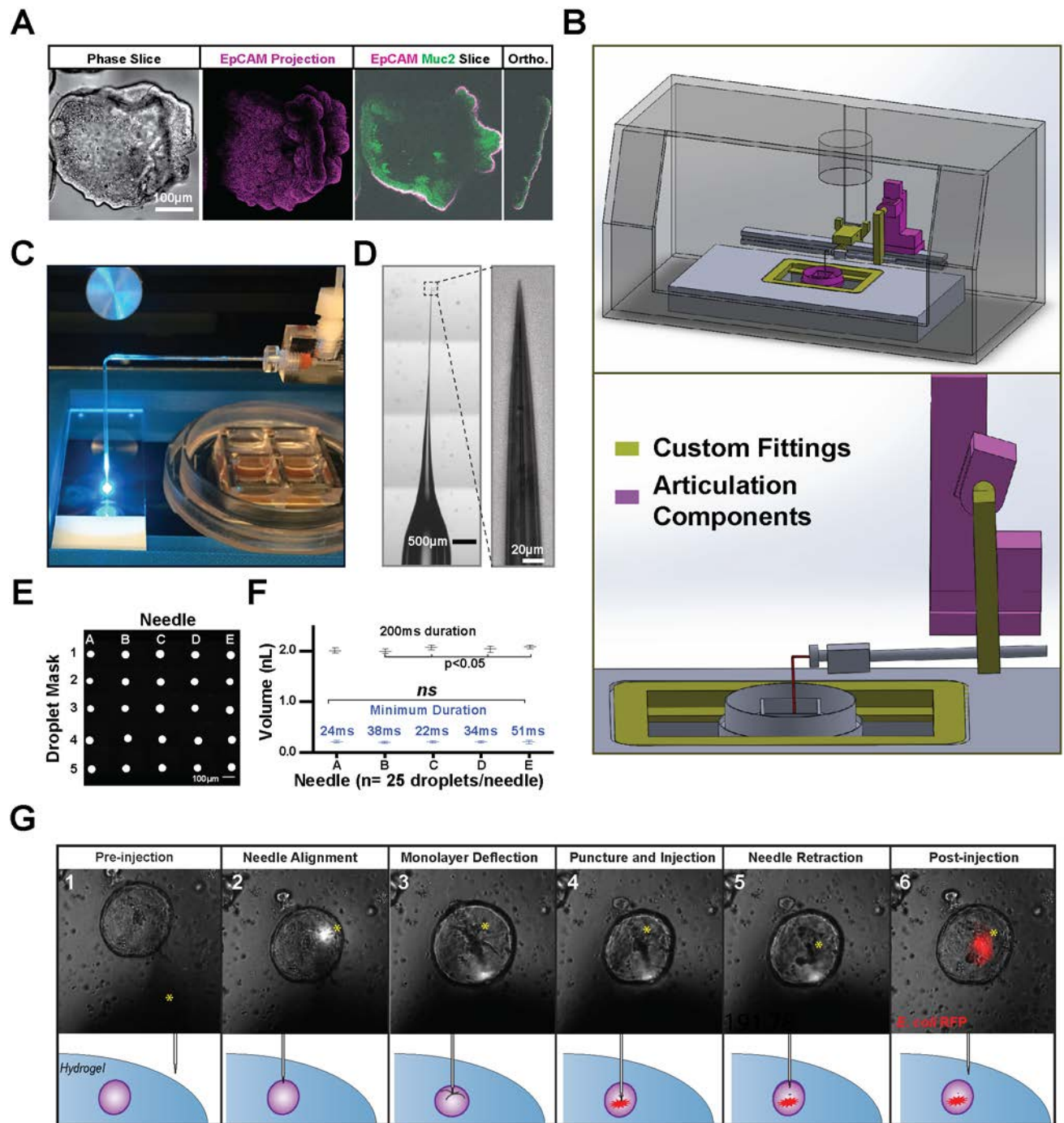


**Figure 6. Robotically Articulated Colonoid Microinjection Maintains Atmospheric Control Facilitating Long-term Sampling of Large Batches of Colonoids:**

A) Organoids grown from adult stem cells in 3D-culture form complex monolayers organized around a hollow, mucus filled “lumen” cavity analogous to the colon lumen. B) 3D-printed customized fittings were used to mount robotic microinjection hardware within an atmospheric imaging chamber of an automated imaging system. C) A 90° bend in the injection needle allows for vertical articulation of the microinjection needle minimizing hydrogel disruption and needle breaking during injections. D) Wet etching mechanically pulled borosilicate capillaries produces clean, fine aperture needles capable of injecting large batches of organoids without disturbing monolayer integrity. E) Computer vision made and measured the area of masks from images of the smallest droplets of fluorescent cargo delivered reproducibly by five replicate needles facilitating volume estimation. F) Optimized needles produce varying volumes at the same injection duration (black) but similar minimal volumes when the minimal duration reproducibly delivering cargo from each needle is used (blue). G) Organoid-microbe injections can be performed visually by locating an organoid of interest (1), aligning the needle to the organoid lumen (2), articulating the needle against the organoid monolayer distorting its appearance (3), puncturing the monolayer and injecting cargo (4), and retracting the needle from the organoid lumen (5) to visualize specific transplantation of DSRED expressing *E. coli* within the lumen (needle tip marked with \*).

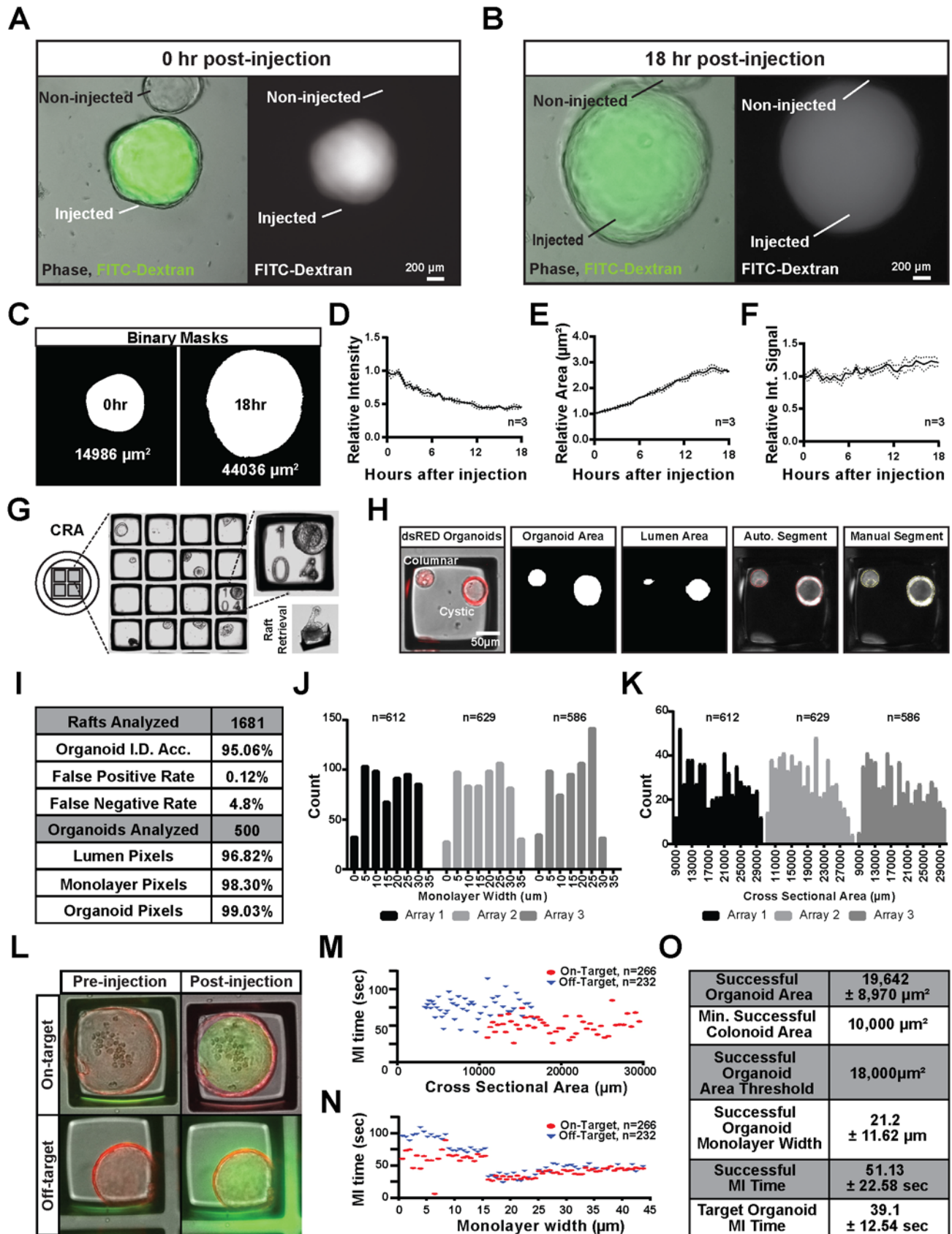
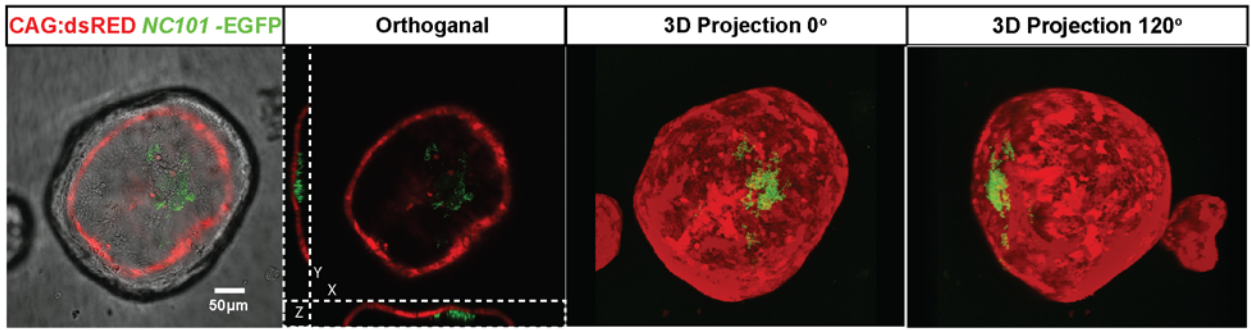


**Figure 7. Increasing Microinjection Throughput Using Computer Vision to Quantify Cargo Retention, Organoid Morphology and Injection Success:**

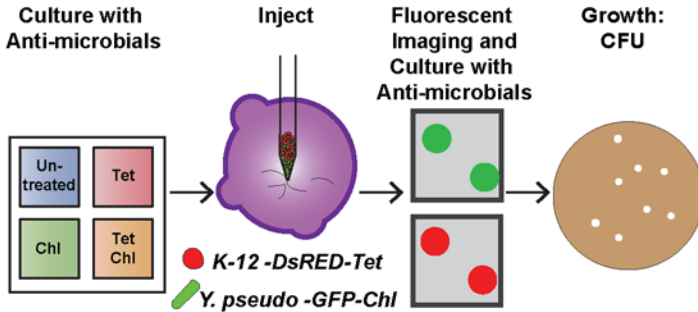
A) Inert high molecular weight fluorescent cargos fill the organoid lumen with no signal observed in the adjacent areas. B) Inert cargos are retained long term as the organoid expands in size over 18 hours. C) CellProfiler computational image analysis pipelines were used to create masks of the fluorescent signal of images collected during the 18-hour time course and quantified the area and mean intensity of the signal. D) The mean signal intensity observed from fluorescent inert cargos decreased over time to about half of the original intensity. E) The area of fluorescent signal doubled during the 18-hour time course as the organoid expanded in size. F) Integrated the fluorescent signal across the observed area shows relative stability suggesting that the inert cargo was retained within the organoid lumen. G) Culture protocols were optimized to grow organoids on 2.5 cm<sup>2</sup> microfabricated culture array devices containing retrievable 200 μm<sup>2</sup> rafts separated by 50 μm walls regularly addressed to facilitate downstream sampling. H) Modified CellProfiler image cytometry pipelines can identify DsRED fluorescent organoids and automatically segment identified organoids of varying morphologies into lumen and epithelial monolayer compartments. I) Automated organoid identification was >95% accurate (n=1681 rafts) allowing for >96% accurate lumen identification. J) Organoid cross-sectional area exhibited a bimodal distribution with an average of 18511 ± 5916 μm<sup>2</sup>. K) Organoid monolayer width also exhibits a bimodal distribution with an average of 16.4 ± 9.3 μm. L) The area and morphology of 500 DsRED expressing organoids was quantified before targeting each for microinjection with 0.36 nl of 7kD FITC-dextran solution, which could be observed

specifically within the lumen of successfully injected organoids with fluorescence signal observed outside the organoid of unsuccessful injections. M) Successfully injected organoids were larger ( $19642 \pm 8970 \mu\text{m}^2$ ) than unsuccessfully injected organoids ( $9142 \mu\text{m}^2 \pm 8970 \mu\text{m}^2$ ). N) Organoids with wider monolayers were injected in shorter intervals ( $51.1 \pm 35.6 \text{sec}$ ) than thinner organoids ( $74.1 \pm 35.6 \text{sec}$ ). O) Organoids larger than  $18,000 \mu\text{m}^2$  with monolayers  $> 15 \mu\text{m}$  wide were microinjected with the highest efficiency and accuracy with all targeted organoids of that range successfully microinjection in  $39.1 \pm 12.5$  seconds.

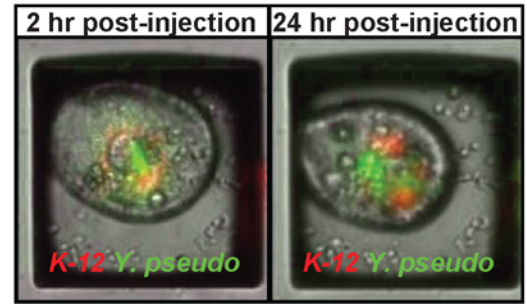
**A**



**B**



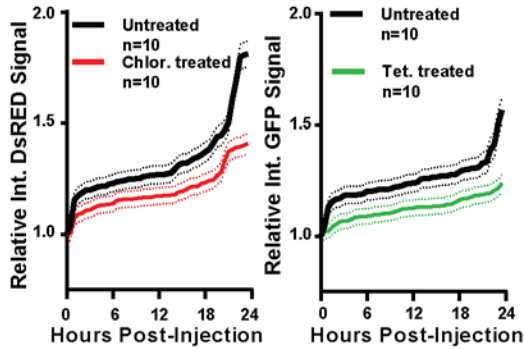
**C**



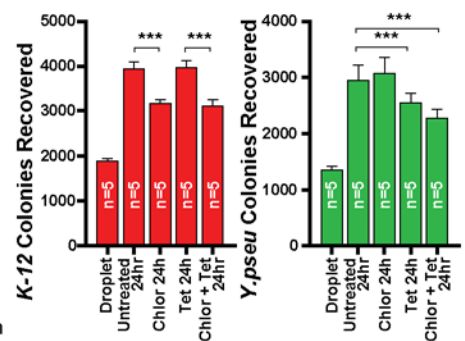
**D**

Media Activity	Media Tx				
	Tet	-	+	-	+
0hr	E,Y	E,Y	E,Y	E,Y	E,Y
12hr	E,Y	Y	E,Y	Y	Y
24hr	E,Y	Y	E	-	-
48hr	E,Y	Y	E	-	-

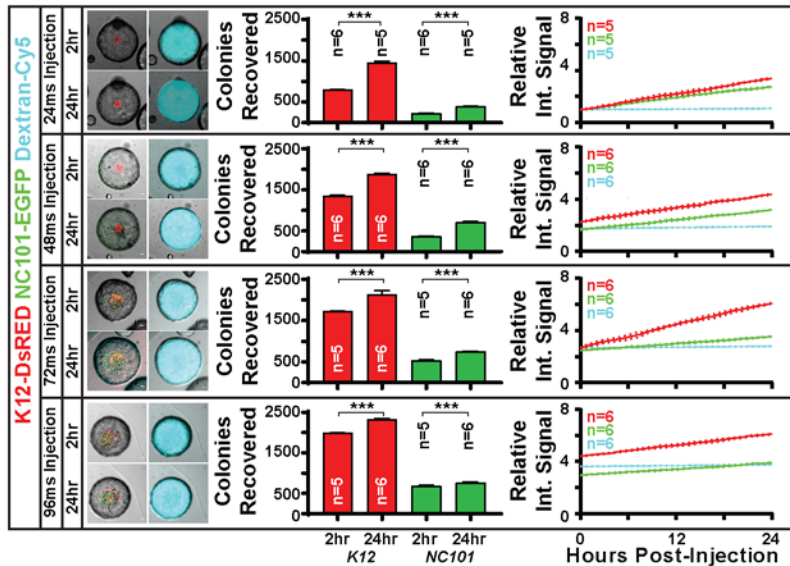
**E**



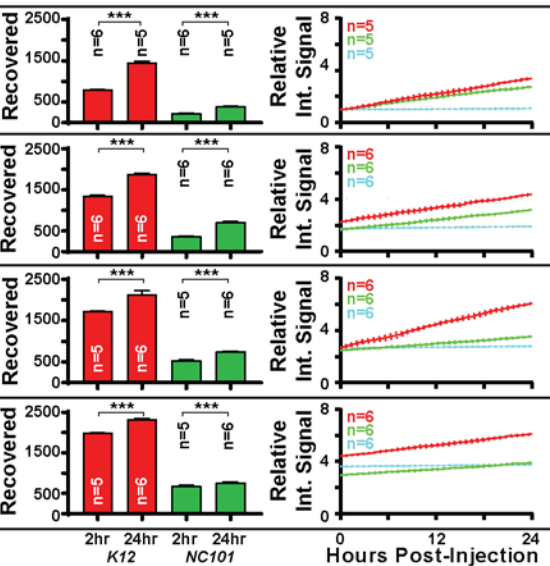
**F**



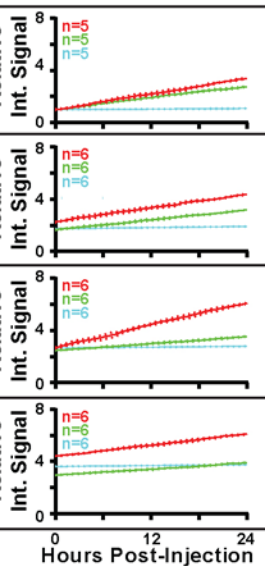
**G**



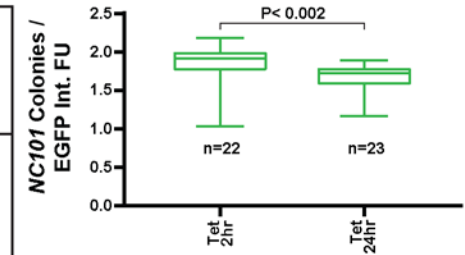
**H**



**I**



**J**



**K**

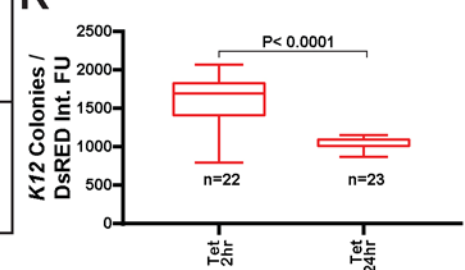


**Figure 8. The colonoid lumen forms a discrete compartment compatible with specific microbial growth:**

A) GFP expressing *E. coli* can be visualized after microinjection into DsRED expressing colonoids and appears to sit in the bottom of the lumen cavity in all colonoids observed.

B) The effects of antibiotics in the colonoid culture media on lumen microbe compatibility was investigated using a CRA device to culture colonoids in 4 discrete reservoirs treated with tetracycline and/or chloramphenicol. Colonoids from each well were targeted for microinjection with a mixed microbial culture of DsRED expressing *E. coli* resistant to tetracycline and GFP expressing *Y. pseudotuberculosis* resistant to chloramphenicol. Injected colonoids were monitored over time by live fluorescent imaging before lumen contents were harvested to assess microbial growth by colony formation on conventional agar plates.

C) Fluorescent signal from both microbes could be observed within the lumen of successfully injected colonoids during the entire time course.

D) Antibiotics were essential for preventing off target growth by excess bacteria delivered to the media during microinjection with no active microbes discovered in culture media treated with chloramphenicol and tetracycline 24 hours after microinjection.

E) Computational analysis shows an increase in integrated DsRED and EGFP fluorescence signal of raft images containing successfully injected colonoids suggesting an increase in DsRED and EGFP expressing microbes.

F) More *E. coli* and *Y. pseudo* colonies were recovered from the lumen of colonoids from all media conditions compared to the input injection droplet suggesting the colonoid lumen protected the injected microbes from chloramphenicol and tetracycline delivered in the culture media (n=10 colonoids in each condition). Significantly more colonies were

recovered from untreated colonoids correlating with increased integrated fluorescence signal. G) Fluorescent signal from both microbes as well as inert fluorescent cargo could be observed within the lumen of successfully injected colonoids during the entire time course. H) More K12 and NC101 colonies were recovered from colonoids collected 24 hours following microinjection compared to those collected immediately following microinjection suggesting that both microbes grew regardless of the delivered load (n=5-6 colonoids from each injection duration). I) Computational analysis shows an increase in integrated DsRED and EGFP fluorescence signal in injected colonoids suggesting an increase in DsRED and EGFP expressing microbes. Computational analysis also showed stable integrated Alexa Fluor 647 signal suggesting that delivered dextran was well retained. J) The measured ratio of recovered NC101 colonies to integrated EGFP signal varied significantly between the 2 hour and 24 hour timepoints suggesting that integrated EGFP signal cannot be used to directly measure *E. coli* NC101-EGFP microbial load. K) The measured ratio of recovered K12 colonies to integrated EGFP signal varied significantly between the 2 hour and 24 hour timepoints suggesting that integrated EGFP signal cannot be used to directly measure *E. coli*-DsRED microbial load.

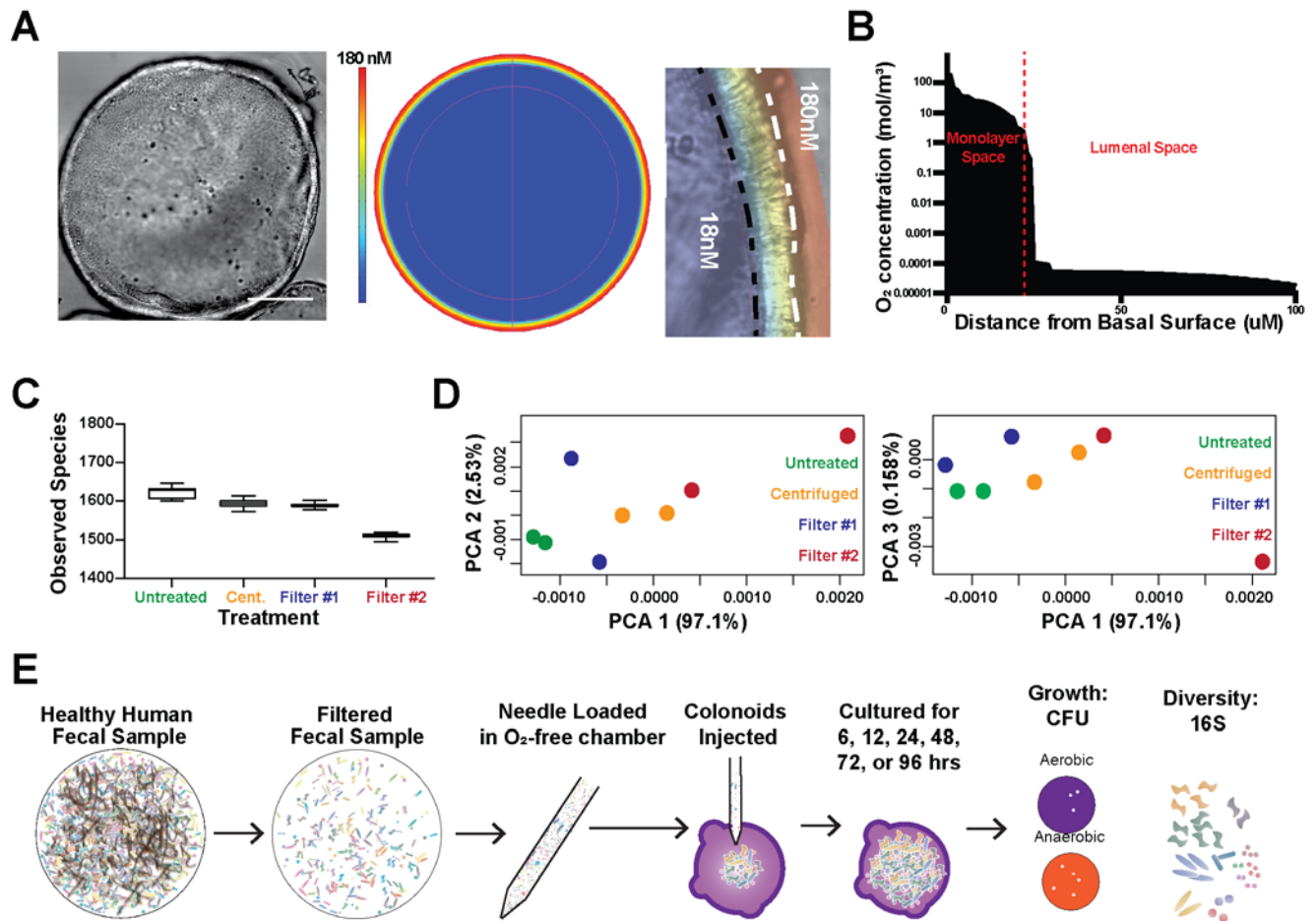


**Figure 9: Monolayer Respiration Makes the Colonoid Lumen a Hypoxic Environment Capable of Supporting the Growth of Anaerobic Enteric Microbes:**

A) COMSOL modeling of suggests the lumen of the average colonoid (left panel) is maintained in a state of hypoxia (right panel) due to respiration by the colonoid monolayer. B) Modeling suggests that O<sup>2</sup> levels drop rapidly from the basal to the apical colonoid surface to about 10% of atmospheric O<sup>2</sup> levels (180mM). C) Stool filtered using a 5 μm polyethylene glycol membrane (Filter #1) was compatible with microinjection needles and contained the majority of species present in the unfiltered or conventionally

processed (centrifuged) stool. D) Stool filtered using a 5  $\mu\text{m}$  polyethylene glycol membrane (Filter #1) showed greater similarity to the unfiltered and conventionally processed stool than stool filtered using a 5  $\mu\text{m}$  polypropylene membrane. E) Colonoid compatibility with human microbial populations was investigated by loading a filtered healthy human fecal sample into a microinjection needle under anaerobic conditions before 30 colonoids were microinjected with  $\sim 0.2$  nl of filtered stool. Injected colonoids were harvested across a 96hr time course and assessed for growth by colony formation in anaerobic and aerobic conditions.

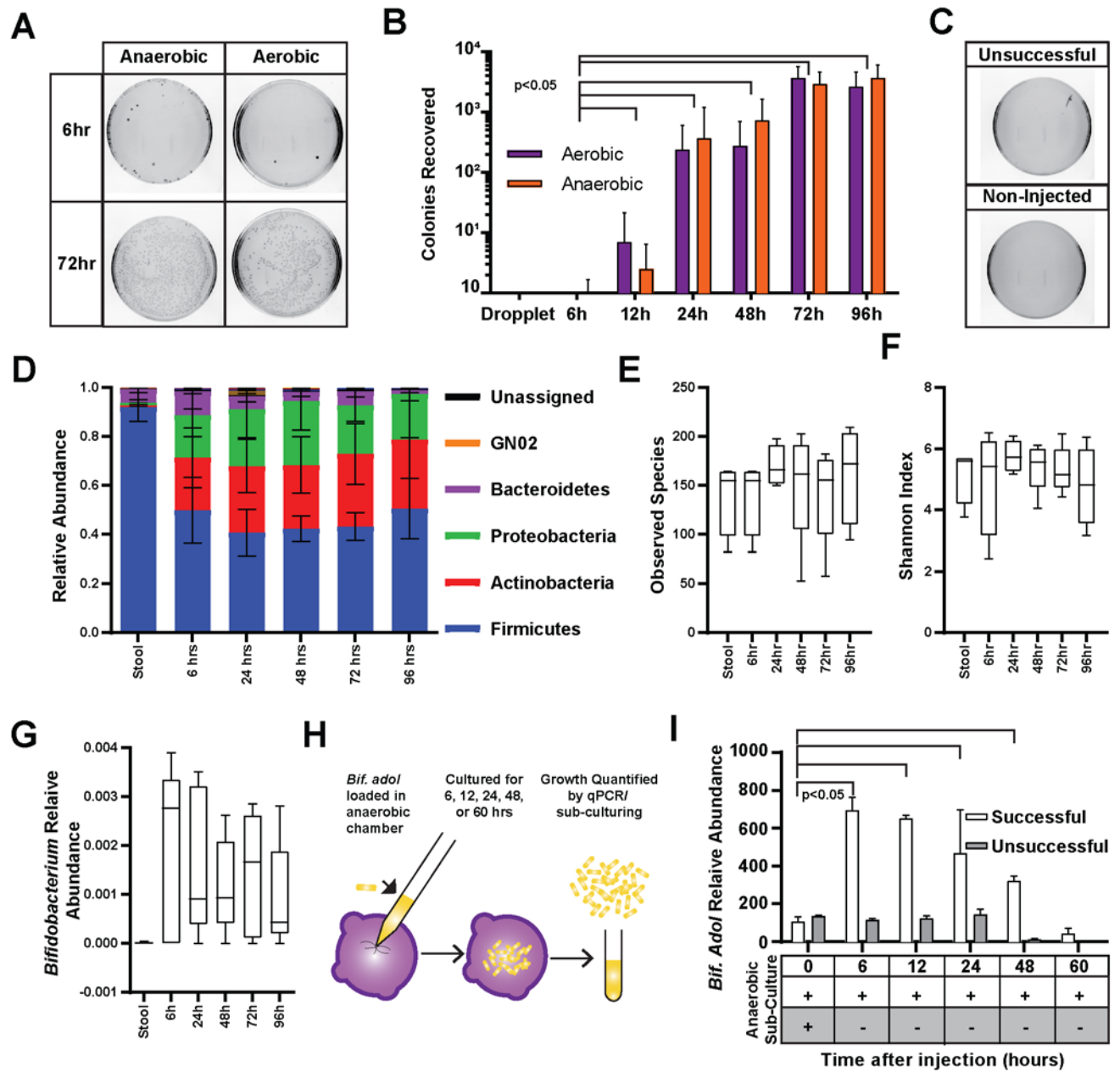


**Figure . The Colonoid Lumen Is Compatible with Patient Derived Microbial Communities and Non-sporulating Anaerobes:**

A) Few colonies were recovered from colonoids retrieved 6hrs following microinjection grown under anaerobic or aerobic conditions, with increasing microbial

loads recovered over time. B) Significantly more anaerobic and aerobic colonies were recovered from injected colonoids 12 hours following microinjection with microbial loads peaking 72 hours following microinjection. C) 10  $\mu$ L samples of the filtered stool collected and cultured under anaerobic conditions grew robustly as expected (top panel), while unsuccessfully and non-injected samples produced no colonies in either atmospheric condition (lower panels). D) The composition of the microbial communities changed quickly after injection but remained stable throughout the 96-hour time course with not significant shifts in 5 dominant phylum. E) No significant changes were observed in the number of species present in the microbial community following injection or incubation within the colonoid lumen. F) The even composition of the microbial community remained following injection and did not significantly change during the 96-hour time course. G) *Bifidobacteria*, a genus containing non-sporulating anaerobes and aerobes, were a minor member of the healthy stool sample and was detected at increased levels in the communities retrieved from colonoids. H) Colonoid microinjection compatibility with anaerobic non-sporulating microbes was verified by monoculture microinjection of *Bifidobacteria adolescentis* quantified by 16s qPCR and culturing. I) An increased abundance of *B. adol* was detected in successfully injected colonoids by targeted qPCR 6 hours following microinjection and was maintained for 48 hours with no increase observed in unsuccessfully injected colonoids. Active *B. adol* was recovered specifically from successfully injected colonoids by anaerobic culturing throughout the 60-hour time course suggesting that increases in 16S abundance was due to growth within the colonoid lumen.

## **Appendix A: In Vitro Polarization of Colonoids to Create an Intestinal Stem Cell Compartment**

### **Introduction**

Gradients of morphogens, differentiation factors and dietary metabolites are believed to participate in producing a polarized cellular architecture in the crypts of the colon and small intestine by regulating cell proliferation and position<sup>72,91,96,162</sup>. Within the crypt, the stem cells reside at the crypt base where they undergo self-renewal and produce proliferative transit amplifying (TA) progenitor cells. TA progenitor cells terminally differentiate and migrate up the long axis of the crypt to eventually populate the colonic epithelium with differentiated lineages: absorptive enterocytes, goblet cells, and enteroendocrine cells<sup>72</sup>. After cells reach the luminal surface, they undergo apoptosis but are replaced by a new generation of cells that maintain the functional absorption, secretion and barrier properties of the epithelium. Intestinal and colonic epithelial stem cells drive renewal of the epithelium every 4–7 days making it one of the most actively self-renewing tissue in the body<sup>163</sup>. It is believed that the orderly movement of cells along the crypt axis from the stem cell compartment to the luminal surface is orchestrated by both intrinsic and extrinsic signaling mechanisms involving gradients of mitogens and morphogens<sup>5,164</sup>. Crypt patterning is thought to be critically dependent upon the spatial organization of these signals with perturbations of key signaling pathways resulting in disrupted cell positioning and disordered epithelial renewal<sup>88,89,164,165</sup>. Despite established roles for certain factors in crypt patterning, less is known as to how discreet levels or gradients of a particular factor regulate crypt

morphogenesis<sup>166</sup>. Testing the impact of factor gradients such as Wnt-3a and R-spondin1 on crypt patterning is technically challenging. Studies to date have relied on indirect readouts of gradients using gene and protein expression, and genetic engineering of signal transduction pathways<sup>87,93–96,167</sup>, but have fallen short of directly testing the influence of gradients on specific cell types. Recently developed culture methods permit the culture of primary colonic epithelial organoids (e.g. colonoids) that possess stem cell and differentiated cellular compartments and self-pattern into crypt units. This major advance in the field now provides a physiologically relevant culture model to test important mechanisms that rely on factor gradients<sup>57,101</sup>. Colonoid culture requires defined growth conditions that mimic the stem cell niche environment, which promotes stem cell self-renewal and also appropriate differentiation. Essentially, cells are suspended in a 3-D extracellular matrix (Matrigel™), which is rich in collagen and laminin similar to the colonic basal *lamina propria*<sup>57,101</sup>. The culture system is further supplemented with a mixture of factors including Wnt-3a, R-spondin1/2, Epidermal Growth Factor (EGF), Noggin, and Jagged to maintain stem cell multipotency and self-renewal<sup>57,96,101</sup>. When placed in these defined culture conditions, isolated crypts or individual stem cells develop into colonoids with multiple cryptlike buds projecting randomly outward a central lumen from<sup>64</sup>. These buds have a vague resemblance to crypt architecture in vivo, and the colonoids often display a disorganized pattern of proliferating cells. The absence of properly formed crypts in the colonoids is likely due to the absence of factor gradients thought to be necessary to define appropriate cell-type locations. Conventional intestinal stem cell culture systems utilize standard tissue culture dishes which lack of spatial variation in concentrations of chemical factors have

hindered the ability to test the influence of fundamental, morphogenic cues in crypt homeostasis and cellular organization. Microfluidic culture systems, however, can readily sustain both simple and complex gradients over sustained times<sup>168–170</sup>. Some of these devices also possess the capability to chemically pattern the environment surrounding cells and tissues<sup>170</sup>, so that a device with gradient-forming capabilities can recreate a physiologically-relevant microenvironment for testing mechanistic hypotheses. Microfluidic devices incorporating gut-derived tumor cells or primary mouse intestinal cells have been described for a number of assays on epithelial cells; however, none have been utilized to replicate the complex 3-D architecture of the colonic crypt<sup>58,171,172</sup>. Efforts have been made to produce scaffolds with a 3-D architecture including crypt- like invaginations in an attempt to place tumor cells into the shape of an intestinal epithelial surface<sup>173–175</sup>. For the most part these studies have employed Caco-2 cells, a tumor derived model gut epithelial cell line, as a surrogate for the intestinal epithelium. While simple to maintain in culture, this tumor cell line has little resemblance to normal epithelium in terms of growth factor response, gene expression and susceptibility to apoptosis making it a poor mimic of the in vivo condition<sup>176</sup>. One report used primary murine and human intestinal organoids within a Matrigel layer to promote growth on the surface of a scaffold, but neither the crypt morphology or polarity were recapitulated<sup>175</sup>.

Recently our group described a microfluidic gradient device specifically developed for optimizing growth factor concentrations for the efficient culture of colonoids<sup>92</sup>. In this study colonoids were grown within a gradient-channel that exposed each colonoid to a distinct concentration of Wnt and/or R-spondin1 enabling the survey

of a wide range of factor concentrations. Colonoids at different ends of the factor gradient displayed distinct phenotypes, i.e. differentiated or stem/proliferative cells. However, no individual colonoid demonstrated polarized locations of proliferative and differentiated cellular compartments. The absence of cell segregation within a single colonoid was likely due to a shallow gradient imposed across each colonoid effectively placing the entire organoid within the same chemical environment. In the present work, we optimize a microengineered, gradient-forming device to create a steep Wnt-3a and/or R-spondin1 gradient across the length of a single colonoid exposing the cells within the same tissue subunit to different concentrations. The goal was to determine whether a simple, linear gradient of 1 or 2 factors was sufficient to produce polarization of proliferative and differentiated cellular compartments along a colonoid length.

## **Materials and Methods**

### **Transgenic Mouse Models and Isolation of Colonic Crypts**

Crypts were isolated from either Sox9EGFP mice or Sox9EGFP-CAGDsRed mice (6–9 weeks old) using previously described methods<sup>92</sup>. The CAGDsRed mouse line ubiquitously expresses the red fluorescent protein DsRed under the control of a chicken beta-actin promoter (CAG). The Sox9EGFP mouse possessed the Sox9 promoter controlling Sox9EGFP (enhanced green fluorescent protein) expression on a modified bacterial artificial chromosome<sup>13,115,177</sup>. Mice genetically engineered with this construct express Sox9EGFP in intestinal stem cells and TA cells<sup>13,115,177</sup>. Crypts were obtained from colons harvested from mice that were bred, handled and sacrificed under protocols approved by the University of North Carolina at Chapel Hill Institutional Animal Care and Use Committee (<http://research.unc.edu/offices/iacuc/>). The University of

North Carolina at Chapel Hill Institutional Animal Care and Use Committee approved the animal work described in this paper (approval #13–200). Prior to euthanasia, all mice are anesthetized with isoflurane followed by cervical dislocation to minimize any stress or pain. Single intestinal stem cells were obtained from crypts harvested from heterozygous Sox9-EGFP:CAGDsRED mice between 6 and 10 weeks of age by fluorescence-activated cell sorting (FACS) (S1 Methods).<sup>115</sup>

### **Colonoid Culture**

Culture media (CCM) was prepared as previously described<sup>92</sup> and consisted of a mixture of advanced DMEM/F12 medium (Invitrogen), Wnt-3a (120 ng/mL) and R-spondin1 (175 ng/mL) unless otherwise specified. CCM also contained Noggin (100 ng/mL), EGF (50 ng/mL), Y27632 ROCK inhibitor (10  $\mu$ M), NAC (1 mM), GlutaMAX (1 $\times$ ), HEPES (10 mM), penicillin (100 unit/mL), and streptomycin (100  $\mu$ g/mL). Wnt-3A and R-spondin1 were prepared from conditioned medium as described previously or purchased purified from a supplier (R&D Systems, Minneapolis, MN). The CCM was prepared in a bulk volume of 500 mL, split into 6-mL aliquots, and stored at -80°C until use. For crypt culture, 100% Matrigel (Dow Corning, Midland, MI) was used. Crypts were isolated from the distal colon of a mouse as previously described<sup>56,96,119,153–156</sup>. The crypts were pelleted by centrifugation at 300 $\times$ G for 90 s. The supernatant was aspirated and the crypts were mixed with cold liquid Matrigel (100% in CCM, 4°C). A 1 mL suspension of freshly isolated crypts (5000 crypts/mL) was added to standard 12-well plates at 4°C. The Matrigel was then polymerized for 15 min at 37°C. After polymerization, 1.5 mL of CCM was overlaid onto the Matrigel. After 5 days in culture, colonoids were retrieved from the Matrigel using collagenase digestion (15 min, 37°C)

and then fragmented using trypsin/EDTA (2 min, 37°C in 0.02 mM trypsin and 0.48 mM EDTA). The slurry was pipetted vigorously for 30 s to break the colonoids into multicellular fragments. These colonoid fragments were then rinsed, counted and re-embedded in Matrigel for culture in CCM. This process was repeated to grow colonoids in continuous culture as well as to prepare fragmented colonoids to load into the microdevice.<sup>3,89,117,118,150,153–157</sup>

### **Diffusion-Based Gradient Generation and Characterization**

Devices were fabricated as described in S1 Methods. Gradient formation through the Matrigel layer on the device was characterized by imaging the movement of a 40 kDa fluoresceinlabelled dextran (Sigma-Aldrich, St. Louis, MO) in 100% Matrigel by time-lapse imaging using an Olympus MVX10 Macroview microscope. Fluorescence images were acquired every 15 min over 24 h to measure gradient formation. The volume of the source and sink was 500  $\mu$ L and that of the channel was 1.5  $\mu$ L. Gradient formation over time was modeled using Fick's Law:<sup>178</sup>

$$C(x, t) = A + \frac{1}{2} C_o \operatorname{erfc} \left( \frac{x}{2\sqrt{(Dt)}} \right)$$

where A is a constant, x ranges from 0 to 1 mm corresponding to the positions along the length of the channel, t is time, D is the diffusion coefficient, erfc is the complementary error function, and CO is the concentration of the species of interest loaded into the source. COMSOL Multiphysics with finite-element analysis (FEA) was used to model the data. For experiments applying gradients to colonoids, the media in both the source and sink were replaced every 24 h.

## **Culture of Colonic Cells in the Microchannel of the Gradient Device**

Before use, the device was sterilized with 70% ethanol and rinsed with phosphate buffered saline (PBS)  $\times 5$ . The gradient-generating region of the device was pre-coated by incubation with 2% Matrigel in PBS for 6 h at 4°C and then rinsed with PBS  $\times 3$  prior to loading cells. This pre-coating step resulted in deposition of a thin Matrigel surface layer on the channel walls which improved subsequent cell/Matrigel loading into the gradient region and enhanced adhesion of the gelled plug to the device walls. Cells were mixed with cold liquid Matrigel (100% in CCM, 4°C) and loaded into the device's gradient-generating region. The Matrigel plug was gelled by incubation at 37°C for 15 min. Once the Matrigel solidified, CCM (500  $\mu$ l) was immediately added to each reservoir. For experiments in which a gradient was formed, Wnt-3a and/ or R-spondin1 were omitted from the CCM added to the sink as indicated in the text.

## **Microscopy**

Colonoid formation and growth was monitored over time using a Nikon Eclipse TE2000-U microscope fitted with a Photometrics Cool SNAP HQ2 digital camera. Objective lenses used were 10 $\times$  and 20 $\times$  with numerical apertures of 0.30 and 0.55, respectively. Fluorescein-dextran diffusion in the microchannel was tracked by wide-field imaging of the entire device using an OlympusMVX10Macroview fluorescence microscope with a 1.0 $\times$ , 0.25 N.A. objective and 0.63 $\times$  demagnification. Confocal images of gradient formation were obtained using a Zeiss CLSM710 Spectral Laser Scanning Microscope equipped with a 488 nm laser to excite fluorescein.

## **Immunofluorescence and EdU Assays**

Crypts isolated from a Sox9EGFP-only mouse were used for immunofluorescence staining to avoid interference from the DsRed fluorescence. For immunofluorescence staining, crypts or colonoids were fixed with 4% paraformaldehyde for 20 min, followed by permeabilization with 0.5% Triton X-100 (Thermo-Fisher, Waltham, MA) for 20 min. After rinsing  $\times 3$  with PBS containing 100 mM glycine, the sample was incubated in immunofluorescence wash (0.2% Triton X-100, 0.1% BSA, 0.05% Tween-20, 7.7 mM NaN<sub>3</sub> in PBS and 5% normal goat serum) for 90 min to block nonspecific binding. The polyclonal rabbit  $\alpha$ -Muc2 primary antibody (1:200, Life Sciences) in immunofluorescence wash was then incubated with the sample for 12 h at 4°C. Secondary antibody ( $\alpha$ -rabbit-Cy3, 1:500, Life Sciences) in immunofluorescence wash was then incubated with the sample for 45 min. All nuclei were stained with Hoechst 33342 (10  $\mu$ g/ mL in PBS) using a 30 min incubation. Microdevices were imaged by brightfield and fluorescence microscopy. An EdU-based assay was also used to identify cells undergoing active DNA syndissertation in S-phase of the cell cycle per manufacturer's protocol (Life Technologies, product #10640).

## **Colonoid Segmentation using DsRed or Hoechst 33342**

A custom script written in MATLAB (MathWorks; Natick, MA) was used to segment the colonoids by identifying DsRed or Hoechst 33342 positive pixels. Fluorescence images were filtered using a top hat filter with a disk-shaped structuring element to remove background fluorescence and uneven background illumination<sup>179–181</sup>. The images were then thresholded using minimum cross entropy thresholding<sup>180</sup>. In the resultant binary image, all interior holes within objects were filled and objects with a total

area less than  $1000 \mu\text{m}^2$  were removed to generate a mask of the segmented colonoids (S1 Fig). Brightfield images were then used to remove large cellular debris by applying a Chan-Vese active contour to the brightfield image using the previously generated mask as an initialization<sup>179</sup>. Cellular debris was defined as objects that possessed brightfield segmentation boundaries that were 20% larger than the segmentation boundary obtained from the DsRed or Hoechst fluorescence suggesting an object consisting of noncellular or degrading cellular material. The area of each colonoid was determined and used as a proxy for the total number of cells within each colonoid.

### **Measurement of the Percentage of Colonoids Positive for a Fluorophore**

Colonoids were identified and segmented as described above based on either DsRed or Hoescht 33342 fluorescence. The fluorescence images of the Sox9EGFP, Muc-2 immunofluorescence staining, or the EdU fluorophore were filtered to reduce background noise (top-hat filtering) and the fluorescence intensity of each pixel previously identified as being within the boundaries of a colonoid (using the DsRed or Hoescht 33342 mask) was summed. The number of pixels positive for EGFP, Muc-2 immunofluorescence staining, or the EdU fluorophore was then quantified based on empirically set fluorescence intensity thresholds for these fluorophores (in comparison to control samples). Based on empiric observation, colonoids were marked as positive for Sox9EGFP, Muc-2 or EdU if 25%, 10%, or 25% of the pixels, respectively, in the colonoid were positive for the fluorophore.<sup>92</sup>

### **Measurement of Sox9EGFP Polarization in a Colonoid**

Colonoids were segmented as described above. The DsRed mask obtained for the segmented colonoids was applied to the Sox9EGFP fluorescence image to identify

the colonoid boundaries in the Sox9EGFP image. Sox9EGFP fluorescence intensity was then divided by DsRed intensity for each pixel. This acted to normalize the Sox9EGFP fluorescence with respect to the cell number in different regions of the colonoid. Each colonoid was then cropped from the resultant image. Within each cropped image, the mean intensity of a 20- $\mu$ m horizontal slice through the center of the colonoid was calculated to generate an intensity profile along the center of the colonoid. The cropped image was rotated by 1 degree about the centroid of the bounding box of the colonoid using nearest neighbor interpolation and the mean intensity of a 20- $\mu$ m horizontal slice through the center of the colonoid was again calculated. This was repeated for 180 degrees of rotation. A linear fit was performed on each intensity profile to obtain the slope of that profile. The rotated image that produced the largest absolute value of the slope was identified. The angle of the rotated image and sign of the slope determined the direction of colonoid polarization. The absolute value of the slope of the linear fit was used as the magnitude of the polarization (S2 and S3 Figs).

### **Measurement of EdU Polarization in a Colonoid**

Colonoids were segmented based on Hoechst 33342 and the EdU image divided by the Hoechst 33342 image as described above for Sox9EGFP and DsRed. This acted to normalize the EdU fluorescence with respect to the cell number in different regions of the colonoid. Each colonoid was then cropped from the resultant image. Since a minority of cells stained with EdU, the EdU fluorescence exhibited a punctate distribution in images (unlike Sox9EGFP fluorescence). For this reason the polarization measurements were altered for the EdU-based measurements. For each segmented colonoid, the Hoechst 33342 geographic centroid and the EdU intensityweighted

centroid were identified. The angle of the vector between the two points was used as the angle of polarization. The magnitude of the vector was normalized to the total length of the colonoid (length along the axis of polarization) (S4 Fig). For EdU polarization measurements, the axes were defined as described for the Sox9EGFP polarization measurements.

## **Statistics**

Boxplots were used to represent the non-normal distribution of colonoid area and Sox9EGFP fluorescence intensity of the developing colonoids<sup>182</sup>. Within the boxplots, stars represented the mean, a bar represented the median, and the upper and lower boxes showed the 75% and 25% percentile of the data, respectively. The whiskers extended to the 5th and 95th percentile with outlying data shown as individual points. The data are presented in the text as medians, first- and third-quartile values for colonoid DsRed area and colonoid Sox9EGFP fluorescence intensity within the regions. For statistical comparison, the data were converted to a normal distribution using a logarithmic transform and then assessed using Q-Q plots for their fit to a normal distribution. The adjusted coefficient of determination (R<sup>2</sup>) values for the Q-Q plots was always 0.91. Statistical differences between data were identified using a Holm-Sidak t test in the analysis of variance<sup>183</sup>. Data are also presented as average  $\pm$  standard deviation where appropriate, with the compass plot data being represented as the standard deviation. Propagation of uncertainty using the standard deviation was used to calculate the variation in the Sox9EGFP/EdU polarization angle and magnitude. Once this was found, statistical differences in the compass plot data were assessed using a Holm-Sidak t-test to determine whether the differences in polarization directions of

colonoids grown in the presence of specific gradients was statistically significant<sup>184</sup>. Similarly, a Holm-Sidak t-test was used to examine the statistical differences between the percentages of colonoids possessing stem/TA cells (Sox9- EGFP), goblet cells (Muc2+) and actively proliferating cells (EdU+) in colonoids cultured in the microchannel and the multiwell plate (S5 Fig). For all statistical analyses, a p-value less than 0.05 was considered to be significant.

## **Results and Discussion**

### **Design and Characterization of Gradient-Microdevice**

Poly(dimethylsiloxane) (PDMS) was selected as the material of choice for the device as PDMS is gas permeable and compatible with colonic stem cell culture<sup>92,185</sup>. Devices formed from PDMS are also readily fabricated using soft lithography<sup>186</sup>. The device incorporated a central microchannel (1×5×0.3 mm with a volume of 1.5 μL) across which a linear gradient (1 mm in length) was formed between two large fluid reservoirs. The two fluid reservoirs (16×16×5 mm with a volume of 1.3 mL) were placed to either side of the microchannel and served as a source or sink (Fig 1A and 1B and S6 Fig). Matrigel was loaded into the central channel via a small inlet and outlet port (1.5 mm diameter) at the ends of the microchannel. An array of hexagonal posts (250 μm height, 6 μm face and 50 μm inter-post spacing) bounded the sides of the gradient-generating region and acted to localize Matrigel to the central microchannel via surface tension forces. Every third post was labelled with a number permitting the channel location to be reproducibly identified over time during microscopy. The diffusion of fluorescein-labeled dextran (40 kDa) was used to characterize the time evolution and stability of a gradient formed across the 1-mm width of the Matrigel-filled microchannel.

Fluorescein-dextran was loaded into the source reservoir and the microchannel was imaged over time. By 1 h, a gradient of fluorescence had begun to form across the microchannel decreasing linearly from the concentration in the source to that in the sink. When the temporal evolution of the fluorescence intensity was fit to Fick's Second Law of Diffusion, a diffusion coefficient of  $7.2 \pm 0.6 \times 10^{-11}$  m<sup>2</sup>/sec (n = 3 devices) was calculated for the fluorescein- dextran which was similar to that measured by other investigators for the 42-kDa protein vascular epithelial growth factor in Matrigel ( $7.0 \times 10^{-11}$  m<sup>2</sup>/sec) (S7 and S8 Figs)<sup>187,188</sup>. To maintain the linear gradient over long time scales (5 days), the source and sink solutions were replaced every 24 h. Modeling the device and solution changes suggested that once a gradient was established, the concentration of a 40 kDa analyte across the microchannel varied by no more than 0.9% over a 5 day period (S9 Fig). The daily reservoir refreshment combined with the 870x volume of the source and sink reservoirs relative to that of the gradient-forming microchannel enabled the source and sink reservoirs to behave as infinite compartments and permit formation of a time-invariant molecular gradient<sup>189</sup>. Similar gradient strategies have been employed successfully by others. These data also suggest that stable, linear gradients of Wnt-3a (39.7 kDa) and R-spondin1 (40.0 kDa) could be formed across the Matrigelfilled microchannel.<sup>189,190</sup>

### **Microchannel devices support colonoid development similar to conventional cultures**

Colonoid growth in a standard format (12-well plate) was compared to that on the microdevice in the absence of factor gradients. Dual transgenic reporter mice (Sox9EGFP:CAGDsRed) were used to identify and monitor changes in stem/progenitor

cells and differentiated cells. Sox9-EGFP marks stem/progenitor cells and CAGDsRed is ubiquitously expressed in all cells. As cell differentiate, DsRed-only expression serves as a proxy marker for differentiated cell types<sup>115</sup>. DsRed+ colonoid area was used to determine colonoid size. Freshly isolated crypts were mixed with Matrigel and loaded into the microchannel. Wnt-3a (60 ng/mL) and R-spondin1 (90 ng/mL) were placed into both the source and sink reservoirs and replenished every 24 h during culture. In parallel, crypts were cultured in a conventional Matrigel patty placed in a multiwell plate and overlaid with media containing 60 ng/mL of Wnt-3a and 90 ng/mL of R-spondin1. The media was replenished every 24 h for both formats. Of the Sox9EGFP-CAGDsRed crypts plated in the microdevice,  $55 \pm 14\%$  (avg.  $\pm$  s.d.) developed into colonoids with a median DsRed area/colonoid of  $13,236 \mu\text{m}^2$  (S1 Table). In comparison,  $60.0 \pm 8.5\%$  of crypts plated and cultured for 5 days in the Matrigel patties developed into colonoids with a median DsRed area/colonoid of  $12,752 \mu\text{m}^2$  after 5 days in culture (Fig 1D and S1 Table). The presence of a differentiated cell type producing mucous (Goblet cells) was assayed by immunofluorescence staining of Mucin 2 (Muc-2) after Sox9EGFP crypts were plated in the microdevice and cultured for 5 days<sup>13</sup>. The percentage of colonoids in the microchannel with Goblet cells (Muc-2+ staining in 10% of the colonoid area) was  $90 \pm 5\%$  compared to  $92 \pm 7\%$  in the multiwell plate (Fig 1C, S5 Fig and S2 Table). These data indicate that microchannels support colonoid development and differentiation similar to convention Matrigel-patty cultures. To assess the impact of the microchannel devices on proliferative cells, Sox9EGFP crypts were plated into microchannels or the conventional platform and cultured for 5 days. Sox9-EGFP expression and EdU were used to assess the numbers of proliferative stem/progenitor

cells in all colonoids on the devices. The percentage of colonoids demonstrating Sox9EGFP expression in 25% of the colonoid area was similar for the microchannel and conventional multiwell environments with  $83 \pm 8\%$  and  $85 \pm 9\%$  of colonoids positive for Sox9EGFP, respectively (S3 Table). The median integrated Sox9EGFP fluorescence/colonoid in the microchannel was 118,822RFUs (S4 Table). In comparison, the median integrated Sox9EGFP fluorescence/ colonoid in the multiwell plate was 133,490 RFUs (Fig 1D and S3 Table). A second assay based on an EdU pulse, which marks cells in the S-phase of the cell cycle, was used to quantify proliferating cells<sup>191</sup>. The percentage of colonoids in the microchannel with EdU+ cells (occupying >25% of the colonoid area) was  $96 \pm 3\%$ , compared to  $92 \pm 7\%$  in the standard Matrigel patty on the multiwell plate (Fig 1C and S5 Table). These data indicate that microchannels and multiwells yielded colonoids containing similar numbers of proliferating stem/progenitor cells.

### **Colonoids do not demonstrate overall polarization in the absence of an external gradient**

The localization of Sox9EGFP within colonoids in the absence of an external chemical gradient was assessed to determine the extent to which individual colonoids might polarize the stem/ progenitor cell compartments on the microchannel devices. Colonoids derived from a Sox9- EGFP-CAGDsRed mouse were loaded into microchannels or multiwell plates and cultured in the presence of Wnt-3a (60 ng/mL) and R-spondin1 (90 ng/mL). We developed vector-based computational image analysis pipelines to measure the relative location of Sox9EGFP expressing cells in the colonoid. For the microchannel device, a line perpendicular to the long axis of the microchannel

was defined as the line through 0 to 180 degrees. Zero and 180 degrees were arbitrarily defined for each multiwell plate, but was consistent across all wells. A Sox9EGFP polarization vector was calculated by searching for the steepest gradient in Sox9EGFP intensity as the colonoid was rotated through 180 degrees. Using this strategy, an unpolarized colonoid is characterized by a Sox9EGFP vector magnitude that approaches zero while a highly polarized colonoid is near 0.04. For the conventional multiwell platform, the average Sox9EGFP polarization vector possessed a length of  $0.0006 \pm 0.0006$  and an angle of  $150 \pm 110$  degrees. The colonoids in the microchannel displayed an average Sox9EGFP polarization vector with a length of  $0.0009 \pm 0.0007$  and an angle of  $152 \pm 107$  degrees. When the Sox9EGFP polarization angle was examined for each colonoid in both the multiwell plate and microchannel, the angle appeared to be randomly distributed through all quadrants and the magnitude of the vectors near zero. Additionally, the initial location of a colonoid in the microchannel or multiwell plate had no impact on its likelihood of being polarized (S10 Fig and S6 Table). Thus, colonoids cultured under these gradient-free conditions displayed Sox9EGFP fluorescence nearly equally distributed about the colonoid in all locations of both culture formats (Fig 2). Using a similar vector-based approach, we assessed the extent to which the proliferative cell compartment (marked by EdU) was polarized in the absence of an external gradient. Colonoids were cultured in both microchannel and conventional platforms for 5 days at which time EdU was added to the culture for 2 h. Since only a small subset of cells were marked by EdU, the algorithm used for Sox9EGFP polarization could not be employed. Instead the geographic centroid and the intensity-weighted centroid were identified and the vector between these two locations

was used to assess EdU polarization. Using this algorithm, unpolarized colonoids possessed an EdU vector magnitude approaching zero while the largest possible vector magnitude for highly polarized colonoids was 0.5. For the conventional multiwell plate, the average EdU polarization vector possessed a length of  $0.009 \pm 0.064$  and an angle of  $61 \pm 26$  degrees. The colonoids in the microchannel displayed an average EdU polarization vector with a length of  $0.011 \pm 0.053$  and an angle of  $38 \pm 41$  degrees. As with the Sox9EGFP vectors, the EdU vector magnitudes suggested that in the absence of an external growth factor gradient the rapidly proliferating cells within a colonoid showed no spatial preference (Fig 3).

### **A Wnt-3a gradient is sufficient to polarize the stem/progenitor cell compartments**

We next sought to test whether formation of a gradient of Wnt-3a, a factor that supports stem cell maintenance, would promote the polarization of the stem/progenitor cell compartment when applied across a single colonoid. To test this, colonoids were loaded into the microchannel and Wnt-3a (75 ng/mL) was added to the source reservoir only. After 5 d of culture under the linear Wnt-3a gradient, the colonoid area, Sox9EGFP expression, and EdU incorporation were measured. The median DsRed area/colonoid in the microchannel device was  $14,096 \mu\text{m}^2$  per colonoid (S11 Fig). After 5 days in culture, the colonoid area under the Wnt-3a gradient was not statistically different from that without a gradient in either platform. The median integrated Sox9EGFP fluorescence per colonoid was 73,591 RFUs (S7 Table and S12 Fig). Similar to the DsRed fluorescence, the integrated Sox9EGFP fluorescence per colonoid was not statistically different from that of colonoids in the absence of a gradient. These data suggest that the colonoids under the Wnt-3a gradient possess similar numbers of

stem/progenitor cells as the colonoids cultured in the absence of a gradient. Although the total size and Sox9EGFP fluorescence per colonoid in the gradient and no-gradient conditions were similar, the distribution of stem or proliferating cells across the colonoid under these two conditions might be distinct. To assess this possibility, the average Sox9EGFP and EdU polarization vectors of the Wnt-3a-gradient-exposed colonoids after 5 d in culture was measured and compared to a no-gradient condition. Colonoids exposed to the Wnt-3a gradient possessed an average Sox9EGFP polarization vector magnitude of  $0.0044 \pm 0.0019$  and an angle of  $58 \pm 21$  degrees, both of which were statistically different from that of colonoids in the microchannel in the absence of a gradient ( $p < 0.05$ ). Of the 28 colonoids surveyed under the Wnt-3a gradient, 22 colonoids (79%) possessed Sox9EGFP polarization vectors facing the Wnt-3a source (Fig 4A and 4B). The larger Sox9EGFP vector magnitude also suggested that the colonoids were more polarized than that without a gradient. However, the average vector was well short of the highly-polarized value of 0.04 so that the colonoids were not under maximal polarization conditions. The presence of Sox9EGFP polarization in a colonoid was not related to its location in the microchannel (S13 Fig and S6 Table). Under the influence of the Wnt-3a gradient, the average EdU polarization vector possessed a length of  $0.02 \pm 0.06$  and an angle of  $41 \pm 39$  degrees. The EdU polarization vector of colonoids exposed to Wnt-3a gradient demonstrated that eleven of the colonoids (73%) polarized the EdU expressing cells toward the Wnt-3a source (Fig 4C and 4D). Thus the majority of the colonoids in the channel responded to the Wnt-3a gradient with their proliferating cells localized to colonoid regions with sufficient Wnt-pathway activation creating discrete stem/TA cell compartment similar to what is seen in

vivo at the base of the crypt. This data also demonstrates that a Wnt gradient alone is sufficient to polarize a colonoid in the absence of other signaling gradients such as BMP, Noggin, or R-spondin.

### **A Wnt-3a/R-spondin1 gradient enhances polarization of the stem/ progenitor cell compartment**

The highest levels of Wnt activity are thought to exist in the crypt base with the Wnt concentration tapering off in a gradient toward the luminal surface. R-spondin1 (Rspo1) is coexpressed with Wnts in the stem cell zone and functions to potentiate Wnt activity through its receptor LGR5, which is G-protein coupled receptor expressed almost exclusively in colonic stem cells<sup>113</sup>. To determine whether a dual gradient of Wnt-signaling along the microchannel might promote enhanced polarization of proliferative and differentiated cellular compartments, R-spondin1 and Wnt-3a were placed at high concentration in the source reservoir (75 ng/mL Wnt-3a, 110 ng/mL R-spondin1) to generate an environment with a steep factor gradient. After 5 days under a Wnt-3a/R-spondin1 gradient, the median DsRed fluorescence (area/colonoid) was 22,146  $\mu\text{m}^2$  and the median Sox9<sup>EGFP</sup> fluorescence (intensity/colonoid) in the presence of the dual gradient was 105,823 RFUs (S11 and S12 Figs and S8 Table). These values were not statistically different from that in the absence of a gradient or in the presence of a Wnt-3a gradient alone) suggesting that the number of stem/progenitor cells and differentiated cells were not changed in the presence of a Wnt-3a/R-spondin1 gradient. To assess whether a Wnt-3a/R-spondin1 gradient enhanced polarization of the stem/progenitor and differentiated compartments, Sox9<sup>EGFP</sup> and EdU location was measured in each colonoid under the dual factor gradient. The average Sox9<sup>EGFP</sup>

polarization vector exhibited a magnitude of  $0.0049 \pm 0.0019$  and an angle of  $35 \pm 31$  degrees, which was a statistically significant difference from that of the colonoids in the absence of a gradient, but not significantly different from that of a Wnt-3a gradient alone. Of the 24 colonoids assessed in the dual gradient, 92% possessed a Sox9EGFP vector that orientated toward the source reservoir containing Wnt-3a/R-spondin1 (Fig 5A and 5B). As with the Wnt-3a gradient, the presence of Sox9EGFP polarization in a colonoid was not related to its location in the microchannel (S13 Fig and S6 Table). Analysis of EdU labeling under the Wnt-3a/R-spondin1 gradient revealed an average EdU polarization vector magnitude of  $0.09 \pm 0.07$  and an angle of  $15 \pm 19$  degrees, which was a statistically significant difference from polarization vectors in the absence of a factor gradient or Wnt-3 alone (Fig 5C and 5D). Nearly all colonoids in the Wnt-3a/R-spondin1 gradient exhibited proliferating cells oriented toward the highest Wnt-3a/R-spondin1 concentrations similar to what is observed in vivo at the base of the crypt.

### **Effect of a Wnt-3a and R-spondin1 Gradient on Growth and Polarization of Colonoids Derived from a Single Stem Cell**

The experiments above utilized multicellular colonoid fragments as the source material for development of colonoids. While the fragments were small ( $\sim 30 \mu\text{m}$  diameter with  $\sim 25$  cells), the fragments did contain many cell types (differentiated, stem, and TA cells), and thus may have had pre-established cellular interactions that might impact spatial lineage allocation of a colonoid developing under an externally imposed growth-factor gradient. In addition, the colonoid fragments were obtained from continuously cultured colonoids ( $>1$  month). While all evidence to date indicates that the cells within these colonoids are representative of those in vivo and maintain a

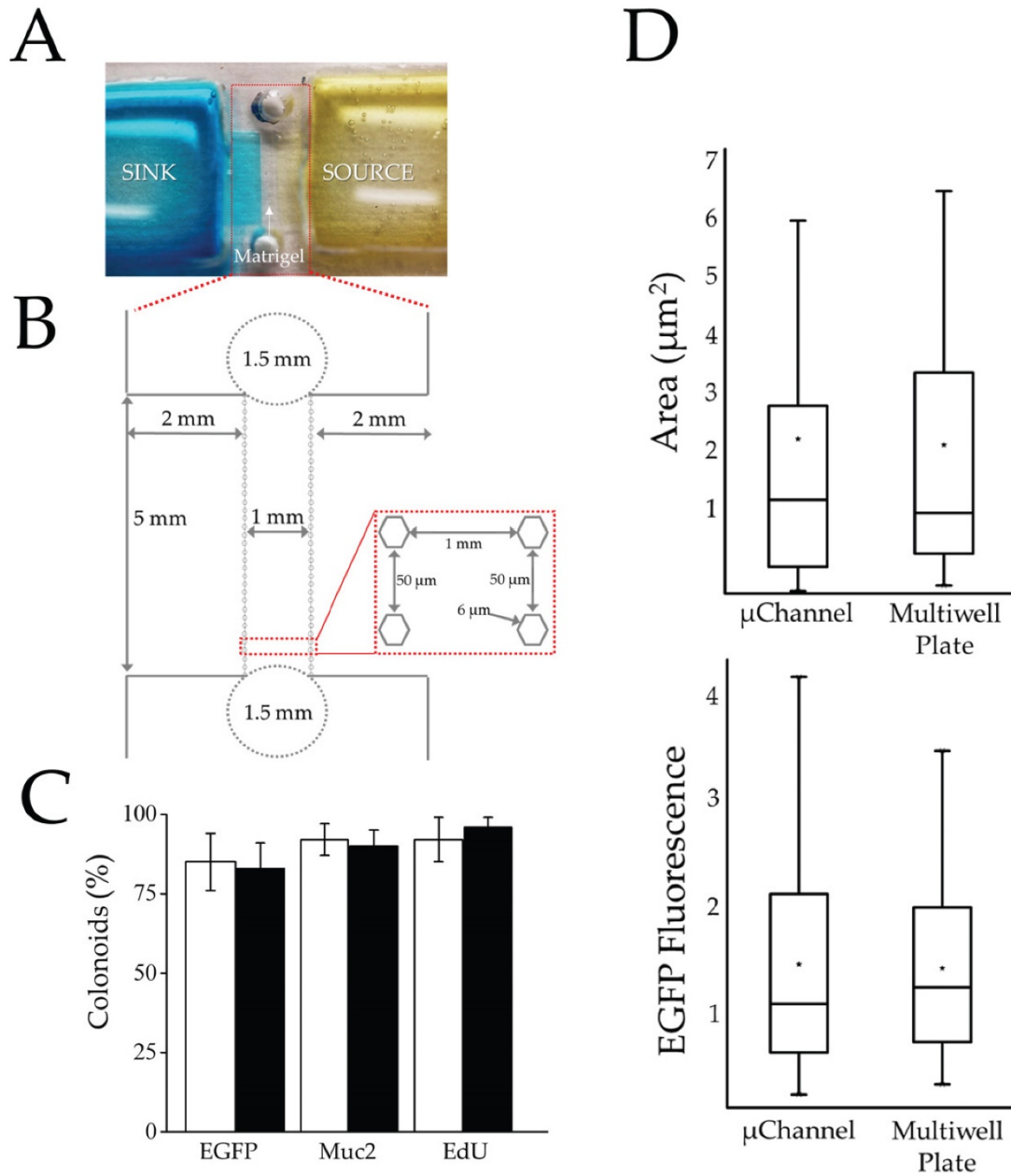
normal karyotype, it is conceivable that the cultured colonoids differ in an as yet unknown manner from their in vivo counterparts<sup>64,90,114</sup>. For this reason, single stem cells were isolated from freshly obtained Sox9<sup>EGFP</sup>-CAGDsRed mouse crypts by fluorescence-activated cell sorting of the stem cells (Sox9<sup>EGFP</sup><sub>low</sub>:CAG<sup>DsRED</sup>)<sup>115</sup>. The stem cells suspended in Matrigel were loaded into a microchannel and cultured for 5 d in the presence of a Wnt-3a/R-spondin1 gradient. The median DsRed fluorescence area per colonoid was 16,576  $\mu\text{m}^2$  so that the area of the 5-day colonoids in the dual gradient was not statistically different from that obtained in the prior experiments using multicellular colonoid fragments (S11 Fig). Similarly, the Sox9<sup>EGFP</sup> fluorescence/colonoid of the single stem cell-derived colonoids (median of 95,734 at 5 days) did not display a statistically significant difference from that of prior experiments (S12 Fig and S9 Table). These data suggested that colonoids originating from individual stem cells grew robustly, catching up in size and stem/TA cell numbers to that of the cultured colonoid fragments. The Sox9<sup>EGFP</sup> polarization vector for the single-cell-derived colonoids was measured to test the hypothesis that these colonoids might more readily polarize under the Wnt-3a/R-spondin1 gradient since the single cells were initially free of cell-cell interactions. The average Sox9<sup>EGFP</sup> polarization vector of the single-cell-derived colonoids possessed a magnitude of  $0.012 \pm 0.002$  and an angle of  $17 \pm 16$  degrees which was a statistically significant difference from that of colonoid-fragment-derived colonoids under a Wnt-3a/R-spondin1 gradient ( $p < 0.05$ ). Of the 23 colonoids surveyed in the dual gradient condition, 20 colonoids (87%) possessed Sox9<sup>EGFP</sup> vectors pointing in the direction of the growth factor source (Fig 6). A similar percentage of colonoids arising from the single cells and colonoid fragments polarized

to align with the growth factor gradient; however, colonoids developing from the single stem cells were more highly polarized as evidence by greater vector magnitudes than those arising from the colonoid fragments. In addition, colonoids located near the sink were more likely to be polarized than those located near the source (S14 Fig and S6 Table). The above data suggest that cell interactions within the colonoid fragments exert an additional influence on the behavior of the stem and/or TA cells modifying the colonoid's ability to fully spatially orient in response to environmental cues. The growth-factor gradient concentrations near the sink also appear more appropriate for that required to induce colonoid polarization.<sup>3,89,117,118,150,153–157</sup>

## **Conclusions**

Basal-luminal polarization of the stem/progenitor and differentiated cellular compartments in the intestinal and colonic crypts is considered to be dictated by gradients of morphogenic factors<sup>91,113</sup>. A number of studies indirectly demonstrate through gene expression assays that downstream targets of canonical Wnt signaling exist in a graded fashion along the crypt axis<sup>88,89</sup>. Formal testing of how specific growth factor or chemical gradients influence a number of biological processes like cellular differentiation and crypt patterning have been precluded by limitations in colonic stem cell culture and platforms that enable the generation of steep growth factor gradients. Here, we optimized a platform to introduce tightly controlled steep linear gradients of morphogenic factors, similar to those widely held to be present in vivo, across individual colonoids or single stem cells. We demonstrate that imposing a simple linear gradient of Wnt-3a/Rspondin1 is necessary and sufficient to induce polarization of the proliferative and differentiated cellular architecture in colonoid tissue constructs derived from both

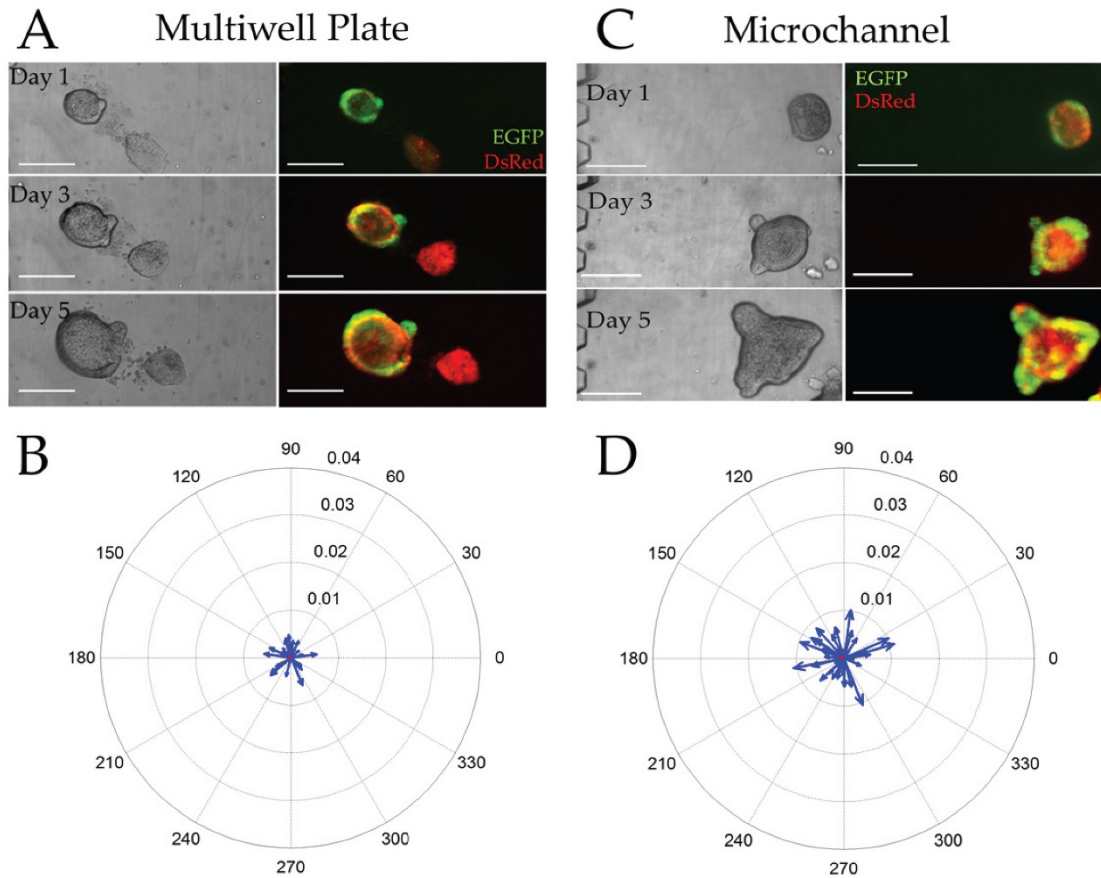
single colonic stem cells and small multicellular colonoids composed of heterogeneous cell types. In these studies, a stem and proliferative cell niche was recreated within a single epithelial unit by imposing a simple, linear, 2-factor gradient suggesting that in vivo, polarization of Wnt-signaling along the crypt axis is likely to be sufficient to maintain the basal-to-luminal crypt organization. Introduction of a 75 pg/mL/ $\mu$ m gradient of Wnt-3a resulted in polarized colonoids with localization of proliferative stem and TA cells in regions of higher Wnt-3a concentration paralleling the in vivo cellular patterning of the intestinal crypt. In this single gradient experiment, R-spondin1, also an activator of the Wnt signaling pathway, was at a uniform concentration of 90 ng/mL throughout the microchannel. It is possible that the R-spondin1 alone provided sufficient Wnt pathway activation to support the Sox9EGFP-expressing cells throughout the colonoids. A combined gradient of Wnt-3a (75 pg/mL/ $\mu$ m) and R-spondin1 (110 pg/mL/ $\mu$ m) acted synergistically to produce enhanced polarization of the colonoid body. The concentration drop over distance for these factor gradients was similar to those reported in the literature for other critical factors controlling a variety of biological processes and organismal development<sup>192–194</sup>. Maintenance of colonoids derived from single stem cells under the combined gradient condition produced the most highly polarized colonoid structure suggesting that the multicellular fragments possessed some internal patterning which limited the ability of colonoids derived from them to maximally respond to morphogenic gradients. These experimental results demonstrate for the first time that a simple linear gradient of growth factors is capable of directing polarization of the cellular architecture along the crypt axis.



**Appendix A: Fig 1. Characterization of the gradient-generating microdevice.**

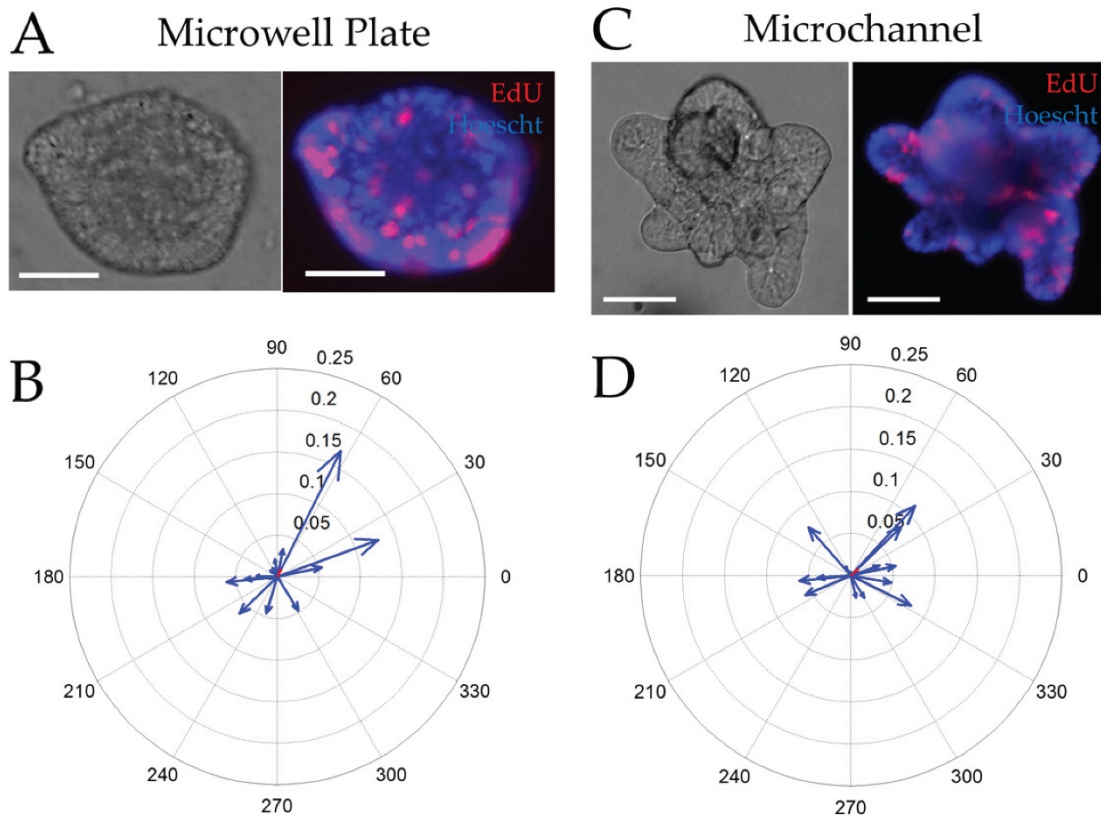
(A) Photograph of the device. The Matrigel-filled gradient region resides between the sink (left with blue dye) and source (right with yellow dye) reservoirs. (B) Schematic of the gradient generating microchannel of the device. The 1.5-mm diameter circles mark the ports for loading Matrigel into the central microchannel. (C) Histogram showing

percentages of colonoids possessing Sox9EGFP expression (stem/TA cell), exhibiting Muc2 staining (goblet cells) and labeling with EdU (actively proliferating cells) when cultured in the microchannel (black) or conventional multiwell plate (white). (D) Colonoid area (top) and Sox9EGFP fluorescence (bottom) per colonoid are shown after 5 days in culture in either the microchannel or microwell. Boxplots were used to represent the non-normal data distribution. Colonoid area is represented as  $\mu\text{m}^2$  (x 104) and Sox9EGFP fluorescence intensity is represented as RFUs (x 105). For the boxplots, the black star indicates the mean of the data, the bar shows the median, and the upper and lower boxes represent the 75% and 25% of the data, respectively. The whiskers extend to the 5% and 95% of the data.



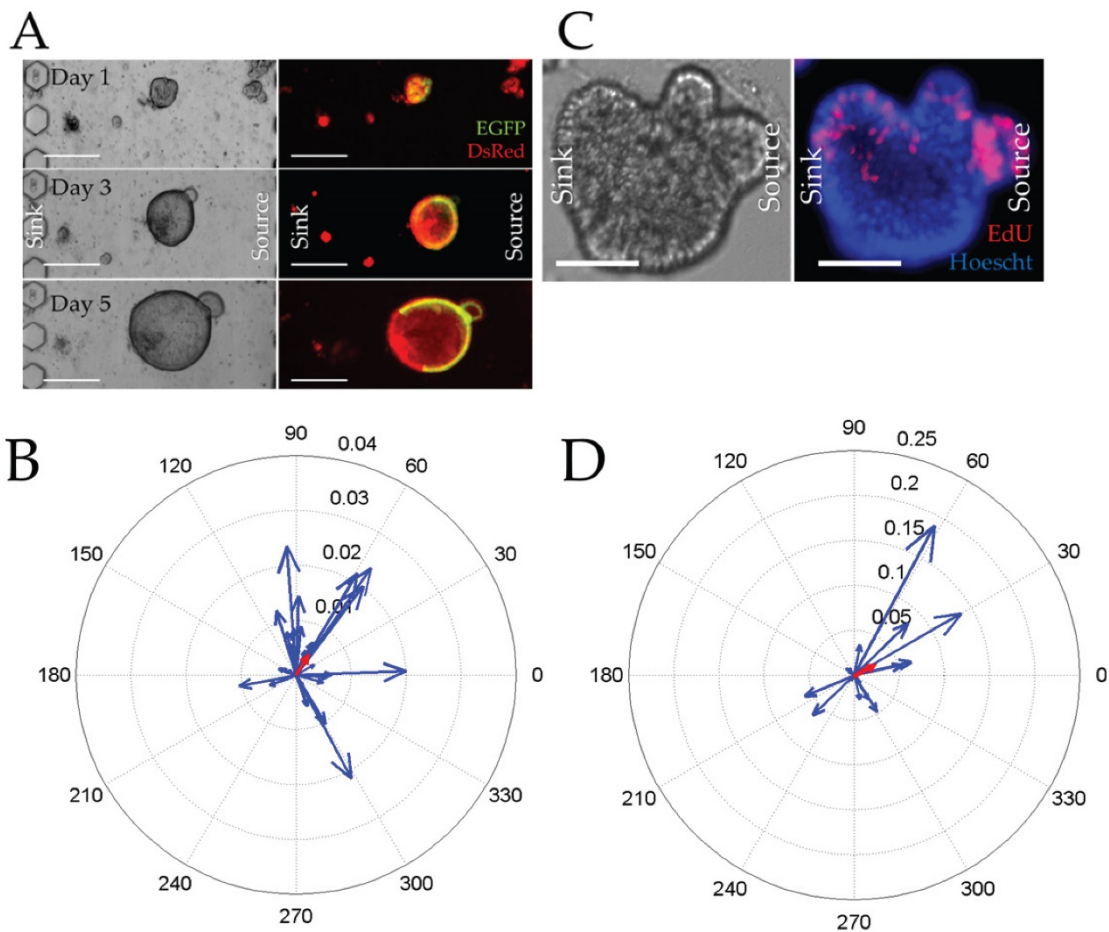
**Appendix A: Fig 2. Colonoid properties in the absence of a gradient.**

(A, C) Brightfield (left) and overlaid red/green fluorescence (right) images of colonoids cultured within a standard multiwell plate (A) or microchannel (C) for 1, 3, and 5 days. Scale bars represent 250  $\mu\text{m}$ . (B, D) Compass plots displaying the Sox9EGFP polarization magnitude and angle for individual colonoids cultured in the multiwell plate (B) or microchannel (C) for 5 days ( $n = 49$  colonoids in 10 microchannels and  $n = 30$  colonoids in 5 wells). The blue vectors represent individual colonoids while the average magnitude and angle of the vector is marked in red (poorly visualized due to the near-zero magnitude).



**Appendix A: Fig 3. Incorporation of EdU into colonoids after a 2 h pulse in the absence of a gradient.**

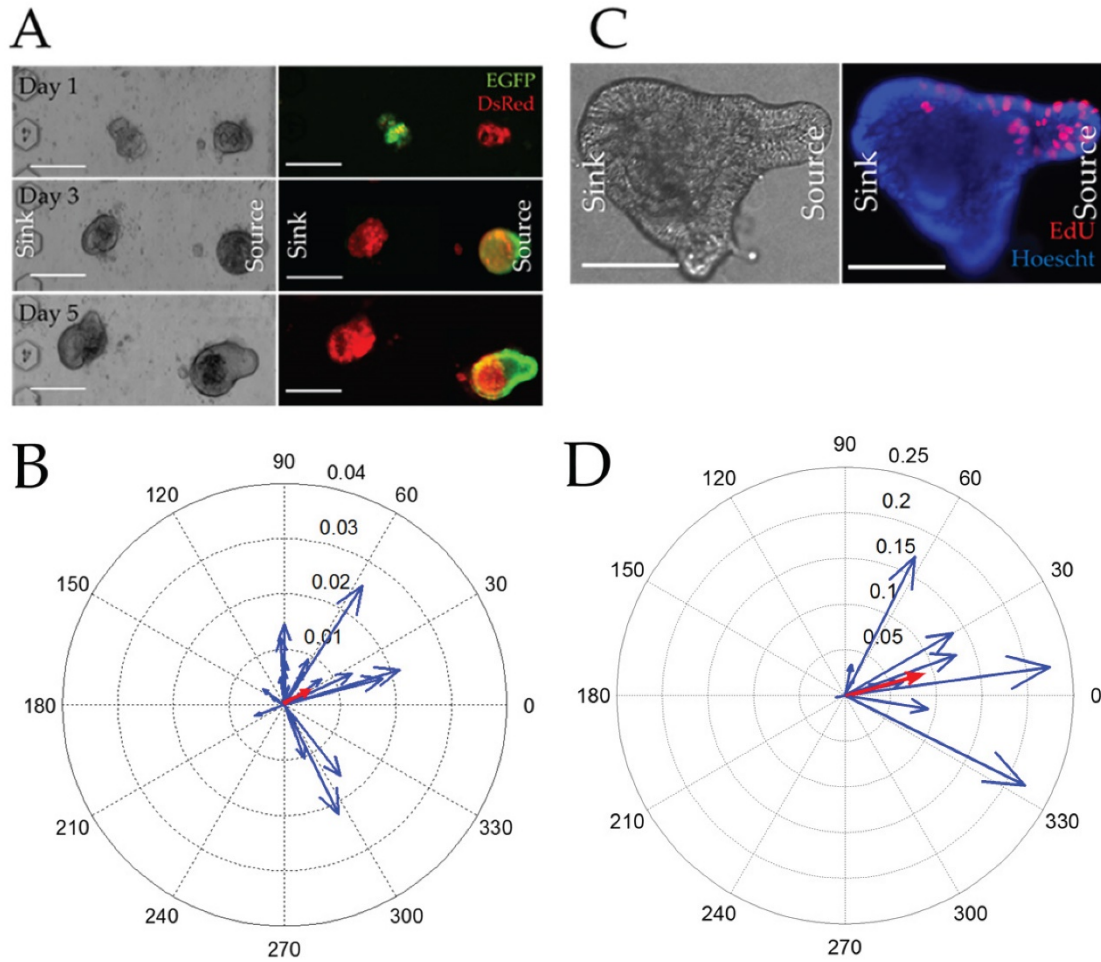
(A,C) Brightfield (left) and overlaid red/blue fluorescence (right) images of colonoids cultured within a multiwell plate (A) or microchannel (C) for 5 days then labeled with EdU (red) and the Hoechst 33342 (blue) (n = 18 colonoids in 5 microchannels and n = 16 colonoids in 3 multiwells). Scale bars represent 50  $\mu\text{m}$ . (B, D) Compass plots displaying the EDU polarization magnitude and angle for individual colonoids (blue) cultured in the multiwell plate (B) or microchannel (C) for 5 days and pulsed with EdU. The average magnitude and angle of the vector can be seen in red (poorly visualized due to the near-zero magnitude).



**Appendix A: Fig 4. Colonoid growth in the presence of a Wnt-3a gradient across the microchannel.**

(A) Brightfield (left) and overlaid red/green fluorescence (right) images of colonoids cultured under a Wnt-3a gradient for 1, 3, and 5 d. The scale bar is 250  $\mu\text{m}$ . (B) Compass plot displaying the Sox9EGFP polarization magnitude and angle for individual colonoids cultured under the Wnt-3a gradient for 5 days (n = 28 colonoids on 5 devices). The average magnitude and angle of the vector can be seen in red. (C) Brightfield (left) and overlaid red/blue fluorescence (right) images of colonoids cultured under a Wnt-3a gradient for 5 days then pulse-labeled with EdU (red) for 2 h. Hoechst

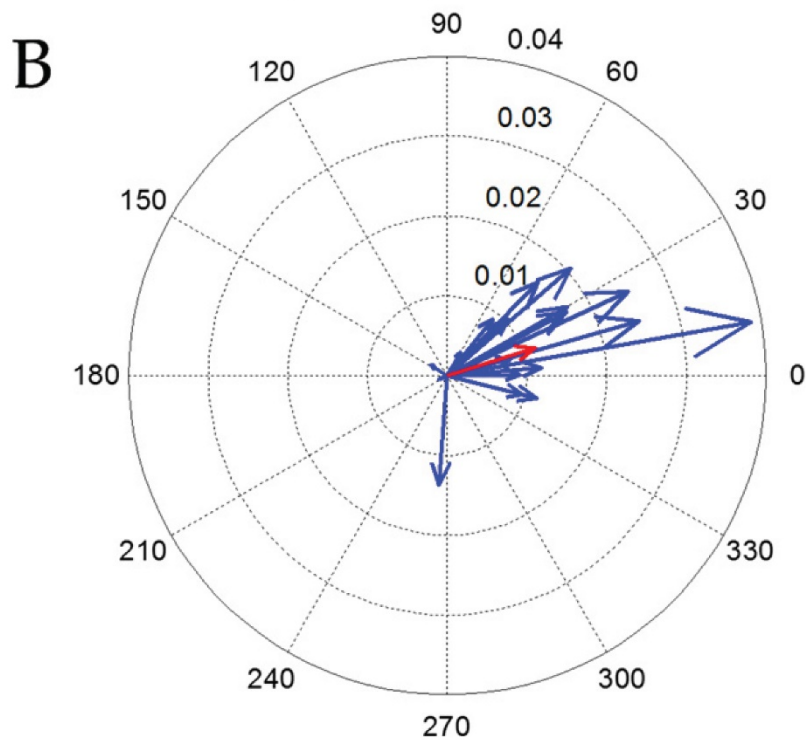
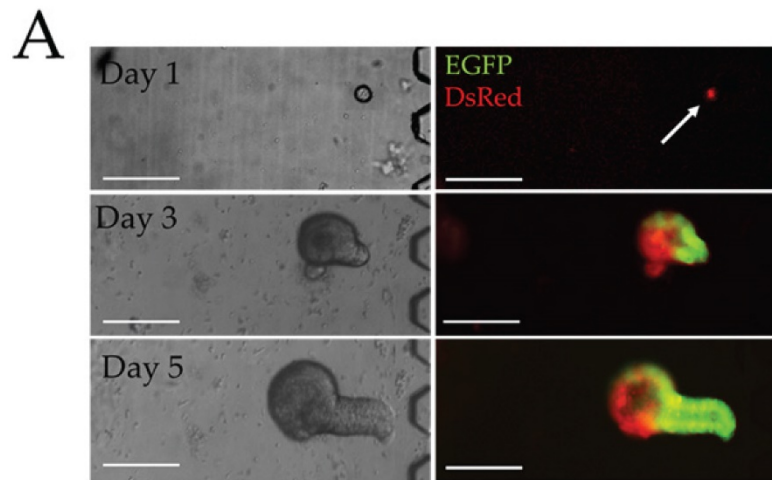
33342 fluorescence is shown in blue. The scale bar represents 50  $\mu\text{m}$ . (D) Compass plot displaying the EDU polarization magnitude and angle for individual colonoids (blue) cultured as described in (C) (15 colonoids in 5 microchannels). The average magnitude and angle of the vector can be seen in red.



**Appendix A: Fig 5. Colonoid growth in the presence of a dual Wnt-3a/R-spondin1 gradient.**

(A) Brightfield (left) and overlaid red/green fluorescence (right) images of colonoids cultured under a Wnt-3a/R-spondin1 gradient for 1, 3, and 5 days in the microchannel. The scale bar is 250  $\mu$ m. (B) Compass plot displaying the Sox9EGFP polarization magnitude and angle for individual colonoids (blue) cultured under the Wnt-3a/R-spondin1 gradient for 5 days (n = 33 colonoids from 6 microchannels). The average magnitude and angle of the vector can be seen in red. (C) Brightfield (left) and overlaid red/blue fluorescence (right) images of colonoids cultured the gradient for 5 days then

pulse-labeled with EdU (red) for 2 h. Hoechst 33342 fluorescence is shown in blue. The scale bar represents 50  $\mu\text{m}$ . (D) Compass plot displaying the EDU polarization magnitude and angle for individual colonoids (blue) cultured as described in (C) ( $n = 11$  colonoids in 4 microchannels). The average magnitude and angle of the vector can be seen in red.



**Appendix A: Fig 6. Growth of single stem cells in the presence of a Wnt-3a/R-spondin1 gradient.**

(A) Brightfield (left) and overlaid red/green fluorescence (right) images of single stem cells cultured under a Wnt-3a/R-spondin1 gradient for 1, 3, and 5 days in the microchannel. The scale bar is 250  $\mu\text{m}$ . (B) Compass plot displaying the Sox9EGFP

polarization magnitude and angle for the single colonoids (blue) under the Wnt-3a/R-spondin1 gradient for 5 days (n = 23 colonoids in 5 microchannels). The average magnitude and angle of the vector can be seen in red.

## **Appendix B: Self-renewing Monolayer of Primary Colonic or Rectal Epithelial Cells**

### **Introduction**

Long-term culture of primary intestinal epithelial tissue as a planar monolayer has not been possible due to the rapid loss of stem and proliferative cells and rapid onset of apoptosis when primary epithelium is placed into culture.<sup>61</sup> Investigators have traditionally relied on colon cancer cell lines, like Caco-2 and its derivatives, to study gut epithelial physiology because of their ability to grow indefinitely on conventional tissue culture plates.<sup>195</sup> While cancer cell lines grow as confluent monolayers and can be efficiently passaged, they possess many non-physiologic characteristics including somatic mutations, chromosomal instabilities, altered metabolism, and aberrant proliferative and differentiation characteristics.<sup>196</sup> Together, these non-physiologic properties of Caco-2 cells call into question their predictive ability in assays designed to understand normal epithelial physiology.

Recent advances in epithelial culture conditions now promote intestinal stem cell (ISC) maintenance and indefinite culture of primary intestinal tissue as 3D organoids.<sup>197–201</sup> The organoid culture system utilizes soluble growth factors including Wnt-3A, R-spondin, Noggin and epidermal growth factor (EGF) to mimic the ISC niche environment that support ISC survival, growth, and differentiation in a thick layer of Matrigel.<sup>197,200,202,203</sup> Like *in vivo*, organoid ISCs exhibit their defining properties by self-renewing and giving rise to progenitors that differentiate into absorptive colonocytes (water and

electrolyte uptake), goblet cells (mucus production), enteroendocrine cells (hormones), and Paneth cells (antimicrobial and stem cell niche functions).<sup>197</sup> By virtue of their non-transformed condition, 3D organoids represent a physiologically relevant model enabling novel assays and pharmaceutical and dietary compounds screens that are not currently possible with colon cancer cell lines, such as Caco-2.<sup>196,204</sup>

While organoid culture technology has had a major positive impact on the *in vitro* study of primary gut epithelium, the 3D geometry of organoids prevents access to the apical aspect of the epithelium producing a number of challenges to physiologically relevant studies. The apical surface of the organoid is analogous to the lumen of the gut where digested contents and microbial communities interact with the epithelium. The spheroidal architecture of the organoids prevents access of exogenous compounds to the luminal epithelial surface limiting studies focused on apical transporters, receptors, metabolic enzymes, and microbiota.<sup>205</sup> Matrigel embedded organoids exist in multiple planes making collection of experimental readout using conventional microscopy exceptionally challenging.<sup>206,207</sup> Unfolding the spherical organoid into a 2D planar tissue construct is a solution that addresses these major challenges and has the potential to further transform *in vitro* study of the gut epithelium.

We have previously demonstrated that primary intestinal epithelial cells can be cultured on polydimethylsiloxane (PDMS) and other artificial surfaces in the absence of a hydrogel.<sup>206</sup> Although supplied with the requisite soluble growth factors for growth within Matrigel, culture of primary epithelium on non-hydrogel surfaces produced a short-lived, non-proliferative monolayer of cells. Dissociated 3D small intestinal and colonic organoids have been cultured on a porous membrane (coated with 0.1% gelatin or 10

$\mu\text{g}/\text{cm}^2$  collagen) to form a monolayer, but these monolayers were not self-renewing suggesting that stem cells were lost from the monolayers over time and a self-renewing ISC compartment was not supported.<sup>208,209</sup> The failure of existing 2D culture methods to produce long-term monolayers suggests that a biochemical environment composed of media and soluble growth factors alone is not adequate to sustain a self-renewing monolayer containing both stem and differentiated cells. To overcome the limitations in monolayer culture duration, we sought to identify parameters that would support self-sustaining monolayers.

## **Materials and Methods**

### **Isolation of crypts from mouse colon and human rectal biopsies.**

Male mice were used at age 6-10 weeks. All experiments were performed in compliance with the relevant laws and institutional guidelines at the University of North Carolina. All experiments and animal usage was approved by the Institutional Animal Care and Use Committee (IACUC) at UNC. Mice were humanely euthanized by lethal dose of isoflurane followed by cervical dislocation under the approved UNC IACUC-approved protocol #13-200. A CAG-DsRed mouse model (CAG = CMV enhancer plus chicken actin promoter) in which all cells expressed the DsRed fluorescent protein was used to monitor the proliferation of colonic epithelial cells by fluorescence microscopy. CAG-DsRed heterozygous mice were bred on a CD-1 background and wild-type mice were bred on a C57BL/6 background. Wild type mice were used for fluorescence-based assays and compound screens. An Lgr5EGFPCreERT2xR26 confetti mouse was used for lineage tracing experiments on the 2D monolayer. The confetti mouse was injected

with 5 mg tamoxifen at 48 h before sacrifice and isolation of crypts from the large intestine.<sup>210</sup> Human rectal biopsies were obtained from UNC Hospitals Meadowmont Endoscopy Center with consent of the patient (under the approved UNC IRB #14-2013).

Isolation buffer was comprised of 5.6 mM Na<sub>2</sub>HPO<sub>4</sub> (Sigma S7907), 8.0 mM KH<sub>2</sub>PO<sub>4</sub> (Sigma P5655), 96.2 mM NaCl (Sigma S5886), 1.6 mM KCl (Sigma P5405), 43.4 mM sucrose (Fisher BP220-1), and 54.9 mM D-sorbitol (Fisher BP439-500) in deionized water. The buffer was filter sterilized and stored at 4°C. EDTA (2 mM, ThermoFisher 15575020) and DL-dithiothreitol (DTT, 0.5 mM, ThermoFisher R0861) were added to 10 mL of isolation buffer and used within 2 hours. Colon tissue was incubated in the above EDTA/DTT solution at room temperature for 75 minutes. The tissue was then rinsed with 5 mL of isolation buffer twice, and vigorously shaken by hand in 10 mL isolation buffer to release the crypts. The density of crypts in the solution was obtained by adding a 10 µL suspension to a Petri dish and counting the number of crypts in this drop of suspension. Released crypts were placed into culture within 30 min of isolation. Isolated crypts were placed on the top of the collagen hydrogel at a density of 1,000 crypts/cm<sup>2</sup> and cultured in 4 mL of medium in the 6-well plate. The medium was changed every 48 h.

### **Preparation of the collagen hydrogel in a 6-well plate.**

Collagen hydrogel is generally prepared by neutralizing the acidic collagen solution with NaOH and incubating the mixture at 37°C for 30-60 minutes. The hydrogel properties (e.g. stiffness, clarity, adhesiveness, cell-binding sites) are highly dependent on the pH during gelation. Therefore, we used a customized neutralization buffer

(containing HEPES, NaHCO<sub>3</sub> and NaOH in PBS) to neutralize the acidic collagen solution prior to gelation to ensure a final pH of 7.4 for the hydrogel. The neutralization buffer was prepared in 75 mL volumes and the reagents and their catalog numbers are listed in detail in the Supporting Information. To prepare 1 mL neutralized collagen at a concentration of 1 mg/mL, 750  $\mu$ L neutralization buffer was first added to a 15-mL conical tube, and the tube was placed on ice. Then 250  $\mu$ L collagen stock solution (type I, rat tail, Corning 356236, 4 mg/mL, 4°C) was added to the tube, and the mixture was homogenized by slow and repeated pipetting, carefully avoiding air bubble formation during pipetting. The collagen mixture (1 mL) was added to each well of a 6-well plate (Denville T1006). The plate was incubated at 37°C for 1 h to generate a clear hydrogel. PBS (4 mL) was placed over the hydrogel. The collagen hydrogel was generally used within two hours after preparation, but could be stored in a 37°C incubator up to one month without apparent loss of integrity, adhesion and cell culture outcome. The thickness of the collagen hydrogel was 1 mm in the 6-well plates.

## **2D monolayer culture on a collagen hydrogel.**

The crypts were placed on top of the collagen hydrogel at a density of 1,000 crypts/cm<sup>2</sup> (unless otherwise stated) and cultured in medium (4 mL per well in the 6-well plate, and medium formulation is defined in the Supporting Information). The medium was changed every 48 h, and Y-27632 was added for the initial 48 h of culture. When the cell coverage was greater than 80% (typically after 3-4 days for mouse cells, 5-7 days for human cells), the monolayers were sub-cultured by a gentle two-step dissociation method. The first step was to lift up the monolayer from the collagen hydrogel by scrapping the collagen (with cells) from the well, and transferring the

hydrogel to a 15-mL conical tube containing 1 mL of culture medium with 500 U/mL of collagenase (type IV, Worthington Biochemical LS004189). The gel was broken into small pieces by pipetting using a 5 mL serological pipette followed by a 1 mL pipet tip. The tube was then incubated at 37°C for 10 min to completely digest the collagen gel. The monolayers were rinsed with PBS buffer, and pelleted by centrifugation at 600xg for 1 min. The second step was to further breakup the monolayer pieces into smaller fragments by incubating the pellet in 150 µL of EDTA (0.5 mM) and Y-27632 (10 µM) in PBS at 37°C for 2 min (mouse cells) or 5 min (human cells). The monolayers were broken into small fragments by pipetting up and down 30 times using a 200 µL pipet tip. The cell fragments were re-suspended in medium and sub-cultured on a new collagen hydrogel at a passage ratio of 1:3.

To convert 3D organoids to a 2D monolayer, the organoids were extracted from Matrigel by detaching the Matrigel patty, breaking it into coarse pieces and then pipetting the suspension using a 200 µL pipet tip. The cells were then cultured on a collagen gel at a density of 10 organoids/cm<sup>2</sup>.

### **Characterization of the 2D monolayer.**

The proliferation and viability of cells was either quantified by surface area coverage or a cell viability assay (CellTiter-Glo luminescence assay, Promega G7572). To ensure the cells possessed grossly normal chromosomes, cells were karyotyped (KaryoLogic, Inc). Twenty cells from each sample were analyzed. To reveal the topographic features of 2D monolayer, the samples were dried with a critical point dryer (Tousimis Semidri PVT-3) and inspected by scanning electron microscope (SEM, FEI

Quanta 200 ESEM, FEI Company). For immunofluorescence (IF) staining, thin sections (8–10  $\mu\text{m}$ ) of the 2D monolayers were prepared on a cryostat.

### **High-throughput screening of dietary metabolites and natural products.**

All 77 compounds were obtained from Sigma Aldrich. The names, categories and their working concentration are listed in supplementary Table 2. 75  $\mu\text{L}$  collagen hydrogel was prepared in each well of 96-well plates (Corning #3603) by the protocol described above. Fragments of primary mouse colonic epithelial cells (75,000 cells per well) were cultured on the collagen hydrogel with 200  $\mu\text{L}$  ENR-W (with “W” indicating a normal [Wnt-3A] of 30 ng/mL). At 24 h, the medium was aspirated, and the cells were cultured in medium (200  $\mu\text{L}$ ) containing a dietary/natural compound in ENR-w (with “w” indicating a reduced [Wnt-3A] of 10 ng/mL) for an additional 48 h. The decreased Wnt-3A concentration reduced the Wnt-3A signaling strength enabling cells to undergo differentiation in response to exogenous compounds. The cells were pulsed with 5-ethynyl-2-deoxyuridine (EDU) (3 h), stained for ALKALINE PHOSPHATASE (ALP) (30 min), and then fixed with 4% paraformaldehyde (15 min). The cells were then sequentially labeled with the Click-iT EDU reagent,  $\alpha$ -Muc2 (MUCIN2) and Hoechst 33342. Finally, the cells were thoroughly rinsed with PBS to remove excess reagents. Three 96-well plates were used for each experiment.

### **Assaying for hit dietary compounds on mouse 3D organoids and human 2D monolayers.**

14 selected hit compounds were tested on 3D mouse colonic organoids. Fragments of mouse colonic epithelial cells (25,000 cells per well) were embedded in 4  $\mu\text{L}$  Matrigel in each well of a 96-well plate and cultured with ENR-W (200  $\mu\text{L}$ ). At 24 h,

the medium was aspirated, and the cells were cultured in ENR-w (200  $\mu$ L) containing a dietary/natural compound for an additional 48 h. Seven selected hit compounds were tested on human rectal 2D monolayers. Fragments of human rectal epithelial cells (75,000 cells per well) were cultured on the collagen hydrogel in a 96-well plate with Human Intestinal Stem Cell medium (HISC) with high [Wnt-3A] of 100 ng/mL. At 48 h, the medium was aspirated, and the cells were cultured in medium (200  $\mu$ L) containing a dietary/natural compound in HISC medium with reduced [Wnt-3A] of 30 ng/mL for an additional 96 h. The cells were then stained with ALP, EDU,  $\alpha$ -Muc2 and Hoechst 33342 in the same manner as the mouse 2D monolayers described above.

### **Image Acquisition.**

Following staining, each 96-well plate was imaged using an Olympus IX81 epifluorescence microscope (4 $\times$  objective, N.A. of 0.13, Olympus UPlanFL N). The imaging area consisted of a grid of either 4 $\times$ 3 or 6 $\times$ 4 overlapping images covering 47%-54% of the total well area. Well-focused images covering the entire image area were obtained by autofocusing on each image position using a custom script written in MatLab. Each sample was imaged using blue, red, far red, and green filter sets (Chroma ET-DAPI 49000, Semrock TxRed-4040B, Chroma ET-Cy5 49006, and Semrock FITC-3540B, corresponding to the Hoechst 33342, ALP, EDU, and Muc2 stains, respectively) and an exposure time of 150 ms for all channels. The total image acquisition time for a 96-well plate using a 6 $\times$ 4 image grid for each well was 456 $\pm$ 7.5 min.

## **Image Analysis.**

After cropping out the overlapping regions in the image data, the collected images obtained from each well were filtered using a Wiener filter with a 3×3 pixel neighborhood to reduce noise. The image background was subtracted using top-hat filtering, and then the images were empirically thresholded. Objects smaller than 3.1 μm in diameter were removed to eliminate cellular debris and artifacts produced by camera noise. The integrated raw fluorescence intensity over the area occupied by the supra-threshold fluorescence was summed for all images of a sample and for each fluorescence emission wavelength. This summed fluorescence area was then normalized by the total cell area occupied by the Hoechst 33342 fluorescence and plotted against the compound number.

## **Hit Selection.**

In high-throughput screens it is important to assess how much the test compounds and negative controls differ from one another. Strictly standardized mean difference (SSMD) was used to quantify the differences between the dietary compounds and negative controls.<sup>211</sup> SSMD is commonly used statistic in compound screens and is calculated as the mean difference between the test sample and reference sample divided by the standard deviation of the difference between the test and reference. SSMD essentially measures effect size for the comparison of two groups. Sample #78 was used as the negative reference for SSMD calculations for all tissue types. Compound effects were classified using standard SSMD thresholds:<sup>212</sup>  $|\text{SSMD}| \geq 5$  for extremely strong,  $5 > |\text{SSMD}| \geq 3$  for very strong,  $3 > |\text{SSMD}| \geq 2$  for strong,  $2 > |\text{SSMD}| \geq 1.645$  for fairly strong,  $1.645 > |\text{SSMD}| \geq 1.28$  for moderate,  $1.28 > |\text{SSMD}| \geq 1$  for

fairly moderate,  $1 > |\text{SSMD}| \geq 0.75$  for fairly weak,  $0.75 > |\text{SSMD}| \geq 0.5$  for weak,  $0.5 > |\text{SSMD}| \geq 0.25$  for very weak, and  $|\text{SSMD}| \leq 0.25$  for extremely weak effects. Compounds with “fairly strong” or stronger effects on nuclear coverage, ALP signal, or EDU signal were designated hits. Compounds with only “fairly moderate” or stronger effects on Muc2 signal were designated hits due to the weaker effects apparent across all Muc2 screens. Library screens were performed in triplicate across well plates (mouse and Caco-2 monolayers). The SSMD size effect was calculated using the paired uniformly minimal variance unbiased estimate (UMVUE) of SSMD.<sup>213</sup> Library screens performed in triplicate within single wells plates (human 2D monolayers and mouse 3D organoids) and the SSMD size effect was calculated using the unpaired SSMD under unequal variance.<sup>211</sup>

#### **Other Statistics/Methods.**

Unless otherwise specified, the data shown for each experiment utilized crypts or cells obtained from a single mouse or one human biopsy. All data utilized three technical replicates ( $n=3$ ) and the mean with a single standard deviation is shown unless otherwise specified. When the fate of a crypt was assayed,  $n=3$  wells with 10 crypts/well counted. Multiple experiments from different mice for all data (except the dietary compound screen) were performed and the results were consistent over time without outliers. While the data of each experiment represent that of a single mouse (to reduce animal usage), over 30 mice were used throughout the work with no observable difference in monolayer formation or growth rate. This translates into greater than 30 different cell lines, but each typically used for no more than 5 passages to avoid any possibility of chromosomal aberrations. Animals from two different backgrounds were

used, CD-1 background (CAG-DsRed mice) and C57BL/6 background (Lgr5EGFPCreERT2xR26 and wild type mice). Data from representative experiments are presented. Biopsies from 3 different humans were used to develop the human monolayer system. The biopsies were obtained sequentially with the first 2 biopsies used to optimize the conditions for human cell culture. The data in the paper are from the 3<sup>rd</sup> biopsy specimen. No difference was observed in the properties of the cells from the different biopsies, and the optimized conditions for the first 2 biopsy cells worked well for the 3<sup>rd</sup> specimen.

## **Results**

### **A murine colonic epithelial monolayer proliferates on the surface of a collagen hydrogel**

Intestinal stem cells can be maintained as a proliferative culture by providing a media rich in growth factors and embedding the cells within Matrigel to form 3D organoids.<sup>7</sup> We hypothesized that a 2D monolayer of epithelial cells would undergo long-term proliferation if provided with the appropriate matrix cues such as a suitable stiffness in addition to the required soluble factors (Figure 1a). Matrigel is widely used in 3D stem cell culture systems as it resembles the extracellular matrix (ECM) found in many tissues.<sup>7</sup> Crypts cultured on the surface of Matrigel failed to form a spreading 2D monolayer (supplementary Figure 1b). Instead the crypts grew into 3D organoids residing above the surface ( $100 \pm 0\%$  of crypts, 100 crypts counted per well, n=3) and possessed morphologies reminiscent of the organoids formed within a Matrigel patty, suggesting that Matrigel did not possess the ECM contacts and stiffness (Young's

modulus  $\sim 50 \text{ Pa}^{214}$ ) required to allow cells to spread on the surface (supplementary Figure 1a).

Polystyrene is the most commonly used 2D cell culture substrate,<sup>215</sup> and PDMS is a dominant material in building cell-based lab-on-chip and microfluidic devices.<sup>216</sup> Crypts plated on a bare, plasma-oxidized polystyrene or PDMS formed an adherent 2D monolayer, but the cells were short-lived and without evidence of self-renewal (supplementary Figure 1b). Similar outcomes were also observed for crypts plated on gelatin, agarose, and polyacrylamide (supplementary Figure 1d).

The common practice of coating surfaces with ECM proteins or peptides (Matrigel, collagen, laminin, fibronectin, gelatin, vitronectin, or poly-D-lysine) on plasma-oxidized polystyrene or PDMS did not improve the proliferative capability or viability of cells (supplementary Figure 1d), suggesting these materials lacked the softness (Young's modulus of PDMS = 0.8-4 MPa,<sup>217</sup> polystyrene = 3-3.5 GPa<sup>218</sup>) or other biophysical and biochemical properties that promote a self-sustaining monolayer.

Collagen hydrogels are widely used matrices for cell culture.<sup>219</sup> After crypts were plated on the surface of collagen hydrogel (type I, rat tail, 1 mg/mL, 1 mm thickness),  $93 \pm 6\%$  crypts formed a surface-attached monolayer that expanded in area and cell number over time (Figure 1b). Collagenase was highly effective at liberating, disaggregating and sub-culturing cells grown on the hydrogels (Figure 1c,d). Karyotyping demonstrated that cells retained the appropriate number of chromosomes through passage number 5 (supplementary Figure 2). Monolayers grew to sizes  $>2 \text{ mm}$  in diameter (Figure 1d) and were maintained in monolayer form for up to ten months (the longest time tested). Lower concentrations of collagen or collagen/Matrigel

composites did not support monolayer formation (supplementary Figure 1c,e) possibly due to inappropriate stiffness and ECM properties.

Monolayers were subjected to a number of morphological and protein expression analyses to characterize key epithelial properties found *in vivo*. When examined by electron microscopy, the cells of the self-sustaining monolayers demonstrated the hallmark "cobblestone" arrangement of colonic epithelium (Figure 1e). *In vivo*, large numbers of microvilli cover the surface of the differentiated colonocytes and function to increase surface area for water and salt absorption. On the monolayers, the microvilli density on each cell was variable suggesting that cells might be at different states of differentiation (Figure 1e,g). High densities of ACTIN and VILLIN, which are concentrated within microvilli, were present only on the upper or apical cell surface (Figure 1f,h,i). In contrast, INTEGRIN- $\beta$ 4 and  $\text{NA}^+/\text{K}^+$ -ATPASE were localized to the basal and basolateral cell surfaces, respectively, demonstrating that the cells are polarized with the luminal surface exposed to the medium and the basal surface facing the collagen (Figure 1i). Adherens and tight junctions were present between the cells of the monolayer as demonstrated by the localized ZO-1, E-CADHERIN and OCCLUDIN staining (Figure 1i). These results suggested that the collagen hydrogel supported epithelial monolayer development closely mimicking that *in vivo*, and also suggest that porosity, ECM proteins, and stiffness of the collagen hydrogel functionally recapitulated key properties of the native colonic basement membrane.

## Equivalency of murine colonic 2D monolayers to 3D organoids

Intestinal and colonic organoids embedded within Matrigel possess proliferative and differentiated cellular compartments and are widely accepted as an *in vitro* tissue model for the digestive tract.<sup>200</sup> Therefore, we sought to compare proliferative capacity and lineage composition between the murine 2D monolayer and 3D organoid platforms. Colonic crypts were cultured in 3D (embedded inside Matrigel patty) to form organoids, and in 2D (on the surface of a collagen hydrogel) to form epithelial monolayers (Figure 2a). Cell populations in both culture systems rapidly expanded with the monolayer and organoid cells demonstrating average doubling times of 23.7 hours (95% confidence interval [C.I.] bounds of 21.3 hours and 26.7 hours, n=4 technical replicates) and 31.2 hours (95% C.I. bounds of 25.1 hours and 41.0 hours), respectively (Figure 2b,c). We observed S-phase cells (EDU<sup>+</sup>) at day 3 in both 3D organoids and 2D monolayers demonstrating actively proliferating cells indicating the presence of stem and progenitor cell lineages (Figure 2d,e). The numbers of organoids and monolayer patches with differentiated cell types (Muc2<sup>+</sup> [goblet cells] and ChgA<sup>+</sup> [enteroendocrine cells]) was also equivalent in the two culture systems suggesting that the 3D and 2D platforms are functionally similar with respect to differentiated secretory lineages (Figure 2d,e). Cells derived from dissociated monolayers were capable of generating organoids when placed into 3D culture conditions (supplementary Figure 3). Similarly, crypt-derived organoids could be removed from 3D culture and cultured on the surface of a collagen hydrogel to form a 2D epithelial monolayer. There was no distinguishable difference between monolayers derived from freshly isolated crypts or from 3D cultured organoids (supplementary Figure 3a,b). Serial interconversion between the monolayer and

organoid morphologies were possible for at least five passages (the greatest number tested) indicating that colonic stem cells are maintained in the monolayer (supplementary Figure 3c,d). These data demonstrate that a proliferative monolayer can be derived from multiple sources (crypts, 3D organoids, and 2D monolayer fragments).

Mature organoids self-pattern into proliferative and differentiated zones by segregating a high density of stem and progenitor cells to the crypt buds (Figure 2f).<sup>220</sup> While stem cells are self-renewing and persist in the organoid crypt buds, differentiated cells in the organoid have a limited life span and are eventually sloughed into the central pseudolumen. Spontaneous patterning of proliferative and differentiated cellular compartments was also observed within the monolayers after 8 days in culture (Figure 2f). Proliferative cells (EDU<sup>+</sup>) were enriched along the edges of the expanding monolayer while differentiated cells such as goblet cells were concentrated in the center of the monolayer. These data demonstrate that monolayer and organoid culture systems readily interconvert, and are equivalent in terms of the cell proliferative capacity, lineage composition, and spontaneous compartmentalization of stem/proliferative cells and differentiated cells.

### **Lineage tracing confirms the presence of stem cells in the murine 2D monolayer**

To determine whether self-renewing colonic stem cells persisted in the 2D monolayers, we performed lineage tracing using the Lgr5EGFPCreERT2xR26 transgenic mouse. Colonic crypts were isolated from a tamoxifen-treated Lgr5EGFPCreERT2xR26 confetti mouse and plated on the surface of collagen hydrogel at a low density of 30 crypts/cm<sup>2</sup> (in order to track the growth of individual crypts). At 24 h post-plating, tracing events (4 out of 3,000 crypts) expressed red fluorescent protein

(RFP), which marked them as derived from Lgr5 stem cells (Figure 3a). The RFP<sup>+</sup> regions expanded into large red patches intermixed with the progeny of unmarked stem cells. RFP<sup>+</sup> cells were isolated from 2D patches and sub-cultured to determine if the RFP<sup>+</sup> patches contained cells with colonic stem cell properties. The RFP<sup>+</sup> cells continued to expand into patches composed only of RFP<sup>+</sup> cells (Figure 3b). The RFP<sup>+</sup> cell monolayers possessed proliferative (EDU<sup>+</sup>) cells, and the differentiated cell types: goblet cells (Muc2<sup>+</sup>), enteroendocrine cells (CHROMOGRANIN A [ChgA]<sup>+</sup>) and absorptive colonocytes (ALP<sup>+</sup>) (Figure 3c). These data demonstrate that the 2D monolayers possessed Lgr5 ISCs that expanded as a proliferative monolayer and produced differentiated descendants *in vitro*.

### **Human rectal epithelial cells form proliferative 2D monolayers**

To determine whether human rectal epithelial cells might form a proliferative monolayer, human rectal crypts obtained from rectal biopsies were cultured on collagen hydrogel in medium with the appropriate growth factors.  $85 \pm 5\%$  crypts (n=3, 20 crypts monitored per experiment) formed a monolayer that expanded in area over time (Figure 4a). The cells were sub-cultured every 5-7 days and maintained as a monolayer. The human 2D monolayer and 3D organoids could be interconverted without loss of proliferative capability (Figure 4b,c). Similar to 3D organoid culture, the cells remained proliferative with cell number increasing over time (Figure 4d). The doubling times measured during log-linear cell growth were 46.5 hours (95% C.I. bounds of 39.4 hours and 56.6 hours) for 2D monolayer and 47.1 hours (95% C.I. bounds of 40.8 hours and

55.8 hours) for 3D organoids. The human cells demonstrated a normal karyotype at passage number 6 (supplementary Figure 2). When examined by EM, the apical surface of the 2D monolayer demonstrated microvilli at varying density suggesting the presence of cells of absorptive colonocyte lineage since microvilli are a hallmark of these absorptive cells (Figure 4e). At day 3 in culture, all 3D organoids and 2D monolayer patches possessed actively proliferating cells (EDU<sup>+</sup> and SOX9<sup>+</sup>) suggesting the presence of stem and progenitor cell lineages (Figure 4f,g).<sup>220-222</sup> Goblet cells (Muc2<sup>+</sup>) and enteroendocrine cells (ChgA<sup>+</sup>) were observed in both human 3D organoids and 2D monolayers at day 6 in culture indicating the presence of differentiated cells (Figure 4f,g). Cells in the 2D monolayer possessed  $\beta$ -CATENIN at the intercellular borders suggesting the formation of tight intercellular connections (Figure 4g). The cells also demonstrated appropriate polarity with ACTIN and INTEGRIN- $\beta$ 4 localized to their apical and basal surfaces, respectively (Figure 4g). These data demonstrate that the collagen hydrogel system supports the proliferation of human rectal epithelial cells as a 2D monolayer.

### **Screening dietary components and food metabolites on murine colonic monolayers reveals specific impacts on cell proliferation and differentiation**

Sustainable 2D monolayers derived from primary tissue represent a transformative technology for personalized and precision medicine applications that rely on drug and compound screening. Critical for high-throughput screening platforms is the flat, accessible luminal surface of the monolayer, permitting cell interrogation with conventional assays and instrumentation including high-content microscopy.

To demonstrate the utility of the 2D murine colonic monolayers, 77 naturally occurring compounds found in food and metabolites of digestion were assayed for their ability to alter proliferation and differentiation, attributes that are central to intestinal barrier function and repair in the face of repeated chemical, physical, immune and infectious insults. The 77 compounds represented a range of chemical classes with diverse or unknown impact on primary intestinal cells and included bioactive food components and metabolites such as fatty acids, bile acids, flavenoids, phytoestrogens, phenols, terpenoids, nitrates, and others (supplementary Table 2).

Monolayers were grown for 24 h under normal Wnt-3A concentration of 30 ng/mL (ENR-W) followed by incubation with the dietary/natural compounds in a reduced Wnt-3A concentration of 10 ng/mL (ENR-w) for 48 h. Decreased Wnt-3A in the media was used to bring the levels of Wnt signaling to a threshold that would make pro-proliferative or pro-differentiation effects of the compounds readily apparent. After exposing 2D monolayers to exogenous compounds, the monolayers were sequentially stained for proliferative (EDU) and differentiated cells (absorptive colonocytes and goblet) (Figure 5, supplementary Figures 4 and 5). Quantitative image analysis of the fluorescence intensities for lineage readouts was used to compare monolayers exposed to the compounds and the control monolayers that lacked exposure to the compounds.

Differences between the dietary compounds and negative controls were assessed using the strictly standardized mean difference (SSMD), a commonly used statistic to identify potential hits in a library screen.<sup>211</sup> SSMD is a measure of the average fold change between a test compound and a negative reference penalized by the variability of the fold change. Multiple compounds (19/77, 25%) were growth suppressive,

reducing the Hoechst-stained area (*e.g.* cell number) relative to that of the control cells with fairly strong or stronger SSMD effect sizes (Figure 5a, b, supplementary Figure 4). Growth inhibitory compounds included many of the fatty acids, nitrates, terpenoids and curcuminoids. Only 9 of 77 (12%) compounds demonstrated increased cell numbers relative to that of the control with fairly strong or stronger SSMD effect sizes. A number of other compounds, such as the phenols gallic acid (#28) and ellagic acid (#29), suppressed the number of cells in S-phase without reducing the number of nuclei. Other molecules such as valproate (#6) and  $\beta$ -carotene (#58) display a similar growth suppressive effect. A single compound, isorhamnetin (#21, a component of ginkgo biloba), greatly increased cell numbers in S-phase. Four of the 77 (5%) molecules (eucalyptol, #42; punicalagin, #31; phytol, #51; indole-3-butyric acid, #72) directed cells towards the absorptive colonocyte lineage as indicated by substantially increased ALP activity (Figure 5c). Finally, a single compound, N-nitrosoanabasine (#65), increased Muc2 expression with a moderate effect size (Figure 5c). These findings demonstrate the potential of this 2D format as a high-content screening system to assay the impact of dietary compounds and microbial metabolites on intestinal health and disease.

To demonstrate the utility of 2D cultures over 3D cultures for enhanced compound screening, fourteen compounds yielding significant alteration in proliferation or differentiation of the murine 2D colonic cells were also assayed for their impact on the 3D murine organoids (Figure 6a,b). The compounds were added to the 3D organoids embedded in Matrigel and then assayed in a manner similar to that for the monolayer. The general response of the organoids to many of the compounds was similar to that of the 2D monolayer (Figure 6c). However, compound assay on the 3D organoids was

significantly more complex relative to that on the monolayers and this may account for many of the differences that were observed. The organoids existed in multiple image planes and underwent uncontrolled shape and size changes during the fixation/staining process making quantification of fluorescence, area and volume challenging. The surface area occupied by the Hoechst stain in the monolayers acted as an easily quantifiable and reliable surrogate for cell number in the 2D monolayers; however, for the reasons stated above, this metric was not possible with the 3D organoids when using conventional microscopy. The inability to use a simple metric such as Hoechst fluorescence surface area or intensity to track changes in cell number highlights the challenges for high throughput compound screens using 3D organoids. Staining for ALP and MUCIN2 was a simple process in the 2D monolayers with staining reagents added to the luminal monolayer surface where these molecules reside. In contrast, reagents added to the 3D organoids must diffuse through a hydrogel and cell layer to access the luminal epithelium of the organoid. For example, we observed that fragmented or burst organoids stained more intensely for ALP (located at the luminal cell surface) relative to intact organoids in response to the same compound. Tannic acid (#27) significantly reduced cell growth in the 2D monolayers but not in the 3D organoids. This may be due to the different cell surfaces (luminal side in 2D and basal side in 3D) to which the compound was added. Tannic acid's lack of membrane permeability may have prevented exposure of the luminal organoid surface to this molecule. This comparison between the monolayers and organoids demonstrates the fundamental differences in the two systems as well as the significant advantages of the monolayers in screening applications

## **Screening dietary metabolites and natural products on human tumor cell lines and primary human rectal cells**

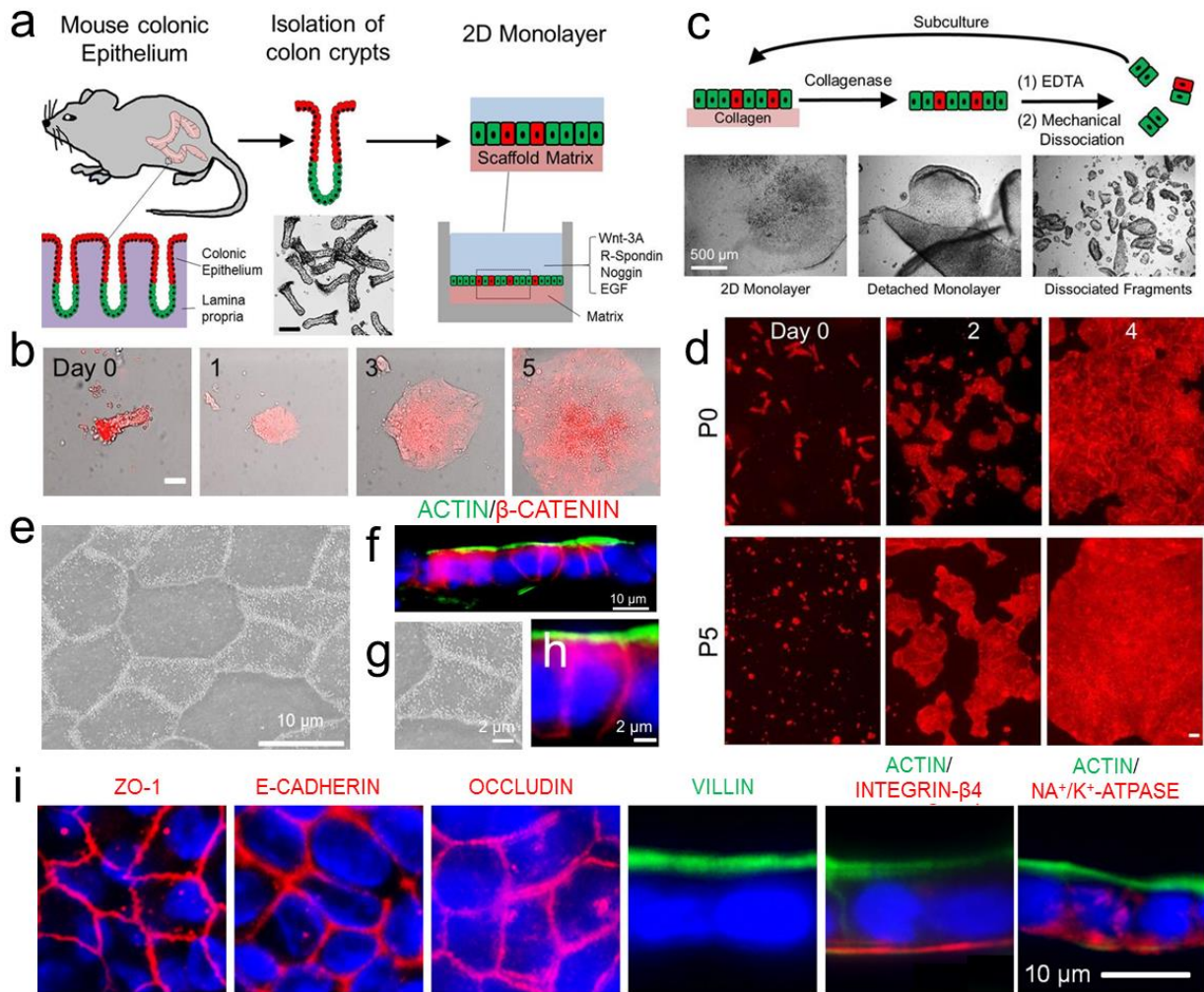
Tumor-derived Caco-2 cells have been adopted by pharmaceutical and biotechnology companies as the industry-standard for drug screening in the intestine. To determine if there are different responses of Caco-2 cells and the 2D primary tissue-derived monolayers, the impact of 7 of the screened compounds on Caco-2 monolayers was assayed and compared to the results obtained from primary human monolayers. The tumor cells were cultured in their standard medium and human primary cells cultured in HISC for 24 h followed by addition of the library compounds. After 48 h, the primary human and Caco-2 cells were stained and evaluated for cell number, proliferation, absorptive-cell phenotype, and goblet cell attributes as described for murine 2D cultures (Figure 7). At least 50% of the measurements trended in the opposite direction when the response of the two cell types to the compounds was measured. For example, valproate (#6) decreased nuclear coverage and increased ALP expression in Caco-2 cells, but generated the opposite responses in the primary cells. Thus, valproate may direct Caco-2 cells but not primary cells into the absorptive-cell lineage under these conditions. Punicalagin (#31) strongly reduced EDU incorporation in the primary cells, but generated the opposite effect in the Caco-2 cells. Punicalagin slows the growth of primary cells, but may encourage proliferation in the tumor cells. These data demonstrate distinct differences between the Caco-2 tumor cells and the 2D primary monolayer for a number of compounds suggesting that a more physiologically relevant cell platform may provide results that more closely represent those *in vivo*. A larger compound screen would likely reveal a greater number of discrepancies between

the two cell types. Nevertheless, these data demonstrate that the human monolayers are suitable for compound screening in a manner similar to the murine monolayers.

## **CONCLUSIONS**

Studies using 3D colonic organoids have provided novel insights into intestinal biology; however, the enclosed organoid architecture possesses severe limitations in screening applications and for many basic biomedical investigations. The organoid lumen buried within a hydrogel is inaccessible to drugs, toxins, probiotics, microbiota and other agents in contrast to the gut lumen of a living animal. We developed a self-renewing, 2D monolayer derived from primary intestinal tissue and possessing all cell lineages found within the colon. Long-term cell proliferation on the collagen hydrogel was likely due to its similar chemical makeup and stiffness relative to that of the basement membrane underlining the colonic epithelium. Cells of the organoids expand at a slower rate than those of the monolayer potentially as a result of the added requirement of the hydrogel-embedded cells to remove and remodel the matrix during expansion. Remarkably, the monolayers self-pattern to create peripheral stem/proliferative and central differentiated cell zones. The interior of the monolayer yields a large surface area occupied predominantly by differentiated cells, a feature mimicking that of the intestinal surface area *in vivo*. Importantly, the chemical environment of the monolayer is readily manipulated by addition of compounds to the media overlying the cells. This programmable feature in combination with the open architecture and accessible luminal face enables facile assay of drugs, toxins, and metabolites not possible in the organoid systems. Standard high-content microscopy methods were readily paired with the 2D monolayers to identify the impact of dietary

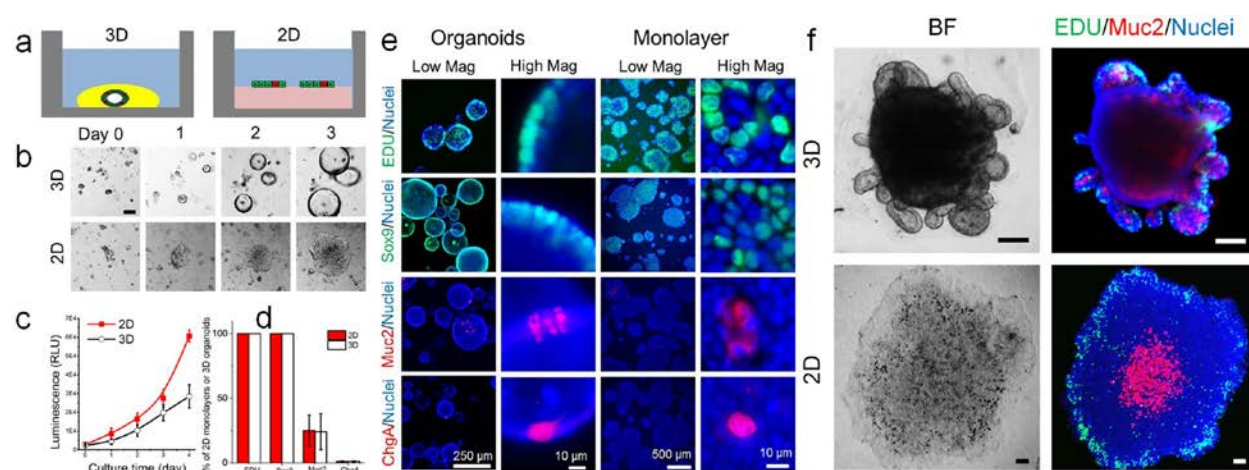
metabolites and natural products on primary intestinal cells obtained directly from animal models.



**Appendix B: Figure 1. Proliferative 2D monolayer culture of murine colonic crypts on the surface of collagen hydrogel.**

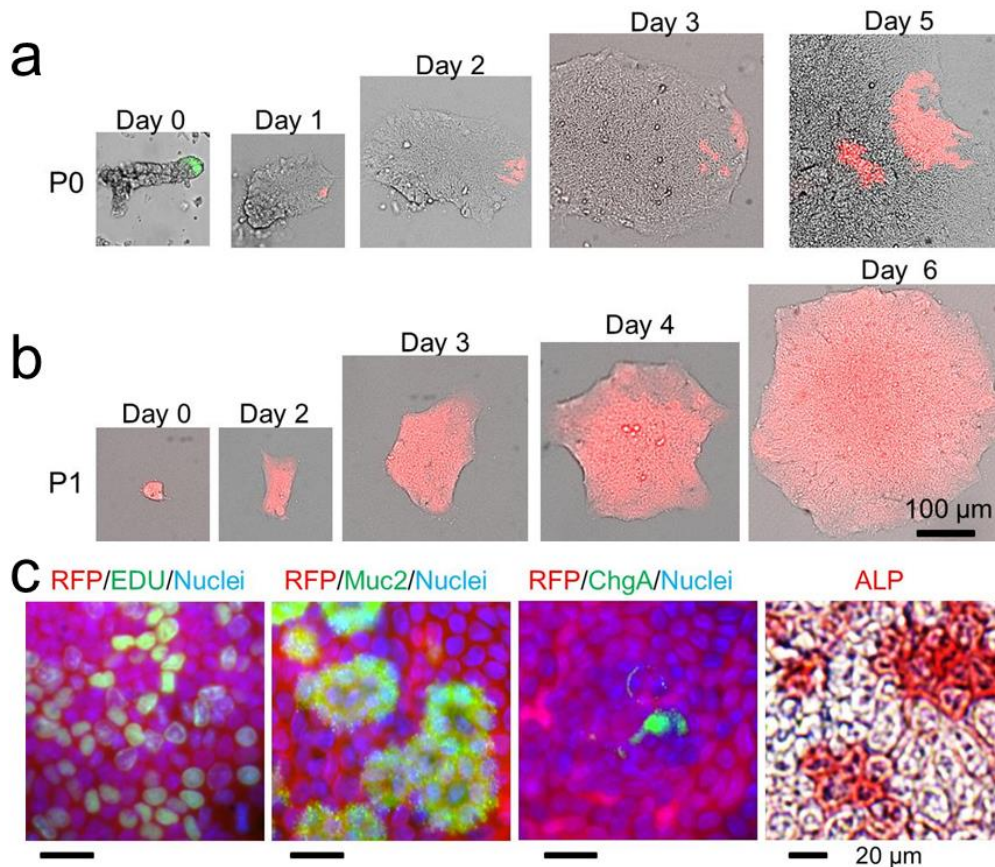
(a) Workflow for culturing crypts on a matrix surface. Wnt-3A, R-spondin, Noggin and EGF are used in the culture medium. Proliferative stem cells and progenitors (green);

differentiated cells (red). (b) Time-lapse images of crypts cultured on the top of collagen hydrogel. Brightfield images are superimposed on DsRed fluorescence images. Crypts express DsRed under a constitutive chicken-actin promoter. (c) Workflow for subculturing 2D monolayers. Monolayers are dissociated from collagen and split. Brightfield images (bottom) demonstrate representative cells at workflow stages. (d) Time-lapse fluorescence (DsRed) images of crypt-derived cells on collagen at passage number 0 (P0, crypts) and passage number 5 (P5). Scale bar =100  $\mu\text{m}$  (a-d). (e) SEM image of a monolayer on collagen gel at day 3 of culture. (f) Fluorescence image of a cross-section through the monolayer immunostained for ACTIN (green) and  $\beta$ -CATENIN (red). The distribution of  $\beta$ -CATENIN (an intracellular protein) demonstrating columnar shaped cells with a height of  $9.4\pm 0.8\ \mu\text{m}$  and width of  $7.5\pm 0.9\ \mu\text{m}$  ( $n=10$ ). (g) High magnification view of a subregion of panel e. (h) High magnification view of a subregion of panel f. (i) Staining for ZO-1, E-CADHERIN, or OCCULUDIN (red); VILLIN or ACTIN (green); INTEGRIN- $\beta 4$  and NA $^+$ /K $^+$ -ATPASE (red). Nuclei (blue).



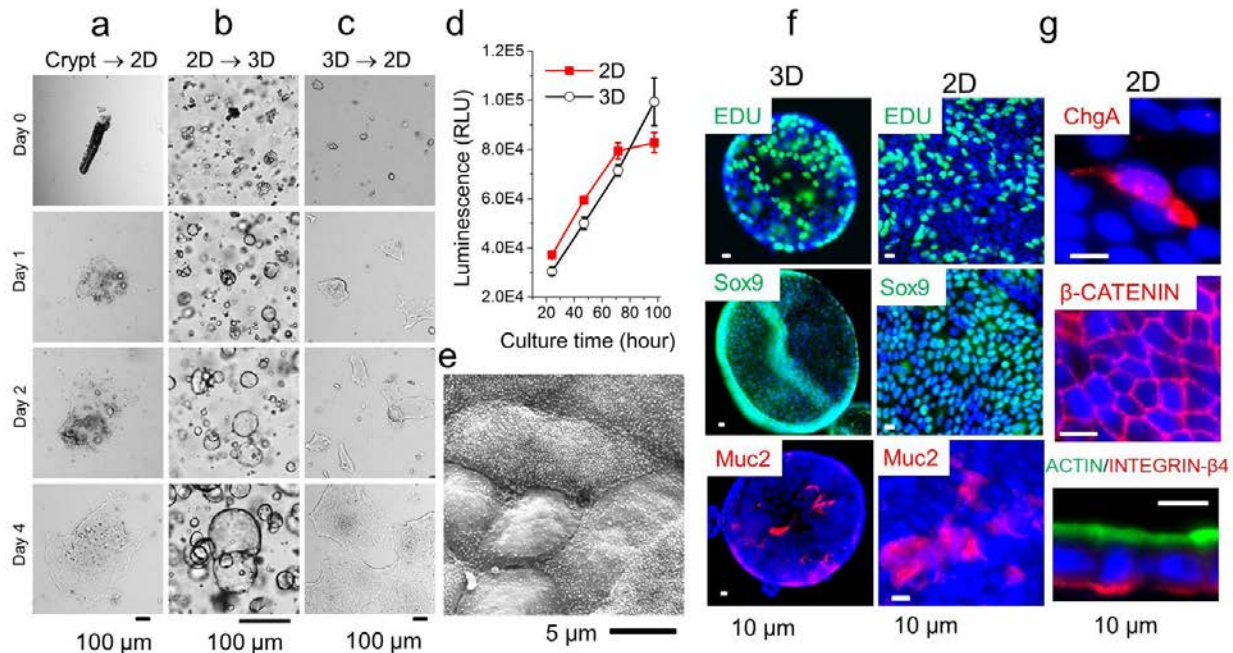
**Appendix B: Figure 2. Proliferative capacity, lineage composition, and compartmentalization are highly similar between 2D murine colonic monolayers and 3D organoids.**

(a) Schematic showing the culture format for organoids and monolayers. (b) Time-lapse images demonstrating the growth and morphologies of crypt-derived organoids and monolayers at passage number 2 (P2). (c) Quantification of cellular growth over time in organoids and monolayers measured by a proxy assay (CellTiter-Glo luminescence, n=4). (d) Percentage of monolayer patches and organoids at day 3 demonstrating positive staining for proliferative and differentiated cell lineages (EDU, SOX9, Muc2 and ChgA; n=3, 20 monolayer patches or organoids per experiment). (e) Fluorescence images of organoids and monolayers at day 3 (EDU [green], SOX9 [green], Muc2 [red], ChgA [red], and nuclei [blue]). (f) Compartmentalization of proliferative stem/progenitor cells and differentiated cells. Brightfield (left column) and fluorescence (right column) images of organoids (top row) and monolayers (bottom row) at culture day 8 (EDU [green], Muc2 [red], and nuclei [blue]). Of the 3D mature organoids, 80±10% (10 organoids/well, n=3 wells) demonstrated increased stem/progenitors (EDU+) collections in the buds while 100±0% (10 monolayer patches/well, n=3 wells) of the monolayers demonstrated EDU+ cells localized to the periphery of the patch. In a majority (83±6%, 10 monolayer patches/well, n=3 wells) of monolayer patches, Muc2+ was found only in the central-most region of the patch. Mucin was present in the lumen of all 3D organoids. Scale bar = 100 µm unless denoted otherwise.



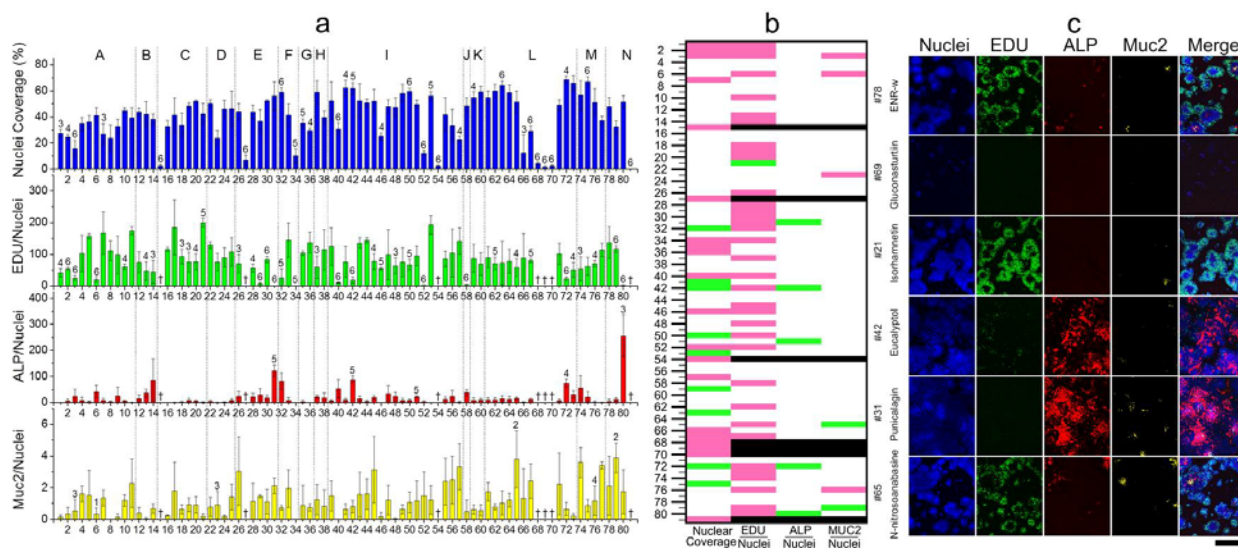
**Appendix B: Figure 3. Lineage tracing of mouse colonic epithelial cells in the 2D monolayer.**

(a) Time lapse images after isolation and culture of a single colonic crypt from a tamoxifen-injected *Lgr5EGFP*CreERT2xR26 confetti mouse. The presence of stem cells or *Lgr5*<sup>+</sup> cells (green, EGFP) is readily seen at day 0. At day 1 and later, a tracing event is observed with expression of RFP (red) marking the progeny of a single stem cell. (b) Post-isolation and passage of RFP<sup>+</sup> cells from panel A. (c) EDU, Muc2, ChgA and ALP stains of monolayers of RFP<sup>+</sup> cells revealed that the monolayer was composed of proliferative cells (EDU<sup>+</sup>, in the presence of Wnt-3A) and differentiated cells (Muc2<sup>+</sup> goblet cells, ChgA<sup>+</sup> enteroendocrine cells, ALP<sup>+</sup> absorptive colonocytes) in the absence of Wnt-3A.



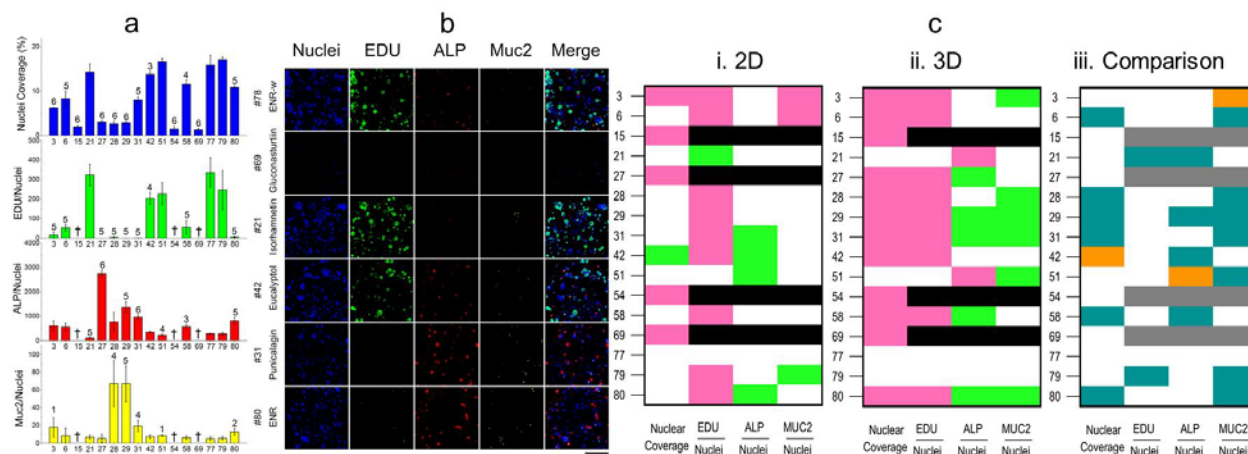
**Appendix B: Figure 4. Human rectal epithelial cells can be cultured as a proliferative 2D monolayer.**

(a) A crypt cultured on the top of collagen hydrogel grew as a 2D monolayer. (b) Conversion of fragments of 2D monolayer to 3D organoids. The 3D organoids possessed a thin wall and cystic structure. (c) Conversion of 3D organoids to a 2D monolayer. 3D organoids were extracted from Matrigel (day 4 in culture) and plated on the top of the collagen hydrogel. (d) Cellular growth over time in organoids and monolayers measured by a cell viability assay (CellTiter-Glo luminescence, n=3). (e) SEM image of a monolayer on collagen hydrogel at day 3 of culture. (f) Fluorescence images of organoids showing EDU staining (green, at day 3), Sox9 (green, at day3), and Muc2 (red, at day 6) immunostaining. (g) Fluorescence images of monolayers showing EDU staining (green, at day 3), Sox9 (green, at day3), Muc2 (red, at day 6), ChgA (red, at day 6), β-CATENIN (red, at day 6), ACTIN (green) and INTEGRIN-β4 (red, at day 6) immunostaining. In all images Hoechst 33342 (blue) marked the nuclei.



**Appendix B: Figure 5. The impact of dietary compounds and natural products on primary murine colonic monolayers.**

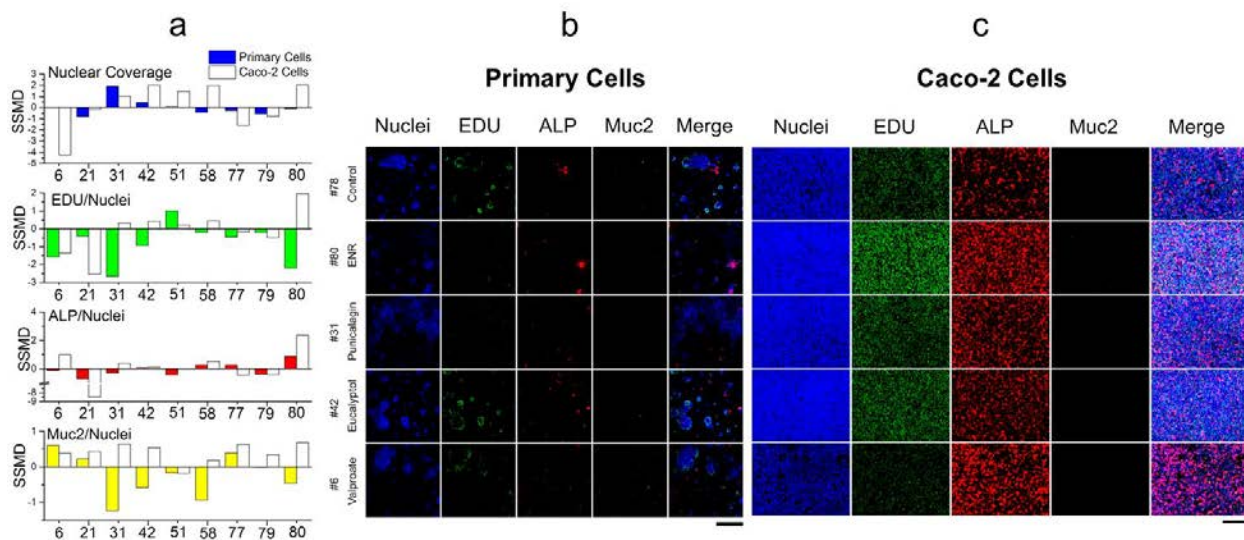
(a) The percentage of the collagen surface area that was positive for Hoechst 33342 and the normalized fluorescence intensity due to EDU incorporation, ALP activity, or Muc2 staining was plotted against the compound number. EDU, ALP and Muc2 fluorescence signals were normalized by summing the fluorescence intensity and dividing by the nuclear percent area (i.e. an indicator of cell number). Hits were designated as: 6- extremely strong, 5- very strong, 4- strong, 3- fairly strong, 2- moderate, 1- fairly moderate (“Moderate” and “fairly moderate” effects were designated only for compounds within the Muc2 screen). †: cultures with extensive cell death (< 10% nuclear coverage). (b) Map of hit compounds. Green and pink indicate an increased or decreased value (respectively) relative to that of the control (ENR-w). Black indicates cultures with extensive cell death. (c) Representative fluorescence images from the compound screen. Scale bar = 1 mm.



**Appendix B: Figure 6. Assaying a subset of the dietary compounds and metabolites on murine 3D organoids.**

(a) The percentage of the collagen surface area that was positive for Hoechst 33342 and the normalized fluorescence intensity due to EDU incorporation, ALP activity, or Muc2 staining was plotted against the compound number. EDU, ALP and Muc2 fluorescence signals were normalized by summing the fluorescence intensity and dividing by the nuclear percent area (i.e. an indicator of cell number). Hits were designated as subtypes: 6- extremely strong, 5- very strong, 4- strong, 3- fairly strong, 2- moderate, 1- fairly moderate (“Moderate” and “fairly moderate” effects were designated only for compounds within the Muc2 screen). †: cultures with extensive cell death (< 10% nuclear coverage for 2D or < 2% nuclear coverage for 3D). (b) Representative fluorescence images from the assay. Scale bar = 1 mm. (c) i) and ii)- Comparison of the effect of selected compounds on the 2D monolayer and 3D organoids. Green and pink indicate an increased or decreased (respectively) value relative to that of the control (ENR-w). Black indicates cultures with extensive cell death. iii) Direct comparison of the responses of the 2D monolayers and 3D colonoids to the

compounds. White indicates a strong response by both cultures in the same direction (enhanced or diminished effect) or a weak response by both cultures. Green-blue indicates a strong response in one culture system, but not the other. Orange indicates strong responses in both cultures, but in opposite directions. Grey indicates that no comparison of the two cell types was made.



**Appendix B: Figure 7. The impact of seven dietary compounds and natural products on human primary rectal and tumor Caco-2 cells.**

(a) The SSMD effect size was plotted against the compound number for the four screen readouts: the percentage of the image surface area that was positive for Hoechst 33342 and the normalized fluorescence intensity due to EDU incorporation, ALP activity, or Muc2 staining. EDU, ALP and Muc2 fluorescence signals were normalized by summing the fluorescence intensity and dividing by the nuclear percent area (i.e. an indicator of cell number).  $|\text{SSMD}| > 1.645$  is required to designate a strong effect size. (b,c) Representative fluorescence images from the assays. Control media for Caco-2 cells was DMEM medium. Scale bar = 1 mm.

## REFERENCES

1. Cheng, H. & Leblond, C. P. Origin, differentiation and renewal of 4 main epithelial cell types in mouse small intestine. *Am. J. Anat.* **141**, 537–561 (1974).
2. Cheng, H. & Leblond, C. P. Origin, differentiation and renewal of the four main epithelial cell types in the mouse small intestine V. Unitarian theory of the origin of the four epithelial cell types. *Am. J. Anat.* **141**, 537–561 (1974).
3. Quastler, H. & Sherman, F. G. Cell population kinetics in the intestinal epithelium of the mouse. *Exp. Cell Res.* **17**, 420–438 (1959).
4. Sancho, E., Batlle, E. & Clevers, H. Signaling Pathways in Intestinal Development and Cancer. *Annu. Rev. Cell Dev. Biol.* **20**, 695–723 (2004).
5. He, X. C. *et al.* BMP signaling inhibits intestinal stem cell self-renewal through suppression of Wnt- $\beta$ -catenin signaling. *Nat. Genet.* **36**, 1117–1121 (2004).
6. Haramis, A. P. G. *et al.* De Novo Crypt Formation and Juvenile Polyposis on BMP Inhibition in Mouse Intestine. *Science (80- )*. **303**, 1684–1686 (2004).
7. Sato, T. *et al.* Paneth cells constitute the niche for Lgr5 stem cells in intestinal crypts. *Nature* **469**, 415–418 (2011).
8. Noah, T. K. & Shroyer, N. F. Notch in the Intestine: Regulation of Homeostasis and Pathogenesis. *Annu. Rev. Physiol.* **75**, 263–288 (2013).
9. Crosnier, C., Stamatakis, D. & Lewis, J. Organizing cell renewal in the intestine: Stem cells, signals and combinatorial control. *Nat. Rev. Genet.* **7**, 349–359 (2006).
10. Clevers, H. & Nusse, R. Wnt/ $\beta$ -catenin signaling and disease. *Cell* **149**, 1192–1205 (2012).
11. Barker, N. *et al.* Identification of stem cells in small intestine and colon by marker gene Lgr5. *Nature* **449**, 1003–1007 (2007).
12. Furuyama, K. *et al.* Continuous cell supply from a Sox9-expressing progenitor zone in adult liver, exocrine pancreas and intestine. *Nat. Genet.* **43**, 34–41 (2011).
13. Gracz, A. D., Ramalingam, S. & Magness, S. T. Sox9 expression marks a subset of CD24-expressing small intestine epithelial stem cells that form organoids in vitro. *AJP Gastrointest. Liver Physiol.* **298**, G590–G600 (2010).
14. van der Flier, L. G. *et al.* Transcription Factor Achaete Scute-Like 2 Controls Intestinal Stem Cell Fate. *Cell* **136**, 903–912 (2009).
15. van der Flier, L. G., Haegebarth, A., Stange, D. E., van de Wetering, M. & Clevers, H. OLFM4 Is a Robust Marker for Stem Cells in Human Intestine and Marks a Subset of Colorectal Cancer Cells. *Gastroenterology* **137**, 15–17 (2009).
16. Sangiorgi, E. & Capecchi, M. R. Bmi1 is expressed in vivo in intestinal stem cells. *Nat. Genet.* **40**, 915–920 (2008).

17. Montgomery, R. K. *et al.* Mouse telomerase reverse transcriptase (mTert) expression marks slowly cycling intestinal stem cells. *Proc. Natl. Acad. Sci.* **108**, 179–184 (2011).
18. Takeda, N. *et al.* Interconversion Between Intestinal Stem Cell Populations in Distinct Niches. *Science (80-. )*. **334**, 1420–1424 (2011).
19. Lignot, J. H., Helmstetter, C. & Secor, S. M. Postprandial morphological response of the intestinal epithelium of the Burmese python (*Python molurus*). *Comp. Biochem. Physiol. - A Mol. Integr. Physiol.* **141**, 280–291 (2005).
20. TSUKAHARA, T., INOUE, R., YAMADA, K. & YAJIMA, T. A Mouse Model Study for the Villous Atrophy of the Early Weaning Piglets. *J. Vet. Med. Sci.* **72**, 241–244 (2010).
21. Allison, C., McFarlan, C. & Macfarlane, G. T. Studies on mixed populations of human intestinal bacteria grown in single-stage and multistage continuous culture systems. *Appl. Environ. Microbiol* **55**, 672–678 (1989).
22. Pompei, A. *et al.* Folate production by bifidobacteria as a potential probiotic property. *Appl. Environ. Microbiol.* **73**, 179–185 (2007).
23. Coker, O. O. *et al.* Mucosal microbiome dysbiosis in gastric carcinogenesis. *Gut* gutjnl-2017-314281 (2017). doi:10.1136/gutjnl-2017-314281
24. Eckburg, P. B. *et al.* Diversity of the human intestinal microbial flora. **308**, 1635–1638 (2005).
25. Fearon, E. F. & Vogelstein, B. A Genetic Model for Colorectal Tumorigenesis. *Cell* **61**, 759–767 (1989).
26. Brenner, H., Kloor, M. & Pox, C. P. Colorectal cancer. *Lancet* **383**, 1490–1502 (2014).
27. Vogelstein, B. *et al.* Genetic Alterations during Colorectal-Tumor Development. *N. Engl. J. Med.* **319**, 525–532 (1988).
28. Jemal, A., Thomas, A., Murray, T. & Thun, M. Cancer Statistics , 2002. **52**, 23–47 (2002).
29. De Lisle, R. C. & Borowitz, D. The cystic fibrosis intestine. *Cold Spring Harb. Perspect. Med.* **3**, 1–17 (2013).
30. O’Sullivan, B. P. & Freedman, S. D. Cystic fibrosis. *Lancet* **373**, 1891–1904 (2009).
31. Swidsinski, A. *et al.* Mucosal flora in inflammatory bowel disease. *Gastroenterology* **122**, 44–54 (2002).
32. Sartor, R. B. Microbial Influences in Inflammatory Bowel Diseases. *Gastroenterology* **134**, 577–594 (2008).

33. Macfarlane, G. T. & Macfarlane, S. Models for intestinal fermentation: association between food components, delivery systems, bioavailability and functional interactions in the gut. *Curr. Opin. Biotechnol.* **18**, 156–162 (2007).
34. Basu, S., Haase, G. & Ben-Ze'ev, A. Wnt signaling in cancer stem cells and colon cancer metastasis. *F1000Research* **5**, 699 (2016).
35. Ley, R., Turnbaugh, P., Klein, S. & Gordon, J. Microbial ecology: human gut microbes associated with obesity. *Nature* **444**, 1022–3 (2006).
36. Ley, R. E. *et al.* Obesity alters gut microbial ecology. *Proc. Natl. Acad. Sci.* **102**, 11070–11075 (2005).
37. Turnbaugh, P. J. *et al.* The Human Microbiome Project. *Nature* **449**, 804–810 (2007).
38. Gill, S., Pop, M., DeBoy, R. & Eckburg, P. Metagenomic analysis of the human distal gut microbiome. *Science (80-. )*. **312**, 1355–1359 (2006).
39. Morgan, X. C. & Huttenhower, C. Chapter 12: Human Microbiome Analysis. *PLoS Comput. Biol.* **8**, 1–20 (2012).
40. Tomkovich, S. & Jobin, C. Microbiota and host immune responses: A love-hate relationship. *Immunology* **147**, 1–10 (2016).
41. Karin, M. & Clevers, H. Reparative inflammation takes charge of tissue regeneration. *Nature* **529**, 307–315 (2016).
42. Britton, G. J. *et al.* Inflammatory bowel disease microbiotas alter gut CD4 T-cell homeostasis and drive colitis in mice. *bioRxiv* 276774 (2018). doi:10.1101/276774
43. Jones, R. M. The influence of the gut microbiota on host physiology: In pursuit of mechanisms. *Yale J. Biol. Med.* **89**, 285–297 (2016).
44. Kabeerdoss, J., Jayakanthan, P., Pugazhendhi, S. & Ramakrishna, B. S. Alterations of mucosal microbiota in the colon of patients with inflammatory bowel disease revealed by real time polymerase chain reaction amplification of 16S ribosomal ribonucleic acid. *Indian J. Med. Res.* **142**, 23–32 (2015).
45. Marchesi, J. R. *et al.* The gut microbiota and host health: A new clinical frontier. *Gut* **65**, 330–339 (2016).
46. Guo, S. *et al.* Secreted metabolites of *Bifidobacterium infantis* and *Lactobacillus acidophilus* protect immature human enterocytes from IL-1 $\beta$ -induced inflammation: A transcription profiling analysis. *PLoS One* **10**, 1–19 (2015).
47. Ghouri, Y. A. *et al.* Systematic review of randomized controlled trials of probiotics, prebiotics, and synbiotics in inflammatory bowel disease. *Clin Exp Gastroenterol* **7**, 473–487 (2014).
48. Manuscript, A. & Proteasome, I. NIH Public Access. **15**, 1537–1547 (2009).

49. Shah, S. H. *et al.* Branched-chain amino acid levels are associated with improvement in insulin resistance with weight loss. *Diabetologia* **55**, 321–330 (2012).
50. Sobhani, I. *et al.* Microbial dysbiosis in colorectal cancer (CRC) patients. *PLoS One* **6**, (2011).
51. Marchesi, J. R. *et al.* Towards the Human Colorectal Cancer Microbiome. *PLoS One* **6**, e20447 (2011).
52. Garrett, W. S. *et al.* Colitis-Associated Colorectal Cancer Driven by T-bet Deficiency in Dendritic Cells. *Cancer Cell* **16**, 208–219 (2009).
53. Terzić, J., Grivennikov, S., Karin, E. & Karin, M. Inflammation and Colon Cancer. *Gastroenterology* **138**, 2101–2114 (2010).
54. El Aidy, S. *et al.* Gut bacteria-host metabolic interplay during conventionalisation of the mouse germfree colon. *ISME J.* **7**, 743–755 (2013).
55. Trotter, P. J. & Storch, J. Fatty acid esterification during differentiation of the human intestinal cell line Caco-2. *J. Biol. Chem.* **268**, 10017–23 (1993).
56. Arrieta, M. C., Walter, J. & Finlay, B. B. Human Microbiota-Associated Mice: A Model with Challenges. *Cell Host Microbe* **19**, 575–578 (2016).
57. Sato, T. *et al.* Single Lgr5 stem cells build crypt-villus structures in vitro without a mesenchymal niche. *Nature* **459**, 262–265 (2009).
58. VanDussen, K. L. *et al.* Development of an enhanced human gastrointestinal epithelial culture system to facilitate patient-based assays. *Gut* **64**, 911–920 (2015).
59. Wang, Y., Ahmad, A. A., Sims, C. E., Magness, S. T. & Allbritton, N. L. In vitro generation of colonic epithelium from primary cells guided by microstructures. *Lab Chip* **14**, 1622–1631 (2014).
60. Zachos, N. C. *et al.* Human Enteroids / Colonoids and Intestinal Organoids Functionally Recapitulate and Pathophysiology \*. *J. Biol. Chem.* **291**, 3759–3766 (2016).
61. Yin, X. *et al.* Niche-independent high-purity cultures of Lgr5 + intestinal stem cells and their progeny. *Nat. Methods* **11**, 106–112 (2014).
62. Richmond, C. A. & Breault, D. T. Move Over Caco-2 Cells: Human-Induced Organoids Meet Gut-on-a-Chip. *Cmgh* 4–5 (2018). doi:10.1016/j.jcmgh.2018.01.016
63. Leushacke, M. & Barker, N. Ex vivo culture of the intestinal epithelium: Strategies and applications. *Gut* **63**, 1345–1354 (2014).
64. Sato, T. *et al.* Growing Self-Organizing Mini-Guts from a Single Intestinal Stem Cell: Mechanism and Applications. *Science (80- )*. **340**, 241–260 (2013).
65. Schwank, G. *et al.* Functional repair of CFTR by CRISPR/Cas9 in intestinal stem cell organoids of cystic fibrosis patients. *Cell Stem Cell* **13**, 653–658 (2013).

66. Koo, B. K. *et al.* Controlled gene expression in primary Lgr5 organoid cultures. *Nat. Methods* **9**, 81–83 (2012).
67. Walton, K. D., Mishkind, D., Riddle, M. R., Tabin, C. J. & Gumucio, D. L. Blueprint for an intestinal villus: Species-specific assembly required. *Wiley Interdiscip. Rev. Dev. Biol.* 1–19 (2018). doi:10.1002/wdev.317
68. Saboor, M., Zehra, A., Qamar, K. & Moinuddin. Disorders associated with malabsorption of iron: A critical review. *Pakistan J. Med. Sci.* **31**, 1549–1553 (2015).
69. Leslie, J. L. & Young, V. B. A whole new ball game: Stem cell-derived epithelia in the study of host-microbe interactions. *Anaerobe* **37**, 25–28 (2016).
70. Clevers, H., Loh, K. M. & Nusse, R. An integral program for tissue renewal and regeneration: Wnt signaling and stem cell control. *Science (80- )*. **346**, (2014).
71. Rubin, D. C. CFTR and the Regulation of Crypt Cell Proliferation. *Cmgh* **5**, 418–419 (2018).
72. Barker, N. *et al.* Crypt stem cells as the cells-of-origin of intestinal cancer. *Nature* **457**, 608–611 (2009).
73. Ralls, M. W. *et al.* Bacterial nutrient foraging in a mouse model of enteral nutrient deprivation: insight into the gut origin of sepsis. *Am. J. Physiol. Liver Physiol.* **311**, G734–G743 (2016).
74. Hill, D. R. & Spence, J. R. Gastrointestinal Organoids: Understanding the Molecular Basis of the Host – Microbe Interface. *Cell. Mol. Gastroenterol. Hepatol.* **3**, 138–149 (2017).
75. Chevalier, C. *et al.* Gut Microbiota Orchestrates Energy Homeostasis during Cold Article Gut Microbiota Orchestrates Energy Homeostasis during Cold. 1360–1374 (2015). doi:10.1016/j.cell.2015.11.004
76. Bartfeld, S. & Clevers, H. Organoids as Model for Infectious Diseases: Culture of Human and Murine Stomach Organoids and Microinjection of Helicobacter Pylori. *J. Vis. Exp.* 1–9 (2015). doi:10.3791/53359
77. Bohórquez, D., Haque, F., Medicetty, S. & Liddle, R. A. Correlative Confocal and 3D Electron Microscopy of a Specific Sensory Cell. *J. Vis. Exp.* 1–8 (2015). doi:doi:10.3791/52918
78. Bohórquez, D. V. *et al.* An enteroendocrine cell - Enteric glia connection revealed by 3D electron microscopy. *PLoS One* **9**, (2014).
79. Cao, Y. *et al.* Long-term use of antibiotics and risk of colorectal adenoma. *Gut* **67**, 672–678 (2018).
80. Meng, D., Zhu, W., Ganguli, K., Shi, H. N. & Walker, W. A. Anti-inflammatory effects of *Bifidobacterium longum subsp infantis* secretions on fetal human enterocytes are mediated by TLR-4 receptors. *Am. J. Physiol. - Gastrointest. Liver Physiol.* **311**, G744–G753 (2016).

81. Zhang, Y. J., Xu, J. J., Wang, P. & Wang, J. L. Multidrug resistance gene and its relationship to ulcerative colitis and immune status of ulcerative colitis. *Genet. Mol. Res.* **13**, 10837–10851 (2014).
82. In, J. G. *et al.* Human mini-guts: New insights into intestinal physiology and host-pathogen interactions. *Nat. Rev. Gastroenterol. Hepatol.* **13**, 633–642 (2016).
83. Caminero, A. *et al.* Duodenal Bacteria From Patients With Celiac Disease and Healthy Subjects Distinctly Affect Gluten Breakdown and Immunogenicity. *Gastroenterology* **151**, 670–683 (2016).
84. Rodansky, E. S., Johnson, L. A., Huang, S., Spence, J. R. & Higgins, P. D. R. Intestinal organoids: A model of intestinal fibrosis for evaluating anti-fibrotic drugs. *Exp. Mol. Pathol.* **98**, 346–351 (2015).
85. Foulke-abel, J. *et al.* Human Enteroids as a Model of Upper Small Intestinal Ion Transport Physiology and Pathophysiology. 638–649 (2016). doi:10.1053/j.gastro.2015.11.047
86. Fatehullah, A., Tan, S. H. & Barker, N. Organoids as an in vitro model of human development and disease. *Nat Cell Biol* **18**, 246–254 (2016).
87. Davies, P. S., Dismuke, A. D., Powell, A. E., Carroll, K. H. & Wong, M. H. Wnt-reporter expression pattern in the mouse intestine during homeostasis. *BMC Gastroenterol.* **8**, 1–15 (2008).
88. Mariadason, J. M. *et al.* Gene expression profiling of intestinal epithelial cell maturation along the crypt-villus axis. *Gastroenterology* **128**, 1081–1088 (2005).
89. Gregorieff, A. *et al.* Expression Pattern of Wnt Signaling Components in the Adult Intestine. *Gastroenterology* **129**, 626–638 (2005).
90. Clevers, H. ST E M CELLS A unifying theory for the crypt. 0–1 (2013).
91. Krausova, M. & Korinek, V. Wnt signaling in adult intestinal stem cells and cancer. *Cell. Signal.* **26**, 570–579 (2014).
92. Ahmad, A. A. *et al.* Optimization of 3-D organotypic primary colonic cultures for organ-on-chip applications. *J. Biol. Eng.* **8**, 8–11 (2014).
93. Barker, N., Huls, G., Korinek, V. & Clevers, H. Restricted high level expression of Tcf-4 protein in intestinal and mammary gland epithelium. *Am. J. Pathol.* **154**, 29–35 (1999).
94. Hirata, A. *et al.* Dose-dependent roles for canonical Wnt signalling in de novo crypt formation and cell cycle properties of the colonic epithelium. *Development* **140**, 66–75 (2013).
95. Leedham, S. J. *et al.* A basal gradient of Wnt and stem-cell number influences regional tumour distribution in human and mouse intestinal tracts. *Gut* **62**, 83–93 (2013).
96. Clevers, H. XThe intestinal crypt, a prototype stem cell compartment. *Cell* **154**, 274–284 (2013).

97. Mccracken, K. W. *et al.* Modeling human development and disease in pluripotent stem cell-derived gastric organoids. *Nature* **516**, 400–404 (2015).
98. Kieckhafer, J. E. *et al.* The RNA Polymerase III Subunit Polr3b Is Required for the Maintenance of Small Intestinal Crypts in Mice. *Cmgh* **2**, 783–795 (2016).
99. Aoki, R. *et al.* Foxl1-Expressing Mesenchymal Cells Constitute the Intestinal Stem Cell Niche. *Cmgh* **2**, 175–188 (2016).
100. Jung, P. *et al.* Isolation and in vitro expansion of human colonic stem cells. *Nat. Med.* **17**, 1225–1227 (2011).
101. Sato, T. *et al.* Long-term expansion of epithelial organoids from human colon, adenoma, adenocarcinoma, and Barrett's epithelium. *Gastroenterology* **141**, 1762–1772 (2011).
102. Clevers, H. Modeling Development and Disease with Organoids. *Cell* **165**, 1586–1597 (2016).
103. Artursson, P., Palm, K. & Luthman, K. Caco-2 monolayers in experimental and theoretical predictions of drug transport. *Adv. Drug Deliv. Rev.* **64**, 280–289 (2012).
104. Natoli, M., Leoni, B. D., D'Agnano, I., Zucco, F. & Felsani, A. Good Caco-2 cell culture practices. *Toxicol. Vitro.* **26**, 1243–1246 (2012).
105. Sun, H., Chow, E. C., Liu, S., Du, Y. & Pang, K. S. The Caco-2 cell monolayer: usefulness and limitations. *Expert Opin. Drug Metab. Toxicol.* **4**, 395–411 (2008).
106. Wang, Y. *et al.* Micromolded arrays for separation of adherent cells. *Lab Chip* **10**, 2917 (2010).
107. Xu, W., Sims, C. E. & Allbritton, N. L. Microcup Arrays for the Efficient Isolation and Cloning of Cells. *Anal. Chem.* **82**, 3161–3167 (2010).
108. Lecault, V. *et al.* High-throughput analysis of single hematopoietic stem cell proliferation in microfluidic cell culture arrays. *Nat. Methods* **8**, 581–586 (2011).
109. A Direct Measurement of the Radiation Sensitivity of Normal Mouse Bone Marrow Cells Author ( s ): J . E . Till and E . A . McCulloch Published by : Radiation Research Society Stable URL : <http://www.jstor.org/stable/3570892> A Direct Measurement of the Rad. **14**, 213–222 (2016).
110. Shackleton, M. *et al.* Generation of a functional mammary gland from a single stem cell. *Nature* **439**, 84–88 (2006).
111. Gracz, A. D., Puthoff, B. J. & Magness, S. T. Somatic Stem Cells. **879**, 89–107 (2012).
112. Livet, J. *et al.* Transgenic strategies for combinatorial expression of fluorescent proteins in the nervous system. *Nature* **450**, 56–62 (2007).
113. Barker, N., van de Wetering, M., Clevers, H., Wetering, M. Van De & Clevers, H. The intestinal stem cell. *Genes Dev.* **22**, 1856–1864 (2008).

114. Gracz, A. D. *et al.* A high-throughput platform for stem cell niche co-cultures and downstream gene expression analysis. *Nat. Cell Biol.* **17**, 340–349 (2015).
115. Ramalingam, S., Daughtridge, G. W., Johnston, M. J., Gracz, A. D. & Magness, S. T. Distinct levels of Sox9 expression mark colon epithelial stem cells that form colonoids in culture. *AJP Gastrointest. Liver Physiol.* **302**, G10–G20 (2012).
116. Gobaa, S. *et al.* Artificial niche microarrays for probing single stem cell fate in high throughput. *Nat. Methods* **8**, 949–955 (2011).
117. Roccio, M., Gobaa, S. & Lutolf, M. P. High-throughput clonal analysis of neural stem cells in microarrayed artificial niches. *Integr. Biol.* **4**, 391 (2012).
118. Li, K., Bihan, M., Yooseph, S. & Methé, B. A. Analyses of the Microbial Diversity across the Human Microbiome. *PLoS One* **7**, e32118 (2012).
119. Wu, X. *et al.* Molecular characterisation of the faecal microbiota in patients with type II diabetes. *Curr. Microbiol.* **61**, 69–78 (2010).
120. Lau, E., Carvalho, D., Pina-Vaz, C., Barbosa, J.-A. & Freitas, P. Beyond gut microbiota: understanding obesity and type 2 diabetes. *Hormones* **14**, 358–369 (2015).
121. Petersen, C. & Round, J. L. Defining dysbiosis and its influence on host immunity and disease. *Cell. Microbiol.* **16**, 1024–1033 (2014).
122. Barlow, G. M., Yu, A. & Mathur, R. Role of the gut microbiome in obesity and diabetes mellitus. *Nutr. Clin. Pract.* **30**, 787–797 (2015).
123. Joglekar, P. & Segre, J. A. Building a Translational Microbiome Toolbox. *Cell* **169**, 378–380 (2017).
124. Whitaker, W. R., Shepherd, E. S. & Sonnenburg, J. L. Tunable Expression Tools Enable Single-Cell Strain Distinction in the Gut Microbiome. *Cell* **169**, 538–546.e12 (2017).
125. Lim, B., Zimmermann, M., Barry, N. A. & Goodman, A. L. Engineered Regulatory Systems Modulate Gene Expression of Human Commensals in the Gut. *Cell* **169**, 547–558.e15 (2017).
126. Bae, S., Mueller, O., Wong, S., Rawls, J. F. & Valdivia, R. H. Genomic sequencing-based mutational enrichment analysis identifies motility genes in a genetically intractable gut microbe. *Proc. Natl. Acad. Sci.* **113**, 14127–14132 (2016).
127. Browne, H. P. *et al.* Culturing of ‘unculturable’ human microbiota reveals novel taxa and extensive sporulation. *Nature* **533**, 543–546 (2016).
128. Auchtung, J. M., Robinson, C. D. & Britton, R. A. Cultivation of stable, reproducible microbial communities from different fecal donors using minibioreactor arrays (MBRAs). *Microbiome* **3**, 1–15 (2015).
129. Jabaji, Z. *et al.* Type I collagen as an extracellular matrix for the in vitro growth of human small intestinal epithelium. *PLoS One* **9**, 1–9 (2014).

130. In, J. *et al.* Enterohemorrhagic *Escherichia coli* Reduces Mucus and Intermicrovillar Bridges in Human Stem Cell-Derived Colonoids. *Cell. Mol. Gastroenterol. Hepatol.* **2**, 48–62.e3 (2016).
131. Moon, C., VanDussen, K. L., Miyoshi, H. & Stappenbeck, T. S. Development of a primary mouse intestinal epithelial cell monolayer culture system to evaluate factors that modulate IgA transcytosis. *Mucosal Immunol.* **7**, 818–828 (2014).
132. Stelzner, M. *et al.* A nomenclature for intestinal in vitro cultures. *AJP Gastrointest. Liver Physiol.* **302**, G1359–G1363 (2012).
133. Gracz, A. D. *et al.* Brief report: CD24 and CD44 mark human intestinal epithelial cell populations with characteristics of active and facultative stem cells. *Stem Cells* **31**, 2024–2030 (2013).
134. Leslie, J. L. *et al.* Persistence and toxin production by.
135. Dutta, D., Heo, I. & Clevers, H. Disease Modeling in Stem Cell-Derived 3D Organoid Systems. *Trends Mol. Med.* **23**, 393–410 (2017).
136. Gach, P. C., Wang, Y., Phillips, C., Sims, C. E. & Allbritton, N. L. Isolation and manipulation of living adherent cells by micromolded magnetic rafts. *Biomicrofluidics* **5**, 1–12 (2011).
137. Oesterle, A. Pipette Cookbook 2015. 100 (2015). doi:10.1017/CBO9781107415324.004
138. Engevik, M. A. *et al.* Human *Clostridium difficile* infection: inhibition of NHE3 and microbiota profile. *Am. J. Physiol. - Gastrointest. Liver Physiol.* **308**, G497–G509 (2015).
139. Bray, M. & Carpenter, A. E. Advanced Assay Development Guidelines for Image-Based High Content Screening and Analysis Assay Guidance Manual. *Assay Guid. Man.* (2013).
140. Leslie, J. L. *et al.* Persistence and toxin production by *Clostridium difficile* within human intestinal organoids result in disruption of epithelial paracellular barrier function. *Infect. Immun.* **83**, 138–145 (2015).
141. Wilson, S. S., Tocchi, A., Holly, M. K., Parks, W. C. & Smith, J. G. A small intestinal organoid model of non-invasive enteric pathogen-epithelial cell interactions. *Mucosal Immunol.* **8**, 352–361 (2015).
142. Forbester, J. L. *et al.* Interaction of salmonella enterica serovar Typhimurium with intestinal organoids derived from human induced pluripotent stem cells. *Infect. Immun.* **83**, 2926–2934 (2015).
143. Schlaermann, P. *et al.* A novel human gastric primary cell culture system for modelling *Helicobacter pylori* infection in vitro. *Gut* **65**, 202–213 (2016).
144. Wroblewski, L. E. *et al.* *Helicobacter pylori* targets cancer-associated apical-junctional constituents in gastroids and gastric epithelial cells. *Gut* **64**, 720–730 (2015).

145. Hill, D. R. *et al.* Bacterial colonization stimulates a complex physiological response in the immature human intestinal epithelium. *Elife* **6**, (2017).
146. Paredes-Sabja, D., Shen, A. & Sorg, J. A. Clostridium difficile spore biology: sporulation, germination, and spore structural. *Trends Microbiol.* **22**, 406–416 (2014).
147. Engevik, M. A. *et al.* Human *Clostridium difficile* infection: altered mucus production and composition. *Am. J. Physiol. - Gastrointest. Liver Physiol.* **308**, G510–G524 (2015).
148. Hiergeist, A. & Reischl, U. Multicenter quality assessment of 16S ribosomal DNA-sequencing for microbiome analyses reveals high inter-center variability. *Int. J. Med. Microbiol.* **306**, 334–342 (2016).
149. Stulberg, E. *et al.* An assessment of US microbiome research. *Nat. Microbiol.* **1**, 1–7 (2016).
150. Gunasekara, D. B. *et al.* Development of Arrayed Colonic Organoids for Screening of Secretagogues Associated with Enterotoxins. *Anal. Chem.* **90**, 1941–1950 (2018).
151. Dekkers, J. F. *et al.* A functional CFTR assay using primary cystic fibrosis intestinal organoids. *Nat. Med.* **19**, 939–945 (2013).
152. Edelstein, A. D. *et al.* Advance methods of microscope control using microManager software. **1**, 1–18 (2015).
153. Miyoshi, H. & Stappenbeck, T. S. In vitro expansion and genetic modification of gastrointestinal stem cells as organoids. *Nat. Protoc.* **8**, 2471–2482 (2013).
154. Bartfeld, S. *et al.* In Vitro Expansion of Human Gastric Epithelial Stem Cells and Their Responses to Bacterial Infection. *Gastroenterology* **148**, 126–136.e6 (2015).
155. Attayek, P. J. *et al.* Automated microraft platform to identify and collect non-adherent cells successfully gene-edited with CRISPR-Cas9. *Biosens. Bioelectron.* **91**, 175–182 (2017).
156. Delley, R. Series for the Exponentially Modified Gaussian Peak Shape. *Anal. Chem.* **57**, 388 (1985).
157. Otsu, N. A Threshold Selection Method from Gray-Level Histograms. *IEEE Trans. Syst. Man. Cybern.* **9**, 62–66 (1979).
158. Eliceiri, K., Schneider, C. A., Rasband, W. S. & Eliceiri, K. W. NIH Image to ImageJ: 25 years of image analysis HISTORICAL commentary NIH Image to ImageJ: 25 years of image analysis. *Nat. Methods* **9**, 671–675 (2012).
159. Caporaso, J. G. *et al.* Global patterns of 16S rRNA diversity at a depth of millions of sequences per sample. *Proc. Natl. Acad. Sci.* **108**, 4516–4522 (2011).
160. Lozupone, C. & Knight, R. UniFrac: a New Phylogenetic Method for Comparing Microbial Communities UniFrac: a New Phylogenetic Method for Comparing Microbial Communities. *Appl. Environ. Microbiol.* **71**, 8228–8235 (2005).

161. Lozupone, C., Hamady, M. & Knight, R. UniFrac - An online tool for comparing microbial community diversity in a phylogenetic context. *BMC Bioinformatics* **7**, 1–14 (2006).
162. Scoville, D. H., Sato, T., He, X. C. & Li, L. Current View: Intestinal Stem Cells and Signaling. *Gastroenterology* **134**, 849–864 (2008).
163. van der Flier, L. G. & Clevers, H. Stem Cells, Self-Renewal, and Differentiation in the Intestinal Epithelium. *Annu. Rev. Physiol.* **71**, 241–260 (2009).
164. Battle, E. *et al.*  $\beta$ -catenin and TCF mediate cell positioning in the intestinal epithelium by controlling the expression of EphB/EphrinB. *Cell* **111**, 251–263 (2002).
165. Van Es, J. H. & Clevers, H. Notch and Wnt inhibitors as potential new drugs for intestinal neoplastic disease. *Trends Mol. Med.* **11**, 496–502 (2005).
166. Du, H., Nie, Q. & Holmes, W. R. The Interplay between Wnt Mediated Expansion and Negative Regulation of Growth Promotes Robust Intestinal Crypt Structure and Homeostasis. *PLoS Comput. Biol.* **11**, 1–23 (2015).
167. Kosinski, C. *et al.* Gene expression patterns of human colon tops and basal crypts and BMP antagonists as intestinal stem cell niche factors. *Proc. Natl. Acad. Sci.* **104**, 15418–15423 (2007).
168. Beta, C. & Bodenschatz, E. Microfluidic tools for quantitative studies of eukaryotic chemotaxis. *Eur. J. Cell Biol.* **90**, 811–816 (2011).
169. Tehranirokh, M., Kouzani, A. Z., Francis, P. S. & Kanwar, J. R. Microfluidic devices for cell cultivation and proliferation. *Biomicrofluidics* **7**, (2013).
170. Kim, S., Kim, H. J. & Jeon, N. L. Biological applications of microfluidic gradient devices. *Integr. Biol.* **2**, 584 (2010).
171. Miyoshi, H. & Stappenbeck, T. S. Counteracting stem cell expansion during wound repair Distinct roles of non-canonical Wnt and TGF- $\beta$ . *Cell Cycle* **12**, 387–388 (2013).
172. Kim, H. J. & Ingber, D. E. Gut-on-a-Chip microenvironment induces human intestinal cells to undergo villus differentiation. *Integr. Biol.* **5**, 1130 (2013).
173. Wang, L., Murthy, S. K., Barabino, G. A. & Carrier, R. L. Synergic effects of crypt-like topography and ECM proteins on intestinal cell behavior in collagen based membranes. *Biomaterials* **31**, 7586–7598 (2010).
174. Pfluger, C. A., McMahon, B. J., Carrier, R. L. & Burkey, D. D. Precise, Biomimetic Replication of the Multiscale Structure of Intestinal Basement Membrane Using Chemical Vapor Deposition. *Tissue Eng. Part A* **19**, 649–656 (2013).
175. Shaffiey, S. A. *et al.* Intestinal stem cell growth and differentiation on a tubular scaffold with evaluation in small and large animals. *Regen. Med.* **11**, 45–61 (2016).
176. Meer, A. D. van der & Berg, A. van den. Organs-on-chips: breaking the in vitro impasse. *Integr. Biol.* **4**, 461 (2012).

177. Formeister, E. J. *et al.* Distinct SOX9 levels differentially mark stem/progenitor populations and enteroendocrine cells of the small intestine epithelium. *AJP Gastrointest. Liver Physiol.* **296**, G1108–G1118 (2009).
178. Crank, J. *the Mathematics of Diffusion.* (1975). doi:10.1016/0306-4549(77)90072-X
179. Chan, T. F. & Vese, L. A. Active contours without edges. *IEEE Trans. Image Process.* **10**, 266–277 (2001).
180. Li, C. H. & Tam, P. K. S. An iterative algorithm for minimum cross entropy thresholding. *Pattern Recognit. Lett.* **19**, 771–776 (1998).
181. Bright, D. S. & Steel, E. B. Two-dimensional top hat filter for extracting spots and spheres from digital images. *J. Microsc.* **146**, 191–200 (1987).
182. Frigge, M. *et al.* Some Implementations of the Boxplot Linked references are available on JSTOR for this article : Some Implementations of the Boxplot. **43**, 50–54 (2016).
183. Fitzmaurice, G. M. & Ravichandran, C. A primer in longitudinal data analysis. *Circulation* **118**, 2005–2010 (2008).
184. Holzmann, H., Munk, A., Suster, M. & Zucchini, W. Hidden Markov models for circular and linear-circular time series. *Environ. Ecol. Stat.* **13**, 325–347 (2006).
185. Wang, Y. *et al.* Capture and 3D culture of colonic crypts and colonoids in a microarray platform. *Lab Chip* **13**, 4625 (2013).
186. Xia, Y. & Whitesides, G. Soft lithography. *Annu. Rev. Mater. Sci.* **28**, 153–184 (1998).
187. Roskoski, R. Vascular endothelial growth factor (VEGF) signaling in tumor progression. *Crit. Rev. Oncol. Hematol.* **62**, 179–213 (2007).
188. Chen, R. R., Silva, E. A., Yuen, W. W. & Mooney, D. J. Spatio-temporal VEGF and PDGF delivery patterns blood vessel formation and maturation. *Pharm. Res.* **24**, 258–264 (2007).
189. Abhyankar, V. V. *et al.* A platform for assessing chemotactic migration within a spatiotemporally defined 3D microenvironment. *Lab Chip* **8**, 1507 (2008).
190. Abhyankar, V. V., Lokuta, M. A., Huttenlocher, A. & Beebe, D. J. Characterization of a membrane-based gradient generator for use in cell-signaling studies. *Lab Chip* **6**, 389 (2006).
191. Zeng, C. *et al.* Evaluation of 5-ethynyl-2'-deoxyuridine staining as a sensitive and reliable method for studying cell proliferation in the adult nervous system. *Brain Res.* **1319**, 21–32 (2010).
192. Lara Rodriguez, L. & Schneider, I. C. Directed cell migration in multi-cue environments. *Integr. Biol.* **5**, 1306 (2013).

193. Wrobel, M. R. & Sundararaghavan, H. G. Directed Migration in Neural Tissue Engineering. *Tissue Eng. Part B Rev.* **20**, 93–105 (2014).
194. Schneider, I. C. & Haugh, J. M. Mechanisms of gradient sensing and chemotaxis: Conserved pathways, diverse regulation. *Cell Cycle* **5**, 1130–1134 (2006).
195. Comalada, M. *et al.* The effects of short-chain fatty acids on colon epithelial proliferation and survival depend on the cellular phenotype. *J. Cancer Res. Clin. Oncol.* **132**, 487–497 (2006).
196. Metabolites, M. *et al.* The Colonic Crypt Protects Stem Cells from Article The Colonic Crypt Protects Stem Cells from. *Cell* **165**, 1–13 (2016).
197. Malago, J. J. *et al.* Differential modulation of enterocyte-like Caco-2 cells after exposure to short-chain fatty acids. *Food Addit. Contam.* **20**, 427–37 (2003).
198. Chao, A. C. *et al.* In vitro and in vivo evaluation of effects of sodium caprate on enteral peptide absorption and on mucosal morphology. *Int. J. Pharm.* **191**, 15–24 (1999).
199. Usami, M., Komurasaki, T., Hanada, A., Kinoshita, K. & Ohata, A. Effect of  $\gamma$ -linolenic acid or docosahexaenoic acid on tight junction permeability in intestinal monolayer cells and their mechanism by protein kinase C activation and/or eicosanoid formation. *Nutrition* **19**, 150–156 (2003).
200. Haas, M. J. *et al.* Nicotinic acid induces apolipoprotein A-I gene expression in HepG2 and Caco-2 cell lines. *Metabolism.* **60**, 1790–1796 (2011).
201. Ooi, C. C. *et al.* Structure-activity relationship of butyrate analogues on apoptosis, proliferation and histone deacetylase activity in HCT-116 human colorectal cancer cells. *Clin. Exp. Pharmacol. Physiol.* **37**, 905–911 (2010).
202. Zhao, P. *et al.* Targeting of the Orphan Receptor GPR35 by Pamoic Acid: A Potent Activator of Extracellular Signal-Regulated Kinase and -Arrestin2 with Antinociceptive Activity. *Mol. Pharmacol.* **78**, 560–568 (2010).
203. Salovaara, S., Sandberg, A.-S. & Andlid, T. Organic Acids Influence Iron Uptake in the Human Epithelial Cell Line Caco-2. *J. Agric. Food Chem.* **50**, 6233–6238 (2002).
204. Ridlon, J. M. & Bajaj, J. S. The human gut sterolbiome: Bile acid-microbiome endocrine aspects and therapeutics. *Acta Pharm. Sin. B* **5**, 99–105 (2015).
205. Abbasi, N., Akhavan, M. M., Rahbar-Roshandel, N. & Shafiei, M. The effects of low and high concentrations of luteolin on cultured human endothelial cells under normal and glucotoxic conditions: Involvement of integrin-linked kinase and cyclooxygenase-2. *Phyther. Res.* **28**, 1301–1307 (2014).
206. Cheng, Z., Surichan, S., Ruparelia, K., Arroo, R. & Boarder, M. R. Tangeretin and its metabolite 4'-hydroxytetramethoxyflavone attenuate EGF-stimulated cell cycle progression in hepatocytes; Role of inhibition at the level of mTOR/p70S6K. *Br. J. Pharmacol.* **162**, 1781–1791 (2011).

207. Refolo, M. G. *et al.* Anti Proliferative and Pro Apoptotic Effects of Flavonoid Quercetin Are Mediated by CB1 Receptor in Human Colon Cancer Cell Lines. *J. Cell. Physiol.* **230**, 2973–2980 (2015).
208. Moskot, M. *et al.* Activities of genes controlling sphingolipid metabolism in human fibroblasts treated with flavonoids. *Metab. Brain Dis.* **30**, 1257–1267 (2015).
209. Huang, H. *et al.* Dietary compounds galangin and myricetin suppress ovarian cancer cell angiogenesis. *J. Funct. Foods* **15**, 464–475 (2015).
210. Mukhtar, E., Adhami, V. M., Sechi, M. & Mukhtar, H. Dietary flavonoid fisetin binds to  $\beta$ -tubulin and disrupts microtubule dynamics in prostate cancer cells. *Cancer Lett.* **367**, 173–183 (2015).
211. Duan, J. *et al.* Transport characteristics of isorhamnetin across intestinal Caco-2 cell monolayers and the effects of transporters on it. *Food Chem. Toxicol.* **66**, 313–320 (2014).
212. Keung, W. M. & Vallee, B. L. Daidzin: a potent, selective inhibitor of human mitochondrial aldehyde dehydrogenase. *Proc. Natl. Acad. Sci. U. S. A.* **90**, 1247–1251 (1993).
213. Kopečná-Zapletalová, M., Krasulová, K., Anzenbacher, P., Hodek, P. & Anzenbacherová, E. Interaction of isoflavonoids with human liver microsomal cytochromes P450: inhibition of CYP enzyme activities. *Xenobiotica* **47**, 324–331 (2017).
214. Toro-Funes, N. *et al.* The intracellular metabolism of isoflavones in endothelial cells. *Food Funct.* **6**, 97–107 (2015).
215. Hu, L. *et al.* Protective effects of neohesperidin dihydrochalcone against carbon tetrachloride-induced oxidative damage in vivo and in vitro. *Chem. Biol. Interact.* **213**, 51–59 (2014).
216. Hachet-Haas, M. *et al.* Small neutralizing molecules to inhibit actions of the chemokine CXCL12. *J. Biol. Chem.* **283**, 23189–23199 (2008).
217. Fabiani, R., Rosignoli, P., De Bartolomeo, A., Fuccelli, R. & Morozzi, G. DNA-damaging ability of isoprene and isoprene mono-epoxide (EPOX I) in human cells evaluated with the comet assay. *Mutat. Res. - Genet. Toxicol. Environ. Mutagen.* **629**, 7–13 (2007).
218. Sakurazawa, T. & Ohkusa, T. Cytotoxicity of organic acids produced by anaerobic intestinal bacteria on cultured epithelial cells. *J. Gastroenterol.* **40**, 600–609 (2005).
219. Gan, X. *et al.* Dual Mechanisms of ABCA1 Regulation by Geranylgeranyl Pyrophosphate. *J. Biol. Chem.* **276**, 48702–48708 (2001).
220. Zhang, W. & Lim, L. Y. Effects of spice constituents on P-glycoprotein-mediated transport and CYP3A4-mediated metabolism in vitro. *Drug Metab. Dispos.* **36**, 1283–1290 (2008).

221. Yoshida, N., Takagi, A., Kitazawa, H., Kawakami, J. & Adachi, I. Inhibition of P-glycoprotein-mediated transport by extracts of and monoterpenoids contained in *Zanthoxyli Fructus*. *Toxicol. Appl. Pharmacol.* **209**, 167–173 (2005).
222. Donovan, S. M., Andres, A., Mathai, R. A., Kuhlenschmidt, T. B. & Kuhlenschmidt, M. S. Soy formula and isoflavones and the developing intestine. *Nutr. Rev.* **67**, (2009).